# Direct Numerical Simulations of Reactive Transport Processes at Single Bubbles

Vom Fachbereich Maschinenbau
an der Technischen Universität Darmstadt
zur
Erlangung des Grades eines Doktor-Ingenieurs (Dr.-Ing.) genehmigte

DISSERTATION

vorgelegt von

M.Sc. Manuel Falcone

geboren in Pescara

Berichterstatter: Prof. Dr. Dieter Bothe
Mitberichterstatter: Prof. Dr. Michael Schäfer

Tag der Einreichung: 04.10.2018
Tag der mündlichen Prüfung: 11.12.2018

Darmstadt 2019
D17

Manuel Falcone: Direct Numerical Simulations of Reactive Transport Processes at Single Bubbles
Darmstadt, Technische Universität Darmstadt,
Year thesis published in TUprints 2019
Date of the viva voce 11.12.2018

# Zusammenfassung

Reaktive Stofftransportprozesse kommen in vielen Anwendungen der Chemietechnik vor. Obwohl diese Phänomene schon seit langem Gegenstand zahlreicher Untersuchungen sind, wurde ein vollständiges Verständnis der physico-chemischen Mechanismen bisher noch nicht erreicht. Detaillierte Erkenntnisse über diese Prozesse, insbesondere das lokale Zusammenspiel zwischen der zweiphasigen Hydrodynamik, dem Stofftransport und den chemischen Reaktionen, wurden in den letzten Jahren mittels Direkter Numerischer Simulationen gewonnen. Diese Art der Simulation ist heutzutage noch rechenintensiv. Da die Konzentrationsgrenzschichten an Blasengrenzflächen beachtlich dünner sind als die Geschwindigkeitsgrenzschicht, erfordert eine genaue Lösung der Spezieskonzentrationstransportgleichungen eine deutlich höhere numerische Auflösung als für die Zweiphasenhydrodynamik. Zwei unterschiedliche numerische Techniken wurden in dieser Arbeit mit dem Ziel der Linderung des Mehrskalenproblems entwickelt. In beiden Fällen wird das hydrodynamische Problem mittels einer Arbitrary Lagrangian-Eulerian Interface-Tracking-Methode angegangen, jedoch unterscheiden sich die Verfahren in der Behandlung des Stofftransportes. Der erstgenannte Ansatz basiert auf den sogenannten Radial Basis Functions, mit denen eine Finite-Differenzen-Methode für unstrukturierte Punktmengen formuliert wird. Letzterer verwendet das Finite-Volumen-Verfahren auf einem Gitter, das durch eine spezalisierte Verfeinerung des Netzes, welches für die zweiphasige Hydrodynamik verwendet wird, erhalten wird.

In der vorliegenden Arbeit wurde eine systematische Analyse von reaktiven Stoffaustauschprozessen aus einzelnen aufsteigenden Blasen mit signifikanten Grenzflächenverformungen, d.h. relevanten technischen Durchmessern, mittels 3D Direkten Numerischen Simulationen durchgeführt. Zwei unterschiedliche prototypische Reaktionen wurden berücksichtigt. Simulationen von langsamen zu schnellen Reaktionsintensitäten erlaubten die Beurteilung des Einflusses verschiedener chemischer Zeitskalen auf diese Prozesse. Zusätzlich wurde der Einfluss von niedrigen bis moderaten Diffusionskoeffizienten der Übergangsspezies untersucht. Der letzte Teil der Arbeit wurde dem Vergleich der Simulationsergebnisse mit den Vorhersagen der Filmtheorie gewidmet.

# Abstract

Reactive mass transfer processes are found in many chemical engineering applications. Though these phenomena have been object of investigation for long time already, a complete understanding of the physico-chemical mechanisms involved has not been achieved yet. More detailed insights about these processes, in particular the local interplay between the two-phase hydrodynamics, mass transfer and chemical reactions, have been obtained in recent years by means of Direct Numerical Simulations. However, this type of simulation is nowadays still computationally demanding. Being the concentration boundary layers at bubble interfaces remarkably thinner than the velocity boundary layer, an accurate solution of the species concentration transport equations requires a numerical resolution significantly higher than that needed for the two-phase hydrodynamics. Two different numerical techniques have been developed in this work with the aim of alleviating the multiscale issue. In both the cases, the hydrodynamic problem is tackled by means of an Arbitrary Lagrangian-Eulerian Interface-Tracking method. Instead, they differ regarding the treatment of the mass transfer. The former technique relies on the so-called Radial Basis Functions by which a finite-difference method on unstructered sets of points is formulated. The latter employs a finite-volume discretisation on a mesh obtained from a specialised refinement of the grid used for the two-phase hydrodynamics.

In the present research, a systematic analysis of the reactive mass transfer from single rising bubbles with significant interface deformations, i.e. technically relevant diameters, has been carried out by means of 3D Direct Numerical Simulations. Two distinct reaction prototypes representative of many applications have been considered. Simulations from slow to fast reaction intensities allowed to assess the influence of different chemical time scales on these processes. Additionally, the impact of low to moderate dissolving species diffusivities has been investigated. The last part of the study has been dedicated to the comparison of the simulation results with the predictions of the film theory.

# Acknowledgments

First of all, I would like to thank Prof. Dr. Bothe for his scientific supervision and the given opportunity to work at the Mathematical Modeling and Analysis research group of the Technical University of Darmstadt. Furthermore, special thanks go to all my colleagues for their contribution to the development of this project. In particular, I would like to express my deepest gratitude to Tomislav, Chiara and Andre for their fundamental help and the nice time we spent together.

I would like to acknowledge the financial support of the Deutsche Forschungsgemeinschaft priority program SPP 1740 "Influence of Local Transport Processes on Chemical Reactions in Bubbly Flows" and the Lichtenberg high performance computer of the Technical University of Darmstadt where the calculations for this research were conducted.

The realisation of this project would not have been possible without the invaluable support of my family and my girlfriend Chrissi who accompanied me throughout these years through this difficult but very significant experience.

# Own Publications

The following publications originated from the research presented in this thesis.

Falcone, Manuel, and Holger Marschall. “Explicit Radial-Basis-Function-Based Finite-Difference Method for interfacial mass-transfer problems.” Chemical Engineering & Technology 40.8 (2017): 1385-1390.

Falcone, Manuel, Bothe Dieter, and Marschall Holger. “3D Direct Numerical Simulations of reactive mass transfer from deformable single bubbles: An analysis of mass transfer coefficients and reaction selectivities.” Chemical Engineering Science 177 (2018): 523-536.

# Contents

# List of Figures

List of Figures

# List of Tables

# Nomenclature

## Roman letter symbols

| Symbol | Description | Units |
|---|---|---|
| $\mathbf{a}$ | acceleration vector | $m/s^2$ |
| $\mathbf{A}^{(k)}$ | matrix of the local system $k$ | - |
| $A$ | surface area | $m^2$ |
| $a$ | bubble aspect ratio | - |
| $B$ | boundary operator | - |
| $c_k$ | concentration of the species $k$ | $mol/m^3$ |
| $d_b$ | bubble diameter | m |
| $D_k$ | diffusivity of the species $k$ | $m^2/s$ |
| $E$ | bubble eccentricity | - |
| E | enhancement factor | - |
| $\mathbf{F}$ | force vector | N |
| $f$ | fraction of the cell volume occupied by the liquid | - |
| $\mathbf{g}$ | gravity acceleration vector | $m/s^2$ |
| $g$ | gravity acceleration | $m/s^2$ |
| $k_j$ | coefficient of the $j^{\text{th}}$ reaction | $m^3/mol{\cdot}s$ |
| $L$ | differential operator | - |
| $\overline{L}$ | modified differential operator | - |
| $\dot{m}$ | mass flux | kg/s |
| $m$ | mass | kg |
| $\mathbf{n}$ | unit normal vector | - |
| $\dot{n}'$ | molar transfer rate per unit interfacial area | $mol/m^2{\cdot}s$ |
| $N$ | generic mesh cell neighbor | - |
| $N_b$ | number of bubbles in the reactor | - |
| $n_k$ | number of moles of the species $k$ | mol |
| $P$ | generic mesh cell | - |
| $p$ | pressure | $N/m^2$ |
| $Q$ | gas absorbed in a time interval $\theta$ per unit intefacial area | $mol/m^2$ |
| $r_j$ | rate of the $j^{\text{th}}$ reaction | $mol/m^3{\cdot}s$ |

| | | |
|---|---|---|
| $R_k$ | reaction source/sink term of the species $k$ | mol/m$^3$·s |
| $S$ | reaction selectivity | - |
| | surface of the volume $V$ | - |
| $s$ | parameter of Danckwerts's surface renewal model | 1/s |
| $S_\Sigma$ | bubble surface | - |
| $\mathbf{S}$ | viscous stress tensor | N/m$^2$ |
| | area vector | m$^2$ |
| $t$ | time | s |
| $\mathbf{U}_b$ | bubble velocity vector | m/s |
| $U_b$ | bubble velocity | m/s |
| $\mathbf{u}_p$ | particle velocity vector | m/s |
| $\dot{V}$ | volume flux | m$^3$/s |
| $\mathbf{v}$ | velocity vector | m/s |
| $V$ | volume | m$^3$ |
| $\mathbf{v}_S$ | surface velocity vector | m/s |
| $\mathbf{x}$ | position vector | m |

## Greek letter symbols

| **Symbol** | **Description** | **Units** |
|---|---|---|
| $\beta_l$ | mass transfer coefficient | m/s |
| $\Gamma$ | viscosity ratio $\mu_g/\mu_l$ | - |
| | diffusion coefficient for the mesh displacement | - |
| $\gamma$ | density ratio $\rho_g/\rho_l$ | - |
| $\Delta$ | inter-point spacing | m |
| $\Delta t$ | time-step | s |
| $\delta$ | film thickness | m |
| $\delta_h$ | thickness of the hydrodynamic boundary layer | m |
| $\delta_k$ | thickness of the concentration boundary layer of the species $k$ | m |
| $\epsilon$ | Radial Basis Function free parameter | - |
| $\epsilon_g$ | void fraction | - |
| $\theta$ | time interval | s |
| | polar angle | deg |
| $\kappa$ | total curvature of the interface | 1/m |
| | Damköhler ratio $\mathrm{Da}_2/\mathrm{Da}_1$ | - |
| $\mu$ | dynamic viscosity | kg/m·s |
| $\nu$ | kinematic viscosity | m$^2$/s |
| $\nu_{k,j}$ | stoichiometric coefficient of the species $k$ in the $j^{\text{th}}$ reaction | - |
| $\Pi^d$ | space of all $d$-variate polynomials | - |

| | | |
|---|---|---|
| $\rho$ | density | $\mathrm{kg/m^3}$ |
| $\sigma$ | surface tension coefficient | N/m |
| $\tau_{\mathrm{hyd}}$ | hydrodynamic contact time | s |
| $\chi$ | area stretch factor | - |
| $\Omega$ | open set | - |

## Subscripts and Superscripts

| **Symbol** | **Description** |
|---|---|
| $\Sigma$ | interface |
| $\infty$ | infinite distance from the interface |
| + | liquid-side limit |
| - | gas-side limit |
| b | bulk |
| | bubble |
| eq | volume-equivalent bubble |
| f | face |
| g | gas phase |
| i | interface |
| in | inlet |
| l | liquid phase |
| loc | local |
| p | particle |
| phys | physisorption |
| sim | simulation |

## Abbreviations

| **Symbol** | **Description** |
|---|---|
| ALE | Arbitrary Lagrangian-Eulerian |
| CPD | Conditionally Positive Definite |
| CST | Continuous Species Transfer |
| DNS | Direct Numerical Simulation |
| FT | Front-Tracking |
| LS | Level-Set |
| ODE | ordinary differential equation |
| PDE | partial differential equation |
| PISO | Pressure Implicit with Splitting of Operator |

| | |
|---|---|
| PLIC | Piecewise Linear Interface Calculation |
| RBF | Radial Basis Function |
| VoF | Volume-of-Fluid |

## Dimensionless numbers

| Symbol | Description |
|---|---|
| $\tilde{\phi}$ | generic dimensionless quantity |
| $\mathrm{Da}_j$ | Damköhler number of the $j^{\mathrm{th}}$ reaction |
| Eo | Eötvös number |
| Fr | Froude number |
| $\mathrm{H}_k$ | Henry coefficient of the species $k$ |
| Ha | Hatta number |
| Mo | Morton number |
| $\mathrm{Pe}_k$ | Péclet number of the species $k$ |
| $\mathrm{Re}_b$ | bubble Reynolds number |
| $\mathrm{Sc}_k$ | Schmidt number of the species $k$ |
| Sh | Sherwood number |
| We | Weber number |

## Other symbols

| Symbol | Description | Units |
|---|---|---|
| $[\![\phi]\!]$ | jump of the quantity $\phi$ at the interface | - |
| $\nabla_\Sigma$ | surface gradient operator | 1/m |
| $\mathbf{R}^d$ | $d$-dimensional Euclidean vector space | - |

# Chapter 1

# Introduction

Many industrial products are based on gas-liquid reactions in bubble column reactors. Some examples are liquid-phase oxidation, fermentation, chlorination, Fischer-Tropsch synthesis and wastewater treatment processes. These reactors are basically constituted of cylindrical vessels filled with a liquid, either stagnant or continuously flowing. The gas is injected through a sparger usually placed at the bottom of the column. A mass exchange occurs at the interface between the liquid and gas phases. The dissolving chemical components typically react with other species leading to the formation of some products and/or side-products. A schematic representation of a bubble column reactor is shown in Fig. 1.1.

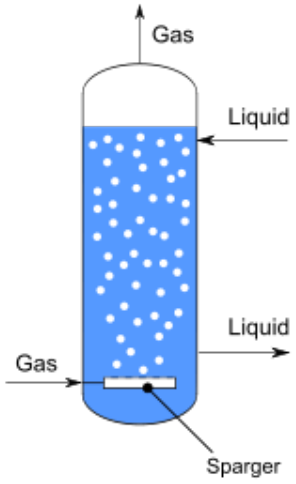


Figure 1.1: Schematic of a bubble column reactor.

Depending on the operating parameters (superficial gas and liquid velocities), material properties (densities and viscosities of the fluids) and the geometry of the reactor, four main flow regimes can be identified in a bubble column: *homogeneous* or *bubbly*, *churn turbulent*, *slug* and *annular*. The last

three flow types belong to the so-called *heterogeneous* regime.

The homogeneous flow regime is encountered at low superficial gas velocity values. As visible in Fig. 1.2, the bubbles have almost the same size and their distribution inside the reactor is uniform. Although interaction effects among the bubbles are always present, they can be considered less important in this case (see Khinast, 2001, Majumder, 2016). Under these circumstances, a single bubble analysis can describe the main aspects of the mass transfer processes.

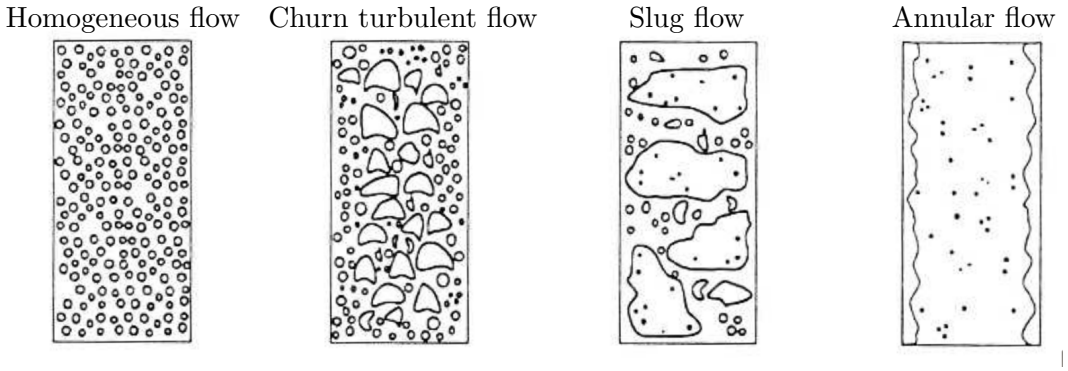


Figure 1.2: Different flow regimes of a bubble column reactor (Urseanu and Krishna, 2000).

Larger superficial gas velocities cause the transition to the churn turbulent flow regime. Due to occurence of coalescence phenomena, different bubble sizes are found inside the reactor. The flow field in the liquid phase is turbulent due to the intense agitation caused by the motion of the bubbles.

A slug flow regime characterized by a continuous coalescence and breakup process is observed when large gas flow rates are combined with small column diameters. Finally, at very high superficial gas velocities, the annular flow appears. In this case, the liquid phase forms an annulus between the column walls and the central part of the reactor which is entirely occupied by the gas phase.

Despite the apparent simplicity of these technological devices, there is no complete understanding of the interaction between the two-phase hydrodynamics, the mass transfer processes and the chemical reactions. An obstacle to the full comprehension resides in the difficulty to obtain detail information from experiments. Most experimental techniques provide only integral information precluding a deep insight into the local phenomena (Schlüter et al., 2001, Bork et al., 2003). Some progress has been recently made (Dani et al., 2007, Francois et al., 2011) by means of new experimental methods which allow for precise measurements of the concentration fields and the local mass transfer coefficients relating to single rising bubbles. However, the improvement is not yet sufficient to deal with group of bubbles, which is indispensable in order to reproduce conditions as similar as possible to the ones found in the reactors.

Experimental measurements of the mass transfer are difficult due to the extreme thinness of the concentration boundary layers. An approximation of the concentration boundary layer thickness for a physisorption process is given by the following relation (Bird et al., 2007)

$$\delta_k \propto \frac{\delta_h}{\sqrt{\mathrm{Sc}_k}} \propto \frac{1}{\sqrt{\mathrm{Pe}_k}}, \tag{1.1}$$

where $Sc_k$ is the Schmidt number of the species $k$ and $Pe_k$ is the corresponding Péclet number. $\delta_h$ and $\delta_k$ denote the hydrodynamic and concentration boundary layer thicknesses, respectively. The Schmidt number ($Sc_k$=$\nu_l/D_{k,l}$) is expressed by the ratio between the liquid kinematic viscosity $\nu_l$ and the species diffusion coefficient in the liquid phase $D_{k,l}$. The Péclet number ($Pe_k$=$U_b d_b/D_{k,l}$) is the product of the Schmidt number with the bubble Reynolds number ($Re_b$=$U_b d_b/\nu_l$), where $U_b$ and $d_b$ represent the bubble velocity and diameter, respectively.

For an industrial bubble reactor, the Péclet number ranges from $10^4$ to $10^7$ leading to thin concentration boundary layers of few micrometer thickness or even less. The situation becomes even more severe if chemisorption is considered. The chemical reactions consume the dissolving species, thinning the boundary layer further.

Fig. 1.3 shows an experimental image together with two successive magnifications of an oxygen concentration boundary layer. The image has been obtained by Kück et al. (2009) by means a LIF technique. The thickness of the shaded area corresponding to the region of higher oxygen concentration is ca. 30 micrometers.

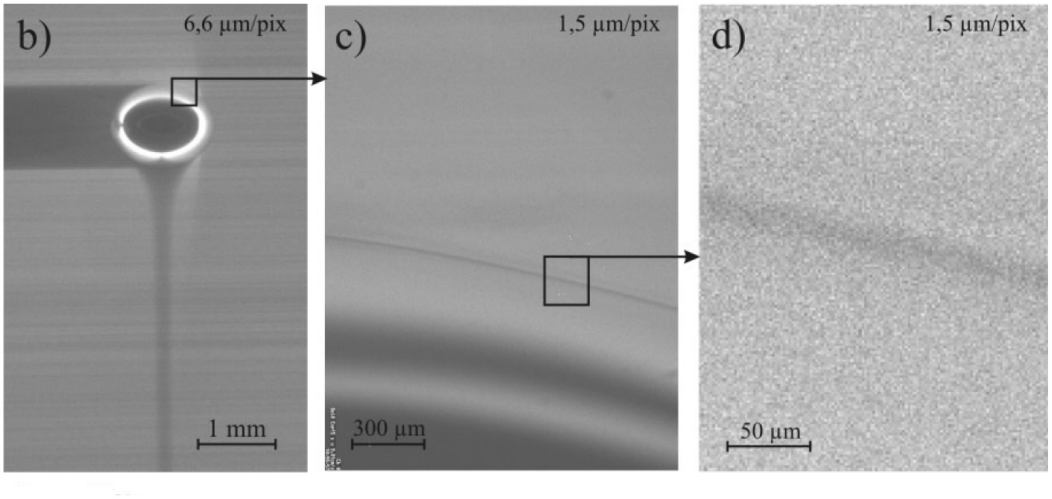


Figure 1.3: Oxygen concentration boundary layer around a gas bubble rising in water. Shaded areas indicate regions with higher oxygen concentration (Kück et al., 2009).

As further critical element for experimental investigations, it has to be remarked that the bubbles flowing through the reactors exihibit unstationary behaviors with non-rectilinear rise paths. Accordingly, the transfer problem is characterized by three-dimensional structures. These strcutures can be hardly captured by the various experimental methods which in the best-case scenario can only measure quantities on two perpendicular planes.

Fig. 1.4 shows a sequence of images regarding a carbon dioxide bubble with diameter of 1.1 mm rising in an aqueous solution contaminated with the Triton X-100 surfactant. The experiment has been carried out by Stöhr et al. (2009) by means of a PLIF technique. Although the sizes of the bubbles in Figs. 1.3 and 1.4 are comparable, the species concentration fields in the wake region look

significantly different. This is due to presence of surfactants at the gas-liquid interface which determines locally a variation of the surface tension coefficient and, consequently, a drastic change of the velocity field in the vicinity of the bubble surface. This in turn strongly influences the mass transfer, as the comparison of the dark areas in Figs. 1.3 and 1.4 corresponding to regions with higher species concentration highlights. Although the level of interface contamination can be considerably reduced by means of specific techniques (see Duineveld, 1995), it is almost impossible to obtain a contamination-free system. Therefore, the experimental results are always affected by the surfactants to a hardly quantifiable extent and their interpretation might be distorted by this effect.

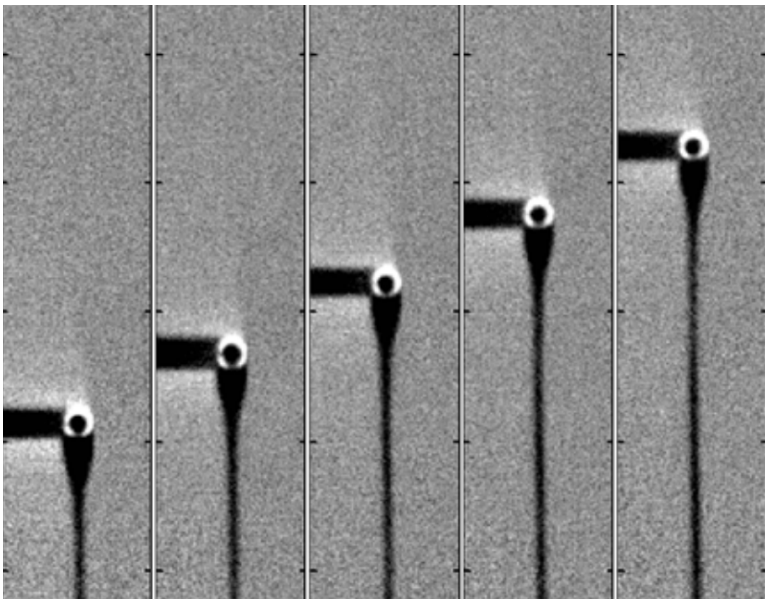

Figure 1.4: Sequence of PLIF images of a rising carbon dioxide bubble with diameter $d_b$=1.1 mm contaminated with Triton X-100. Dark areas indicate regions with higher carbon dioxide concentration (Stöhr et al., 2009).

Besides experiments, the mass transfer processes have been also studied using theoretical models (see Whitman, 1923, Higbie, 1935, Danckwerts, 1951, Clift et al., 1978). However, these models rely on strong assumptions limiting their applicability. Furthermore, they are often restricted to simplified chemical reaction mechanisms.

Due to the impossibility to obtain an exhaustive comprehension of the mass transfer processes by means of theoretical and experimental methods, numerical techniques have been increasingly employed in the last decades for the investigation of such processes. In particular, the Direct Numerical Simulation (DNS) allows to gain detailed information about the local interplay between two-phase hydrodynamics, mass transfer and chemical reactions, leading to a more complete physical understanding.

Although a DNS of the two-phase hydrodynamics of a rising bubble can be nowadays performed in a reasonable time, the situation gets significantly more severe when additional transport equations for

the species concentrations have to be numerically solved for technically relevant Péclet number and, thus, very thin concentration boundary layers. The very high numerical resolution required to capture these small-scale structures is responsible for a prohibitive computational cost in the overwhelming majority of cases. The problem becomes practically intractable if chemical reactions and multiple bubble systems are considered in order to mimic the swarm conditions of the real reactors. Assuming 2D dimensional conditions represents a typical measure to alleviate the computational issue. However, this represents a strong limitation to the significance of the results. Other strategies adopted in the literature, which attempt to introduce less drastic assumptions within the numerical framework, will be presented in the next chapter. A definitive solution to this problem is far from being achieved and, accordingly, it is fundamental to develop novel numerical methods capable to overcome the current difficulties.

# Chapter 2

# Literature Survey

In this chapter, a survey of the literature relevant to mass transfer processes in gas-liquid flows is given. Section 2.1 introduces the most important mass transfer theoretical models. Among them, a distinction must be made between heuristic models based on physical considerations and analytical models derived from rigorous physical principles. In addition to providing insights into the mechanisms of the transfer phenomena, these models, in particular the analytical ones, are useful as a benchmark for novel numerical methods.

An overview of the numerous simulation studies regarding transfer phenomena and the related numerical techniques has been reported in Section 2.2. This section points out the insufficiencies of the current state of the art and, therefore, the compelling need for further research. Finally, the objectives of the present work are outlined in Section 2.3.

## 2.1 Mass transfer models

The *film model*, also known as *film theory*, (Whitman, 1923) represents the first theoretical attempt to describe the mass transfer. It is based on the Nernst's idea of a "diffusion layer". As sketched in Fig. 2.1, this model assumes the presence of a stagnant film of thickness $\delta$ in the liquid region adjacent to the interface. The transfer of the dissolved gas through the layer is caused only by molecular diffusion. In the absence of chemical reactions, it results that the concentration value drops linearly from $c_{k,i}$ to $c_{k,b}$ within the film. The concentration is assumed to be uniform both in the liquid bulk due to the agitation of the fluid and in the gas phase due to the high value of the species diffusion coefficient $D_{k,g}$. The quantity $c_{k,i}$ is computed from the concentration value in the gas phase by considering equilibrium condition at the interface and using the Henry's law. The film model yields the following expression for the transfer rate $\dot{n}'$ per unit interfacial area

$$\dot{n}' = D_{k,l} \frac{c_{k,i} - c_{k,b}}{\delta}. \tag{2.1}$$

The film thickness $\delta$ is a model parameter. Different factors, e.g. liquid agitation, material properties,

reactor geometry, contribute to the determination of its value.

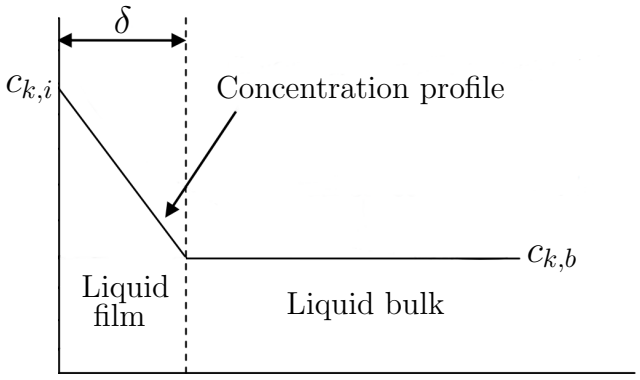


Figure 2.1: Conceptual representation of the film model.

A more elaborated model has been developed by Higbie (1935). It belongs to the category of the *surface-renewal* models which assume that the liquid elements at the interface absorb gas during a time interval $\theta$. Afterwards, they are replaced by liquid elements from the bulk with concentration values equal to $c_{k,b}$. The amount $Q$ of gas absorbed during the time $\theta$ per unit area is obtained from the solution of the following time-dependent one-dimensional diffusion equation

$$\frac{\partial c_k}{\partial t} = D_{k,l}\frac{\partial^2 c_k}{\partial x^2} \tag{2.2}$$

with the boundary and initial conditions

$$\begin{aligned} &c_k = c_{k,i}, \quad x = 0, \quad t \geq 0, \\ &c_k = c_{k,b}, \quad x > 0, \quad t = 0, \\ &c_k = c_{k,b}, \quad x = +\infty, \quad t \geq 0. \end{aligned} \tag{2.3}$$

This problem gives

$$Q = 2(c_{k,i} - c_{k,b})\sqrt{\frac{D_{k,l}\theta}{\pi}}. \tag{2.4}$$

As it emerges from Eq. (2.4), the quantity $Q$ depends on the time length $\theta$.

The reason for the continuous replacement of the liquid at the interface can be ascribed to the turbulent motion in the bulk. Different surface-renewal models have been formulated by considering different distributions for the contact times of the fluid particles forming the liquid phase. The model proposed by Higbie assumes that every fluid particle is in contact with the gas phase for the same time interval $\theta$. Accordingly, the transfer rate $\dot{n}'$ per unit interfacial area is equal to the average rate of absorption of a generic fluid particle given by the ratio $Q/\theta$. Thus, it is obtained

$$\dot{n}' = \frac{Q}{\theta} = 2(c_{k,i} - c_{k,b})\sqrt{\frac{D_{k,l}}{\pi\theta}}. \tag{2.5}$$

Similarly to the film model, the parameter $\theta$ is determined by the liquid agitation, material properties, reactor geometry, etc.

A different assumption regarding the contact times of the different fluid particles at the interface has been incorporated in the model of Danckwerts (1951). It supposes that the fraction of the interface which at any instant has been exposed to the gas for times between $\theta$ and $\theta + d\theta$ is $se^{-s\theta}d\theta$. The parameter $s$, which depends on the properties of the system, expresses the fraction of the interface that is "refreshed" with liquid from the bulk in the unit time. Therefore, $\dot{n}'$ is obtained by averaging the transfer rates per unita area of all the fluid particles at the interface. This corresponds to integrate over the whole range of contact times, i.e. from 0 to $+\infty$, the instantaneous absorption rate $(c_{k,i} - c_{k,b})\sqrt{D_{k,l}/\pi\theta}$ relating to an element exposed to the gas phase for a time $\theta$ weighted with the probability density function $f(\theta)=se^{-s\theta}$. It follows

$$\begin{aligned}\dot{n}' &= \int_0^{+\infty} (c_{k,i} - c_{k,b})\sqrt{\frac{D_{k,l}}{\pi\theta}} f(\theta) d\theta \\ &= (c_{k,i} - c_{k,b})\sqrt{\frac{D_{k,l}}{\pi}} s \int_0^{+\infty} \frac{e^{-s\theta}}{\sqrt{\theta}} d\theta \\ &= (c_{k,i} - c_{k,b})\sqrt{D_{k,l} s}.\end{aligned} \tag{2.6}$$

Though these models have been presented in the context of physisorption, they can be extended to reactive cases. However, they are usually restricted to two-step reaction mechanisms involving a limited amount of species.

The models presented above are based on a rough schematization of the mass transfer and they ignore many aspects, i.e. the curvature of the interface, a detailed description of the flow field, etc., which can profoundly affect the gas absorption. However, they have shown to accurately predict the effects of chemical reactions on the absorption rate in many cases. Danckwerts et al. (1963) found that the Higbie and Danckwerts models are in agreement with the absorption of $CO_2$ into various alkaline solutions. Danckwerts and Gillham (1966) showed that the absorption of $CO_2$ into NaOH solution in a column with a diameter length of 50 cm can be successfully estimated by the Higbie surface-renewal theory. Other experiments (see Danckwerts, 1970) confirmed the capability of these theoretical approaches to provide an accurate quantitative description of transfer phenomena.

The occurence of more complex conditions typically related to large Reynolds can lead to the failure of these simple models and require a more detailed local representation of the system in the vicinity of the interface. Clift et al. (1978) reported several results, each of them corresponding to a specific hydrodynamic regime. These results have been obtained starting from the conservation equations, which will be described in Chapter 3, introducing some assumptions suitable for the considered regime. This allows to obtain an explicit or approximate solution of the problem. However, the higher complexity of these models is accompanied by a strong difficulty to treat chemisorption phenomena. Very few results have been achieved when chemical reactions and the resulting interdependence between two or more species are introduced. The issues are related to the non-linearity of the chemical terms which makes difficult, if not impossible, a mathematical treatment of the problem.

## 2.2 Simulation studies

Several different numerical methods are used to investigate gas-liquid flows. Section 2.2.1 gives a brief description of the most common methods. Exhaustive presentations of these numerical techniques can be found in Tryggvason et al. (2011), Prosperetti and Tryggvason (2007), Wörner (2012), etc. Section 2.2.2 provides an overview of the literature regarding various transfer phenomena occurring in gas-liquid flows which have been studied by means of the methods described in Section 2.2.1. These analyses include physisorption and chemisorption processes, surface active agents (surfactants), evaporation, boiling flows, condensation, etc. Particular attention is dedicated to the studies dealing with thin concentration and/or thermal boundary layers highlighting the adopted solutions to cope with the related computational issue and the maximum values of the Péclet number achieved.

### 2.2.1 Overview of the numerical methods

The numerical methods for gas-liquid flows can be divided into two main categories. The first one is represented by the Direct Numerical Simulation (DNS) methods which aim to resolve all the spatial and temporal scales of the physical system. The Euler-Euler (Two-fluid) and the Euler-Lagrange (Discrete bubble) methods constitute the second category. In these approaches, the influence of the smallest scales on the larger ones is taken into account through modelisations.

The Euler-Euler and Euler-Lagrange methods assume great importance when simulations of entire bubble column reactors are performed. The relevant length scales of the phenomena occurring inside these devices span several orders of magnitude. Therefore, it is not possible currently, and even in the near future, to carry out a simulation able to resolve the finest structures.

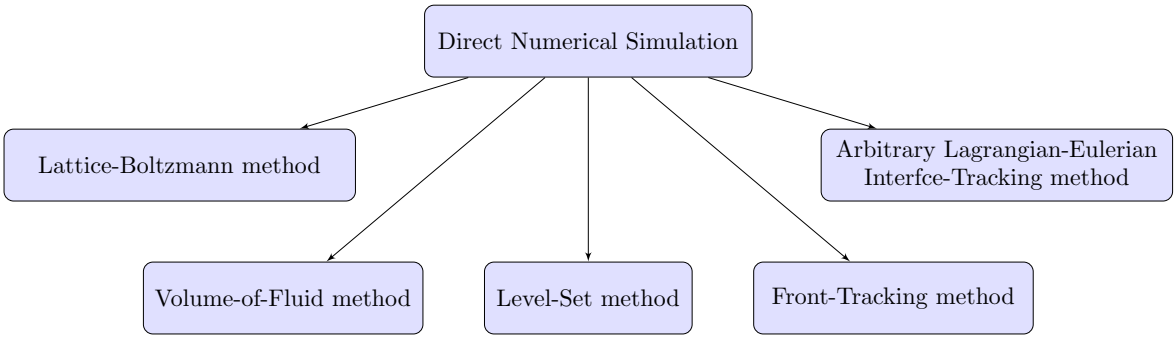


Figure 2.2: Overview of the main DNS methods for the simulation of gas-liquid flows.

**Euler-Euler and Euler-Lagrange methods**

The Euler-Euler method adopts a volume averaging procedure to obtain equations valid in the entire domain for both the phases which are treated as interpenetrating continua. The resulting system of equations resembles the single-phase Navier-Stokes equations. However, additional terms related to the interfacial mass and momentum transfer between the different phases appear. These terms have

to be modeled. This difficult task is often based on theoretical or experimental results.

Different types of averaging have been proposed by several authors. Among them, it is important to remark the time averaging (Ishii, 1975) and the ensemble averaging (Drew and Passman, 1999). The last one can be regarded as the most general averaging procedure.

The Euler-Lagrange method distinguishes between continuous and dispersed phases. With regard to the bubble column reactors, the liquid is considered the carrier phase and it is treated by means of continuum models, i.e. Navier-Stokes equations, while the gas bubbles are seen as rigid spherical particles governed by Newton's second law. The total force exerted on a particle is decomposed in different contributions, e.g. the drag, the lift, the buoyancy. Similarly to what happens in the Euler-Euler approach, these different contributions require a complex modeling based on analytical evaluations, experimental results or detailed simulations. Furthermore, the presence of particle-particle interactions and mutual influence between particles and continuous phase has to be fixed a priori depending on the specific application. For low void fractions, the so-called one-way coupling is usually chosen which only accounts for the influence of the liquid on the particles motion. The mutual interaction (two-way coupling) is considered in the case of moderate gas bubbles densities. Finally, the particle-particle interactions become important for high void fractions leading to the four-way coupling.

**Lattice-Boltzmann method**

Differently from the standard numerical methods based on the Navier-Stokes equations, the Lattice-Boltzmann method represents a discretised form of the Boltzmann's equation which describes the behavior of the fluids by means of the non-equilibrium statistical mechanics.

The main advantages of the Lattice-Boltzmann method are the ability to deal with complex geometries and the possibility to be highly parallelized. Regarding the simulation of multiphase flows, this numerical technique can maintain at a satisfactory level the sharpness of the interface.

A disadvantage is the necessity to tune microscopic input parameters in order to simulate a fluid with given thermophysical properties such as density, viscosity, diffusivity, etc. These material properties are outcomes of the computatation and, therefore, they cannot be prescribed a priori.

Another disadvantage is the numerical instability. To overcome this drawback, more complex variants of this method have been proposed. However, a formulation able to guarantee a stable simulation for an arbitrary choice of the input parameter values has not been achieved yet.

**Volume-of-Fluid method**

The Volume-of-Fluid (VoF), Level-Set (LS) and Front-Tracking (FT) methods have a common underlying approach to solve the hydrodynamics of gas-liquid flows. For all these numerical techniques, the motion of the interface across the computational grid, on which the governing equations are solved, is computed.

In the Volume-of-Fluid method (Hirt and Nichols, 1981), the dynamics of the interface is based on the so-called topological equation for the liquid phase which provides the volume fraction function $f$. The value of $f$ represents the fraction of the cell volume occupied by the liquid. The topological equation is solved in a "geometrical" manner (see Rudman, 1997, Rider and Kothe, 1998) which allows

to maintain remarkably well the sharpness of the interface. This kind of solution needs to be coupled to an interface reconstruction procedure. The Piecewise Linear Interface Calculation (PLIC) algorithm is usally adopted for this purpose. This algorithm represents the interface by means of lines (in 2D) and planes (in 3D). An example of a PLIC reconstruction is given in Fig. 2.3. Due to the computational cost of this operation, the VoF method with PLIC reconstruction is used in the majority of the cases on Cartesian grids. Meshes with generic polyhedral cells have been adopted in Ahn and Shashkov (2007) and Maric et al. (2013).

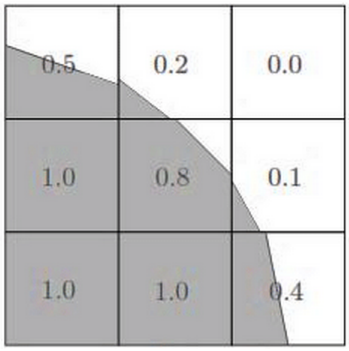


Figure 2.3: Example of Piecewise Linear Interface Calculation: the numbers within the cells represents the volume fraction function values.

An alternative to circumvent the complexity of the interface reconstruction is provided by the algebraic VoF. In this variant of the method, the topological equation is solved by means of differencing schemes. The central aspect of the algebraic VoF is the differencing scheme adopted to discretise the convection term. It is well known that traditional schemes such as the upwind, downwind and central schemes are not able to provide at the same time a stable and sharp solution In the last decades, several novel numerical schemes have been developed which are based on non-linear blendings of the traditional ones. The blendings allow to combine their positive features and limit their drawbacks. Among these novel schemes, the High Resolution Interface Capturing (HRIC) by Muzaferija and Perić (1999), the Compressive Interface Capturing Scheme for Arbitrary Meshes (CICSAM) by Ubbink and Issa (1999) and the Tangent of Hyperbola for Interface Capturing (THINC) have shown the best performances.

**Level-Set method**

The Level-Set method has been developed by Osher and Sethian (1988) to capture the motion of a generic interface. Sussman et al. (1994) have applied for the first time this numerical technique for the simulation of two-phase flows. In the LS method, the interface is given by the zero level set of a smooth scalar function $\phi(\mathbf{x}, t)$. The exact position corresponding to the condition $\phi(\mathbf{x}, t) = 0$ is determined by interpolating the values of $\phi$ at the grid points. Values of $\phi$ greater than zero are found in the liquid, while values less than zero indicate the gas. The function $\phi$ is usually initialized as the signed distance from the interface. The dynamics of the interface is given by the so-called Level-Set

equation which is solved by means of high-order numerical schemes. However, $\phi$ differs in general from the signed distance function after the solution of this equation. When the deviation is considerable, inaccurate calculations of the normal vector and the curvature of the interface and severe mass conservation errors can occur. In order to alleviate these problems, the Level-Set equation is followed by a re-initialization step.

Differently from the VoF, the LS method is able to generate a connected interface. Furthermore, the computational cost of the method benefits from the absence of complex reconstruction algorithms. A further important advantage is the ability to handle topological changes due to bubble coalescence or breakup phenomena in a simple way.

**Front-Tracking method**

The Front-Tracking method (Unverdi and Tryggvason, 1992) takes inspiration from the Peskin's Immersed Boundary (IB) method (Peskin, 1977) originally developed for simulations of blood flow in the heart. Peskin's idea was to track the motion of a boundary surface represented by a discrete data structure. Unverdi and Tryggvason extended this approach to the case of moving interfaces consisting of a set of logically connected Lagrangian marker particles. The generic particle $p$ with position $\mathbf{x}_p$ is advected according to

$$\frac{d\mathbf{x}_p}{dt} = \mathbf{u}_p, \tag{2.7}$$

where $\mathbf{u}_p$ is the flow velocity at $\mathbf{x}_p$ obtained by interpolation of the grid nodal values.

Accumulations and rarefactions of the marker particles can occur during the simulation leading to a non-uniform distribution of these objects along the interface. In order to guarantee an appropriate resolution everywhere, a remeshing procedure, through which marker particles are added or removed, is usually adopted.

Similarly to LS, the FT method produces an accurate and continuous representation of the interface. A major advantage of this numerical technique is the reduced computational time which allows to perform simulations of large systems of multiple bubbles. Nevertheless, the method presents difficulties in dealing with topological changes induced by bubble coalescence and breakup. This requires a special treatment of the merging and splitting of the data structures corresponding to different bubbles. In this respect, progress has been achieved by Torres and Brackbill (2000), Shin and Juric (2002, 2009).

An inherent volume (and mass) conservation is not ensured. Special measures have to be adopted in order to limit this issue (see Dijkhuizen et al., 2010, Roghair et al., 2016).

**Arbitrary Lagrangian-Eulerian Interface-Tracking method**

The Arbitrary Lagrangian-Eulerian (ALE) Interface-Tracking method relies on a different approach to solve the gas-liquid flows. This method does not track or reconstruct the motion of the interface across the computational domain, as it happens in the VoF, LS and FT methods. On the contrary, the interface is here a part of the computational mesh. It consists of a set of edges (in 2D) and faces

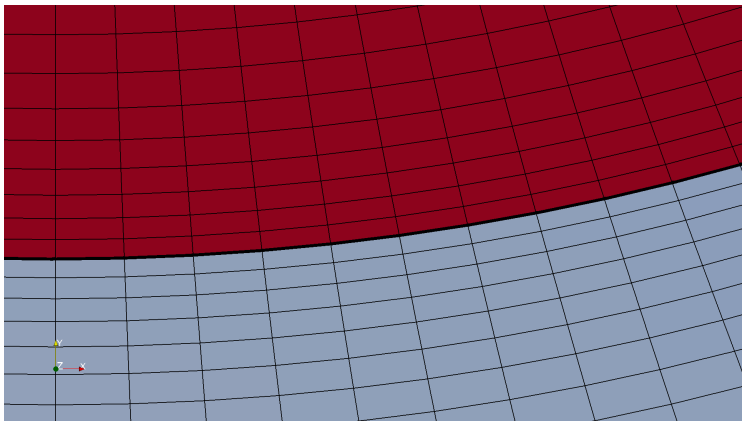

Figure 2.4: Domain discretisation in the ALE Interface-Tracking method: the colored regions correspond to the two phases, the thicker black line represents the interface.

(in 3D) and it connects the two regions corresponding to the liquid and gas phases serving as a boundary.

The motion of the interface during the simulation results from the solution of the complete set of equations, i.e. the mass and momentum equations and the transmission conditions. The interior parts of the grid are not fixed as well and they are displaced according to the interface movement. However, strong distortions of the mesh elements and/or large modifications of the cell aspect ratios might occur if the interface is subjected to significant deformations. For this reason, remeshing steps are often necessary in order to restore a good mesh quality.

The treatment of the interface as a boundary provides the possibility to accurately enforce the transmission/jump conditions without the need to incorporate them into the governing equations as for the previous methods. Furthermore, the ALE Interface-Tracking method represents the best framework for the simulation of all the phenomena that involve a transport along the interface, e.g. surfactants.

One main drawback of the method is the difficulty to deal with bubble coalescence and breakup. The resulting topological changes require complex and computationally expensive algorithms (see Quan et al., 2009).

### 2.2.2 Overview of the literature on transfer phenomena in gas-liquid flows

An overview of the numerous numerical studies relavant to the present work is given in this section. Various problems concerning transfer phenomena in gas-liquid flows present strong similarities with the reactive mass transfer processes considered here. In addition to the two-phase hydrodynamics, these problems also involve the transport of additional quantities such as surfactants, energy, ionic species, etc. These quantities and the chemical components in chemisorption processes share similar transport mechanisms. Furthermore, both are often characterized by thin boundary layers at the interface. The literature overview has been subdiveded in various topics, each corresponding to a specific transfer phenomenon.

## 2. Literature Survey

**Physisorption**

The physical mass transfer from single freely rising bubbles has been intensively investigated in the last two decades. One of the first relevant studies has been carried out by Davidson and Rudman (2002). They performed 2D planar and axisymmetric VoF simulations with the so-called two-scalar method. This approach considers two scalar fields for each dissolving species. Given the concentration $c(\mathbf{x}, t)$, the first scalar field is equal to $c(\mathbf{x}, t)$ in the liquid region and takes a zero value in the gas region, while the reverse occurs for the second scalar field. Bothe et al. (2004) developed in the VoF framework a one-scalar formulation. They performed 2D simulations of the dissolution of oxygen from air bubbles rising in water or aqueous solutions. However, this formulation yields artificial mass transfer.

3D computations using the FT method with a maximum Schmidt number of 1 are reported in the work of Darmana et al. (2006). In this work, the transport resistance in the gas has been neglected and, therefore, the transport equations for the species have been solved only in the liquid. Darmana (2006) simulated also clusters of rising bubbles by means of the same method and he compared the resulting mass transfer rates to those ones of the single bubbles.

Desphande and Zimmerman (2006) employed a LS method to investigate the mass transfer from buoyancy driven droplets. The species transport in both the phases has been taken into account. The authors compared their results for low Reynolds values to empirical correlations for the Sherwood number. It emerged that the simulations underestimates the Sherwood by roughly 25%. Onea et al. (2009) used a one-scalar approach similar to that one presented in Bothe et al. (2004) for simulations of the mass transfer from Taylor bubbles at low Schmidt numbers. The same approach has been adopted by Francois and Carlson (2010) to study the physisorption processes in the surface tension dominated regime. Simulations of fixed-shape single rising bubbles with Schmidt numbers up to 300 have been carried out by Figueroa-Espinoza and Legendre (2010). They assessed the influence of different wakes on the mass transfer by analysing the profiles of the local Sherwood number along the bubble surface.

Marschall et al. (2012) developed within the algebraic VoF framework a single-field model known as *Continuous Species Transfer* (CST) by means of the conditional volume averaging technique. Haroun et al. (2010) too adopted averaged species transport equations in their computations of falling films. These two methods have been combined in an unified model by Deising et al. (2016).

In order to simulate the very thin concentration boundary layers corresponding to high Schmidt numbers, Alke et al. (2010) introduced within the VoF framework a subgrid-scale model based on the analytical solution of the mass transfer for an overflown planar and mobile interface. A different subgrid-scale approach for physisorption problems in 2D flows for the FT method has been developed by Aboulhasanzadeh et al. (2012). In this approach, the solution of a simplified species transport equation valid only for the boundary layer provides as a source term the amount of the dissolving species entering into the bulk. The extension to the 3D case has been presented in Aboulhasanzadeh et al. (2013). Bothe et al. (2011) and Bothe and Fleckenstein (2013) applied the subgrid-scale model of Alke et al. (2010) to 3D cases of physical mass transfer from single rising bubbles. The maximum value of the Péclet number was about $2 \cdot 10^5$ (Bothe and Fleckenstein). Although it was shown that the adoption of this model improves considerably the accuracy of the results, still significant devi-

ations from the Sherwood values predicted by correlations in the literature have been observed for such large Péclet numbers. Weiner and Bothe (2017) proposed an enhanced version of this approach in which the numerical fluxes across all the faces of the interface cells are corrected according to the local subgrid-scale concentration profile. This modification allowed to obtain a better agreement with the Sherwood correlations up to the Péclet value of $4 \cdot 10^6$.

A Dirichlet-Neumann coupling algorithm for interfacial transfer phenomena within the ALE Interface-Tracking framework has been developed by Weber et al. (2017). The method has been validated for low Reynolds numbers up to the Péclet value of $10^5$. Furthermore, it has been applied to more deformed bubbles with maximum Péclet equal to $4 \cdot 10^4$. This work represents the first attempt to investigate the mass transfer from single rising bubbles by means of the ALE Interface-Tracking method.

In the above cited analyses, the change of the bubble volume due to the mass transfer has been neglected. Few studies have taken into account these effects. In Juncu's (2011) mass transfer simulations of spherical bubbles, an uniform concentration in the gas phase is assumed for the dissolving components. At each time step the sphere radius is computed from the remaining species amount inside the bubble. Local volume changes resulting from non-uniform concentration fields in the gas have been tackled by Hayashi and Tomiyama (2011). They carried out 2D VoF simulations of the dissolution of carbon dioxide bubbles. Fleckenstein and Bothe (2015) extended their method presented in Bothe and Fleckenstein (2013) in order to account for multi-component mass transfer and the resulting volume effects. The new method has been adopted to simulate the shrinking of a Taylor bubble in a square channel and the mass transfer from a multi-component gas bubble. In both the cases, only a quarter of the fluid domain has been computed by using two symmetry planes.

**Chemisorption**

Regarding the chemisorption of a dilute species at single freely rising bubbles, early relevant numerical investigations are reported in Khinast (2001), Khinast et al. (2003), Koynov et al. (2004) and Raffensberger et al. (2005). These analyses are focused on the impact of the bubble-wake dynamics on the selectivity of different prototypical reactive systems. A 2D cylindrical model with the bubble shape fixed a priori has been employed throughout all these studies. Furthermore, the concentration of the dissolving species has been assumed to be uniform inside the gas phase, neglecting the internal transport resistance. Koynov et al. (2005) accounted for the deformation of the bubble surface by means of a hybrid Front-Tracking/Front-Capturing method (Tryggvason et al., 2001). They carried out 2D reactive mass transfer simulations of small bubble groups and they compared the resulting mass transfer rates and reaction selectivities to those ones of single rising bubbles. Radl et al. (2008) adopted the same numerical method to investigate the selectivity of the catalytic hydrogenation of nitroarenes. Both single bubbles and bubble clusters have been simulated. The maximum Schmidt number has been chosen equal to 100 and moderate to fast reactions have been considered. The results have been compared to the film theory predictions.

The transport resistance in the gas phase has been taken into account in Kröger et al. (2007), Alke et al. (2009), Bothe et al. (2009) and Bothe et al. (2011). The last work employed the subgrid-scale model developed in Alke et al. (2010) for 2D computations of chemisorption processes. Although this

model is designed for physisorption problems, the study showed that it can be also successfully applied to reactive cases. A reactive version of this subgrid-scale model has been developed in Gründing et al. (2016) for an uncoupled single reaction in which the reaction source term depends solely on the dissolved species concentration. The method has been validated against a 3D reactive Stokes flow around a rising spherical bubbble, but so far it has not been applied to high Péclet number cases. Furthermore, this approach is currently restricted to first-order single reaction and further development would be required to extend its applicability to more complex mechanisms.

The mass transfer accompanied by a first-order reaction from a single bubble in creeping flow with changing volume has been tackled by Juncu (2012). A time-dependent uniform concentration for the dissolving species has been considered inside the bubble. Different Péclet numbers and chemical reaction velocities have been simulated in order to assess their influence on the mass transfer rate. A first-order reaction has been also taken into account in the work of Roghair et al. (2016) who carried out reactive mass transfer simulations of bubble groups by means of an FT technique.

**Surfactants**

A first study on the influence of surfactants on the bubble dynamics has been carried out by Gorodetskaya (1949) who investigated the change of the rise velocity of air bubbles in aqueous solutions due to different concentrations of alcohols. Stuke (1952) carried out similar analyses with oxygen bubbles rising in clean and contaminated water. In the case of contamination, he observed a significant difference of the surface tension values between the front and the rear of the bubble. The occurrence of this gap is due to the capability of the surfactants to lower the surface tension. Due to the rising motion of the bubble, the surfactant molecules adsorbed at the fluid interface are accumulated in the rear part of the surface leading to a decrease of the surface tension in this region and, accordingly, to profound modifications of the two-phase hydrodynamics. In particular, a remarkable consequence is the local stiffening of the interface which behaves as a rigid surface in the rear of the bubble.

A complex aspect regarding the simulation of surfactants is the numerical treatment of the transport of these compounds along the interface. This involves the solution of differential equations on a curved manifold. Early numerical techniques neglected this transport and accounted for the presence of surfactants at the interface by means of the so-called stagnant cap models (see Fdhila and Duineveld, 1996, Zhang et al., 2001, Palaparthi et al., 2006). In recent years, more sophisticated techniques, which do not rely on these simplifications, have been developed. However, these simulations still represent a very challenging task. In particular, methods with non-continuous or smeared representations of the interface like the VoF with PLIC reconstruction and the algebraic VoF present difficulties in dealing with these problems. Nevertheless, some examples of VoF methods able to simulate these phenomena can be found in Renardy et al. (2002), James and Lowengrub (2004) and Alke and Bothe (2009). While the first two numerical techniques are for 2D flows only, the method of Alke and Bothe, which solves the interfacial surfactant transport on an iso-surface of the volume fraction $f$, allows for 3D simulations.

Further numerical issues are encountered when soluble surfactants are considered. In this case, the presence of adsorption and desorption processes determines a coupling between the transport of

the surfactant in the bulk and along the interface. Due to the very low diffusion coefficients of these compounds, their concentration boundary layers at the interface are extremely thin and, therefore, they require a very fine numerical resolution. Several studies have limited the computational demands considering 2D problems only (see Fujioka, 2013, Khatri and Tornberg, 2014, Chen and Lai, 2013, Booty and Siegel, 2010). The last work was extended in Wang et al. (2014) to the 3D axisymmetric case. Axisymmetric simulations were also performed in Muradoglu and Tryggvason (2008) by means of a FT method and in Ganesan and Tobiska (2012) by means of an ALE finite-element method.

3D finite-difference FT computations have been carried out by Muradoglu and Tryggvason (2014) who investigated the effects of soluble surfactants on the bouyancy-driven motion of single bubbles in a tube. Furthermore, they analysed the lateral migration of single bubbles in a pressure-driven channel flow. The maximum Péclet number in this work is about 1000. Pesci et al. (2018) performed 3D simulations of single rising bubbles in contaminated solutions by means of an ALE Interface-Tracking method. A subgrid-scale model has been employed to capture the very large concentration gradients at the interface with a reduced mesh resolution and, accordingly, a lower computational cost. The bubble rising velocity transients provided by the computations are in good agreement with experimental results. The effects of soluble surfactants on the lift coefficient of bubbles in linear shear flows were analysed by Hayashi and Tomiyama (2017) by means of 3D LS simulations. The maximum Reynolds and Péclet numbers are about 70 and $4.5 \cdot 10^5$, respectively. Symmetry conditions have been enforced on a longitudinal plane crossing the bubble center allowing for simulations of only half of the domain.

Due to their influence on the two-phase hydrodynamics, the surfactants can significantly affect the mass transfer from gas bubbles. Furthermore, the presence of these compounds at the interface can cause a hindrance effect, as reported by Clift et al. (1978). Few numerical studies have been dedicated to this topic. Takemura and Yabe (1999) performed both experiments and numerical simulations of mass transfer from carbon dioxide bubbles in contaminated water for Reynolds numbers less than 100. The influence of the surfactants in their axisymmetric computations has been taken into account by means of a stagnant cap model with successful agreement to the experimental measurements. Similar analyses are reported in Takemura and Matsumoto (2000) who investigated the mass transfer accompanied by chemical reactions of carbon dioxide bubbles in sodium hydroxide solutions. Further axisymmetric simulations of mass transfer from contaminated fluid spherical particles with a stagnant cap model have been presented by Saboni et al. (2011). The work pointed out that higher surface contaminations corresponding to larger stagnant cap angles lead to lower mass transfer rates. Furthermore, the authors proposed Sherwood number correlations including the influence of the stagnant cap angle.

**Phase-change phenomena**

Similar to the previous topics, numerical simulations of phase-change phenomena such as evaporation, boiling, condensation, etc., present complex aspects. In particular, these computations require an accurate solution of the energy equation in order to satisfactorily determine the phase-change rates. An early VoF-based approach has been presented by Welch and Wilson (2000) who performed 2D simulations of horizontal film boiling. The mass transfer rate is calculated from the heat flux at

the liquid-vapor interface. Film boiling problems have been also investigated by Welch and Rachidi (2002) who additionally considered the conjugate heat transfer between the solid wall and the boiling fluid. Agarwal et al. (2004) extended the work of Welch and Rachidi (2002) to the case of variable thermal properties. They computed unsteady, periodic bubble release in 2D film boiling. Spherically symmetric simulations of spherical bubble growth have been carried out by Ghosh et al. (2006, 2009) by means of a VoF-based method. Akhtar and Kleis (2011) performed 3D simulations of spherical bubble growth. However, they were not able to avoid interface deformations. Another VoF-based numerical study regarding phase-change problems is reported in Yuan et al. (2008) who adopted a body-fitted coordinate system in order to compute film boiling from a horizontal cylinder. Hardt and Wondra (2008) proposed an evaporation model for vapor-liquid flows within the VoF framework. They validated their model against 1D evaporation problems for which (semi-)analytical solutions are available and, then, they applied it to a 2D film boiling case. Kunkelmann and Stephan (2009) included in the last approach a subgrid-scale model for the contact line evaporation which cannot be resolved by the numerical grid due to undue mesh resolution requirements. A VoF-based method for the simulations of evaporating, stongly deforming droplets in incompressible flows has been developed by Schlottke and Weigand (2008). After having validated the method against various test cases, they considered a 3D evaporation problem of a water droplet in dry air at a Reynolds number about 1500. A local grid refinement technique has been adopted by Strotos et al. (2011) for computations of multi-component droplet evaporation in a hot air environment under forced convection. Ma and Bothe (2013) employed a two-scalar approach for the temperature in VoF simulations of evaporating thin liquid films over heated substrates including the Marangoni effect. The results are in qualitative agreement with the experimental measurements. Sato and Ničeno (2013) applied a new sharp-interface phase-change model to 3D simulations of nucleate pool boiling. In this numerical approach, after the transport of a smooth volume fraction function, an interface sharpening equation (see Olsson and Kreiss, 2005) is solved in order to reduce the smearing.

A LS-based "ghost-fluid" method for phase-change problems has been presented by Gibou et al. (2007). They performed computations of two-dimensional film boiling. LS-based "ghost-fluid" methods have been also proposed by Tanguy et al. (2007) and Houim and Kuo (2013). In the former work, the authors simulated the vaporization of axisymmetric static and moving droplets in air. The interaction between a shock wave and a vaporizing aluminum droplet has been analysed in the latter one. Can and Prosperetti (2012) developed a phase-change model within the LS framework to investigate vapor bubble dynamics. The velocity and temperature fields in the vapor are not computed following the assumption of uniform pressure in this phase. A coupled LS-VoF method is reported in Tomar et al. (2005). 2D computations of bubble growth in film boiling highlighted the capability of the method to both conserve mass and handle complex interface topologies accurately.

2D film boiling computations have been carried out by Juric and Tryggvason (1998) by means of a FT technique. This method has been improved in Esmaeeli and Tryggvason (2004) and tested against a case of film boiling on a horizontal surface. Shin and Juric (2000) and Al-Rawahi and Tryggvason (2002) adopted a 2D dimensional FT method for investigating the effects of fluid flow on dendritic solidification.

## 2.3 Objectives of the thesis

Although several studies have been already dedicated to the numerical investigation of reactive mass transfer processes in single bubble systems, as reported in the previous section, a systematic study of the interaction between mass transfer, chemical reactions and two-phase hydrodynamics has not been carried out yet. Furthermore, past studies have been restricted to fixed-shape and/or 2D bubble models (see Khinast, 2001, Khinast et al., 2003, Koynov et al., 2004, Radl et al., 2008). The aim of the present research was to thoroughly investigate by means of 3D Direct Numerical Simulations the influence on the mass transfer from single risingle bubbles of:

- different hydrodynamic conditions with regard to bubble shape and wake corresponding to technically relevant bubble diameters;
- different chemical reaction intensities ranging from very slow to fast reactions;
- different dissolving species diffusivities.

Two distinct reaction prototypes representative of many chemical engineering applications based on bubble column reactors have been considered.

The analysis has been focused on two quantities: the mass transfer coefficient and the reaction selectivity. The former expresses the transfer efficiency of the unit interfacial area. The latter measures to which extent the dissolving species reacts to the desired product. Therefore, high values of these two quantities are crucial in order to achieve high conversion rates and limit the formation of side-products in bubble column reactors. A very important aspect of the present work was to understand whether and how the mass transfer coefficient and the reaction selectivity are affected by different relevant parameters and to disclose local mechanisms governing the behavior of these global quantities. This analysis is of particular relevance for bubble column reactors with homogeneous flow conditions in which the bubble-bubble interaction effects are of minor importance.

As already pointed out in Chapter 1, severe computational issues result from the multiscale characteristic of the mass transfer phenomena. In order to tackle them, the numerical solution strategy has been based on the decoupling of the two-phase hydrodynamics and the species concentration transport equations. More precisely, different numerical resolutions have been adopted for these two problems in order to limit the overall computational cost. The development of an accurate and efficient novel numerical method for solving the species concentration transport equations was one the main objective of this work. This method has then been coupled to a two-phase hydrodynamics ALE Interface-Tracking solver (Tuković and Jasak, 2012) which, as outlined in Section 2.2.1, provides an accurate representation of the interface and enables a direct enforcement of the jump/transmission conditions. A more detailed description of the ALE Interface-Tracking is given in Section 4.1.

The design of bubble column reactors often relies on simplified models. Among them, the film theory is undoubtedly the most adopted one. In the last part of the work, the accuracy of the film theory predictions for the considered reaction prototypes has been assessed by quantifying the discrepancies of this model from the results of the 3D numerical simulations.

# Chapter 3

# Mathematical model for gas-liquid flows with reactive species transfer

A continuum sharp interface model has been employed to describe the motion of a gas bubble in a liquid. This model consists of the mass and momentum conservation equations for each phase and two transmission conditions at the interface which is assumed to have zero thickness.

A competitive-consecutive prototype made up of two second-order irreversible reactions has been considered. The first reaction yields the desired product denoted with the letter $P$, while the second one is responsible for the creation of the side-product $S$. For this reason, it is also referred to as side-reaction. This mechanism is representative of many different chemical engineering applications based on bubble column reactors, e.g. chlorination of paraffins, hydrogenation of nitroarenes.

Additional differential equations and transmission conditions describing the transport of the species of the competitive-consecutive prototype have been included into the model. However, the influence of these components on the two-phase flow hydrodynamics has been neglected. For this reason, the mass transfer shoud be more properly referred to as species transfer.

A single reaction prototype made up of the first reaction of the competitive-consecutive mechanism has been also taken into account. However, since the species of this prototype represent a subset of those ones involved in the competitive-consecutive mechanism, the mathematical model is presented here with reference to the latter reactive system only.

## 3.1 Two-phase flow hydrodynamics

An incompressible isothermal flow of two Newtonian fluids with uniform density has been assumed. The Navier-Stokes equations for this two-phase system read

$$\nabla \cdot \mathbf{v} = 0, \tag{3.1}$$

$$\frac{\partial}{\partial t}(\rho \mathbf{v}) + \nabla \cdot (\rho \mathbf{v} \otimes \mathbf{v}) = -\nabla p + \nabla \cdot \mathbf{S} + \rho \mathbf{g}, \tag{3.2}$$

with fluid velocity $\mathbf{v}$, density $\rho$, pressure $p$ and gravity acceleration $\mathbf{g}$. The viscous stress tensor $\mathbf{S}$ is given as

$$\mathbf{S} = \mu(\nabla \mathbf{v} + \nabla \mathbf{v}^{\mathrm{T}}), \tag{3.3}$$

where $\mu$ represents the dynamic viscosity.

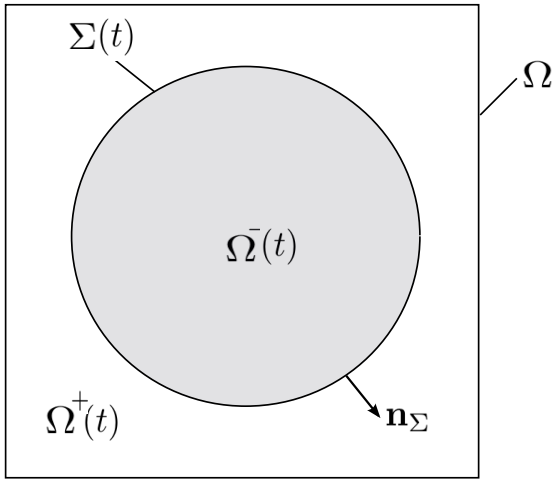


Figure 3.1: Sketch of the physical domain.

Eqs. (3.1) and (3.2) are valid in the domain $\Omega{=}\Omega^+(t) \cup \Omega^-(t)$ with the two disjoint open sets $\Omega^+(t)$ and $\Omega^-(t)$ corresponding to the liquid and gas phases, respectively. The mass and momentum transmission conditions

$$[\![\mathbf{v}]\!] = 0, \tag{3.4}$$

$$[\![p\mathbf{I} - \mathbf{S}]\!] \cdot \mathbf{n}_\Sigma = \sigma \kappa \mathbf{n}_\Sigma \tag{3.5}$$

are enforced at the interface $\Sigma(t)$, where $\sigma$ is the surface tension coefficient and $\kappa$ represents the total curvature of the interface. $\kappa$ is computed as $-\nabla_\Sigma \cdot \mathbf{n}_\Sigma$, where $\nabla_\Sigma$ is the surface gradient operator. The notation

$$[\![\phi]\!](\mathbf{x}) = \lim_{h \to 0^+} (\phi(\mathbf{x} + h\mathbf{n}_\Sigma) - \phi(\mathbf{x} - h\mathbf{n}_\Sigma)) = \phi^+ - \phi^- \tag{3.6}$$

denotes the jump of a generic quantity $\phi$ at a point $\mathbf{x}$ of the interface with unit normal vector $\mathbf{n}_\Sigma$. Eq. (3.4) follows from the continuity of the normal and tangential components of the velocity at the phase boundary, resulting from the assumptions of no phase change and no interfacial slip. The additional term $\nabla_\Sigma \sigma$ is neglected in Eq. (3.5) by assuming that surface gradients of the surface tension coefficient are not present.

Last remark regards the velocity boundary condition at infinite distance from the interface. The assumption of quiescent liquid imposes that the velocity $\mathbf{v}(|\mathbf{x}| \to \infty, t)$ is equal to $\mathbf{0}$ $\forall t \in [0, +\infty)$.

### 3.1.1 Relevant nondimensional numbers

By means of the bubble diameter $d_b$, bubble rising velocity $U_b$, liquid density $\rho_l$, liquid viscosity $\mu_l$ and the absolute value of the gravity acceleration $g$, the following nondimensionalizations

$$\tilde{t} = \frac{U_b}{d_b}t, \quad \tilde{\mathbf{x}} = \frac{x}{d_b}, \quad \tilde{\mathbf{v}} = \frac{\mathbf{v}}{U_b}, \quad \tilde{\rho} = \frac{\rho}{\rho_l}, \quad \tilde{p} = \frac{p}{\rho_l U_b^2}, \quad \tilde{\mu} = \frac{\mu}{\mu_l}, \quad \tilde{\mathbf{g}} = \frac{\mathbf{g}}{g}, \quad \tilde{\mathbf{S}} = \frac{d_b}{\mu_l U_b}\mathbf{S} \tag{3.7}$$

are obtained. Inserting these expressions in Eqs. (3.1) and (3.2), the mass and momentum conservation equations can be rewritten in a nondimensional form as follows

$$\tilde{\nabla} \cdot \tilde{\mathbf{v}} = 0, \tag{3.8}$$

$$\frac{\partial}{\partial \tilde{t}}(\tilde{\rho}\tilde{\mathbf{v}}) + \tilde{\nabla} \cdot (\tilde{\rho}\tilde{\mathbf{v}} \otimes \tilde{\mathbf{v}}) = -\tilde{\nabla}\tilde{p} + \frac{1}{\mathrm{Re}_b}\tilde{\nabla} \cdot [\tilde{\mu}(\tilde{\nabla}\tilde{\mathbf{v}} + \tilde{\nabla}\tilde{\mathbf{v}}^{\mathrm{T}})] + \frac{1}{\mathrm{Fr}}\tilde{\rho}\tilde{\mathbf{g}}, \tag{3.9}$$

where both $\tilde{\rho}$ and $\tilde{\mu}$ are equal to 1 in the liquid phase, while their values in the gas phase are $\rho_g/\rho_l$ and $\mu_g/\mu_l$, respectively. The quantities $\rho_g$ and $\mu_g$ represent the gas density and viscosity. Eqs. (3.8) and (3.9) depend on four nondimensional numbers: the bubble Reynolds number $\mathrm{Re}_b{=}\rho_l U_b d_b/\mu_l$, the Froude number $\mathrm{Fr}{=}U_b^2/g d_b$, the viscosity ratio $\Gamma{=}\mu_g/\mu_l$ and the density ratio $\gamma{=}\rho_g/\rho_l$. The bubble Reynolds number expresses the ratio between inertia and viscous forces, while the Froude number measures the relative strength of inertia and gravity forces. With the additional rescaling of the total curvature $\tilde{\kappa}{=}\kappa d_b$, the nondimensional transmission conditions read

$$[\![\tilde{\mathbf{v}}]\!] = 0, \tag{3.10}$$

$$[\![\tilde{p}\mathbf{I} - \frac{1}{\mathrm{Re}_b}\tilde{\mu}(\tilde{\nabla}\tilde{\mathbf{v}} + \tilde{\nabla}\tilde{\mathbf{v}}^{\mathrm{T}})]\!] \cdot \mathbf{n}_\Sigma = \frac{1}{\mathrm{We}}\tilde{\kappa}\mathbf{n}_\Sigma. \tag{3.11}$$

Eq. (3.11) introduces the Weber number $\mathrm{We}{=}\rho_l d_b U_b^2/\sigma$ which represents the ratio between inertia and surface tension forces.

For gas-liquid systems, the Weber and Froude numbers are usually replaced by the Eötvös $\mathrm{Eo}{=}(1-\gamma)\mathrm{We}/\mathrm{Fr}{=}g(\rho_l-\rho_g)d_b^2/\sigma$ and the Morton $\mathrm{Mo}{=}(1-\gamma)\mathrm{We}^3/\mathrm{FrRe}_b^4{=}g(\rho_l-\rho_g)\mu_l^4/\rho_l^2\sigma^3$ numbers. The former one expresses the ratio between buoyancy and surface tension forces. The latter one involves only fluid properties. Thus, it becomes particularly useful if fixed material properties for the liquid and gas fluids are considered.

## 3.2 Reactive species transfer

The competitive-consecutive reaction prototype is made up of the following two second-order irreversible reactions

$$\begin{aligned} R_1 &: A + B \to P \quad \text{with rate} \quad r_1 = k_1 c_A c_B, \\ R_2 &: P + B \to S \quad \text{with rate} \quad r_2 = k_2 c_P c_B, \end{aligned} \tag{3.12}$$

where $B$ is the component dissolving from the gas into the liquid, $A$ is present only in the liquid phase, $P$ and $S$ are the product and the side-product of the chemical reactions, $r_1$ and $r_2$ are the two reaction rates, $k_1$ and $k_2$ represent the corresponding reaction coefficients and $c_k$ denotes the concentration of the generic species $k$ in the reacting system.

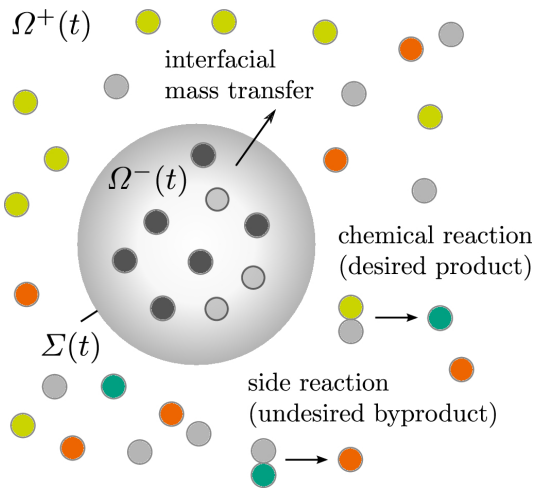


Figure 3.2: Schematic of the reactive mass transfer process relating to the competitive-consecutive reaction mechanism: grey circles denote the dissolving component $B$, yellow circles the liquid component $A$, teal circles the product $P$ and orange circles the side-product $S$.

Assuming that all the species are diluted, the transport equation for the generic chemical component $k$ with diffusion coefficient $D_k$ and stoichiometric coefficients $\nu_{k,i}$, $i$=1, 2 reads

$$\frac{\partial c_k}{\partial t} + \nabla \cdot (c_k \mathbf{v}) = D_k \Delta c_k + \sum_{i=1,2} \nu_{k,i} r_i. \tag{3.13}$$

Eq. (3.13) is valid throughout the domain except for the interface. Regarding the species $B$, discontinuities in the concentration and its normal gradient occur at $\Sigma$. The first discontinuity is related to the different solubility of this component in the liquid and gas phases, respectively. The second one is instead due to the difference in the values of the diffusion coefficient. The mathematical formulations of these two conditions are

$$c_B^+ = \mathrm{H}_B c_B^-, \tag{3.14}$$

$$[\![ \mathbf{n}_\Sigma \cdot (D_B \nabla c_B) ]\!] = 0. \tag{3.15}$$

Eq. (3.14) is known as Henry's law and the coefficient $\mathrm{H}_B$ is the Henry coefficient. In general, it is a function of different quantities, e.g., temperature, pressure, etc. Here, a constant Henry coefficient, which is a good approximation in many technically relevant cases, is assumed. The balance between the normal diffusive fluxes in the transmission condition (3.15) enforces that the amount of $B$ leaving one phase is released at the other one. Eqs. (3.14) and (3.15) are obtained under the assumption of low to moderate mass transfer rates of a dilute gaseous component from a rising gas bubble in an aqueous solution, as found in bubble column reactors.

Regarding the species $A$, $P$ and $S$, Eqs. (3.14) and (3.15) are replaced by a zero normal gradient condition. This enforces no back-dissolution into the gas phase, restricting the presence of these species to the liquid domain. Accordingly, the chemical reactions can take place only in this region.

The species $A$ and $B$ are initialized to some values in the liquid and gas phases, respectively. These values will be specified later. The initial concentration of $P$ and $S$ is 0 $\mathrm{mol/m^3}$ in the entire domain.

### 3.2.1 Relevant nondimensional numbers

The nondimensional form of Eq. (3.13),

$$\frac{\partial}{\partial \tilde{t}}\tilde{c}_k + \tilde{\nabla}\cdot(\tilde{c}_k\tilde{\mathbf{v}}) = \frac{1}{\mathrm{Pe}_k}\tilde{D}_k\tilde{\nabla}^2\tilde{c}_k + \sum_{i=1,2}\nu_{k,i}\tilde{r}_i, \tag{3.16}$$

is obtained with the following nondimensionalizations:

$$\tilde{c}_k = \frac{c_k}{c_{A,\infty}}, \quad \tilde{D}_k = \frac{D_k}{D_{k,l}}, \quad \tilde{r}_1 = \mathrm{Da}_1\tilde{c}_A\tilde{c}_B, \quad \tilde{r}_2 = \mathrm{Da}_2\tilde{c}_P\tilde{c}_B, \tag{3.17}$$

where $D_{k,l}$ is the diffusion coefficient of the species $k$ in the liquid phase and $c_{A,\infty}$ is the concentration of the species $A$ at infinite distance from the interface.

Eq. (3.16) introduces the Péclet number,

$$\mathrm{Pe}_k = \frac{U_b d_b}{D_{k,l}} = \frac{\rho_l U_b d_b}{\mu_l}\frac{\mu_l}{\rho_l D_{k,l}} = \mathrm{Re}_b\mathrm{Sc}_k, \tag{3.18}$$

which is the ratio of inertial forces to species diffusion. As shown in Eq. (3.18), the Péclet number is given by the product of the Reynolds and Schmidt numbers, where the latter one is the ratio between the liquid viscosity and the species diffusion coefficient in the liquid phase.

The dimensionless number in the last two formulas of Eq. (3.17) is the Damköhler number which compares the hydrodynamic and chemical time scales. For the first and second reaction, respectively, it is defined as follows

$$\mathrm{Da}_1 = \frac{d_b k_1 c_{A,\infty}}{U_b}, \quad \mathrm{Da}_2 = \frac{d_b k_2 c_{A,\infty}}{U_b}. \tag{3.19}$$

Different expressions of this dimensionless parameter are reported in the literature. The expression used in Eq. (3.19) corresponds to the so-called first Damköhler number $\mathrm{Da}^{\mathrm{I}}$. In this thesis, we refer

to this formulation, omitting the superscript for simplicity.

The coefficient $\tilde{D}_k$ in Eq. (3.16) is equal to 1 in the liquid phase and to $D_{k,g}/D_{k,l}$ inside the bubble. This ratio between the species diffusion coefficients in both the phases represents the last relevant dimensionless number of the reactive species transfer problem.

### 3.2.2 Target quantities

The attention has been focused on the following reaction engineering quantities: the Sherwood number Sh, the mass transfer coefficient $\beta_l$ and the reaction selectivity $S$ toward the product $P$. The reactive species transfer processes have been investigated by means of both the global and the local variants of these quantities.

The Sherwood number is defined as follows

$$\mathrm{Sh} = \frac{1}{|S_\Sigma|} \int_{S_\Sigma} \frac{\mathbf{n}_\Sigma \cdot \nabla c_B^+}{\overline{c}_{B,l}} d_b \; dS_\Sigma, \tag{3.20}$$

where the integration is along the entire bubble surface $S_\Sigma$ with area $|S_\Sigma|$ and

$$\overline{c}_{B,l} = \frac{1}{|S_\Sigma|} \int_{S_\Sigma} c_B^+ \; dS_\Sigma \tag{3.21}$$

is the average liquid-side interfacial concentration. The local Sherwood number $\mathrm{Sh}_{loc}$ at a generic point of the bubble surface is expressed by the integrand of Eq. (3.20), i.e.

$$\mathrm{Sh}_{loc} = \frac{\mathbf{n}_\Sigma \cdot \nabla c_B^+}{\overline{c}_{B,l}} d_b. \tag{3.22}$$

The Sherwood number is generally associated to the intensity of the species transfer processes. Actually, this quantity can be misleading since high values of Sh can be due to large bubble diameters rather than to efficient transfers from the gas to the liquid phase, i.e. higher concentration gradients at the interface.

The mass transfer coefficient

$$\beta_l = \frac{1}{|S_\Sigma|} \int_{S_\Sigma} \frac{\mathbf{n}_\Sigma \cdot D_{B,l} \nabla c_B^+}{\overline{c}_{B,l}} \; dS_\Sigma \tag{3.23}$$

is computed as surface average of the molar flux at the interface scaled with the average liquid-side interfacial concentration. In comparison to the Sherwood number, the absence of the bubble diameter in Eq. (3.23) allows to measure more effectively the efficiency of the unit interfacial area in the transfer process. The local mass transfer coefficient

$$\beta_{l,loc} = \frac{\mathbf{n}_\Sigma \cdot D_{B,l} \nabla c_B^+}{\overline{c}_{B,l}} \tag{3.24}$$

is equal to the integrand of Eq. (3.23).

## 3. Mathematical model for gas-liquid flows with reactive species transfer

For competitive-consecutive mechanisms the reaction selectivity provides information on the amount of the gaseous reactant that has been converted into the product $P$ or the side-product $S$. The corresponding expression is

$$S(t) = \frac{n_P(t) - n_P(t_0)}{n_B(t_0) - n_B(t)}, \tag{3.25}$$

where $n_P$ and $n_B$ denote the total number of moles of product $P$ and reactant $B$ in the system at the starting time of the process $t_0$ and the current time $t$, respectively.

In order to investigate the contribution of different regions of the domain to the global selectivity, an instantaneous and local selectivity can be formulated as follows

$$S_{loc}(t, x) = \frac{R_P}{R_B} = \frac{r_1 - r_2}{r_1 + r_2}. \tag{3.26}$$

Although an integration of the previous expression over the whole duration of the process and the domain occupied by the liquid phase does not provide the global selectivity, Eq. (3.26) suitably estimates the local development of the chemical reactions at a specific time instance.

Two further quantities involved in this study are the Hatta number Ha and the enhancement factor E. Regarding the first reaction of the competitive-consecutive mechanism, the Hatta number is

$$\mathrm{Ha} = \frac{\sqrt{k_1 c_{A,\mathrm{in}} D_{B,l}}}{\beta_l^{\mathrm{phys}}}, \tag{3.27}$$

where $\beta_l^{\mathrm{phys}}$ indicates the mass transfer coefficient in the case of physisorption, i.e. without chemical reactions and $c_{A,\mathrm{in}}$ is the feed concentration of the species $A$. The Hatta number compares the diffusion and the reaction time scales. The enhancement factor measures the increase of the mass transfer due to chemical reactions by means of the ratio $\beta_l/\beta_l^{\mathrm{phys}}$. A local enhancement factor is obtained by replacing $\beta_l$ and $\beta_l^{\mathrm{phys}}$ with the corresponding local coefficients.

# Chapter 4

# Numerical method for gas-liquid flows with reactive species transfer

The numerical method for the simulation of reactive species transfer processes in gas-liquid flows is presented in this chapter. The ALE Interface-Tracking method, as presented by Tuković and Jasak (2012) and implemented in the OpenFOAM-extend project, has been chosen for the numerical treatment of the two-phase hydrodynamic problem. The main details are provided in Section 4.1. Section 4.2 introduces two different methods for the discretisation of the concentration transport equations. The former is based on the special class of functions called Radial Basis Functions (RBF). The latter exploits a standard finite-volume discretisation on a mesh finer than that one used for the hydrodynamic problem. For this reason, it is referred to as *two-mesh* approach.

## 4.1 Interface-Tracking method for gas-liquid flow hydrodynamics

The starting point for the ALE Interface-Tracking method for a single bubble rising in a quiescent liquid is represented by the integral form of the mass and momentum transport equations. The reformulation of Eqs. (3.1) and (3.2) in the bubble reference frame and their successive integration on a moving non-material control volume *V(t)* yields

$$\oint_{S(t)} \mathbf{n} \cdot \mathbf{v}\, dS = 0, \tag{4.1}$$

$$\frac{d}{dt}\int_{V(t)} \rho\mathbf{v}\, dV + \oint_{S(t)} \mathbf{n} \cdot \rho(\mathbf{v}-\mathbf{v}_S)\mathbf{v}\, dS = \oint_{S(t)} \mathbf{n} \cdot \mathbf{S}\, dS - \int_{V(t)} \nabla p\, dV - \int_{V(t)} \rho\mathbf{a}_b\, dV, \tag{4.2}$$

where $\mathbf{n}$ is the outward pointing normal vector on the control volume surface *S(t)*, $p$ denotes here the dynamic pressure obtained by subtracting the hydrostatic contribution from the absolute pressure,

$\mathbf{v}_S$ is the velocity of the surface $S(t)$ and $\mathbf{a}_b$ is the bubble acceleration vector. Following the adoption of the bubble reference frame, the Dirichlet boundary condition for the velocity at infinite distance from the interface changes from $\mathbf{0}$ to $-\mathbf{U}_b(t)$.

In addition to Eqs. (4.1) and (4.2), the following geometric (space) conservation law has to be satisfied

$$\frac{d}{dt}\int_{V(t)} dV + \oint_{S(t)} \mathbf{n}\cdot\mathbf{v}_S\, dS = 0. \tag{4.3}$$

Eq. (4.3) expresses the relationship between the rate of change of the volume *V(t)* and the velocity $\mathbf{v}_S$.

The spatial discretisation of Eqs. (4.1)-(4.3) relies on a second-order accurate cell-centered finite-volume method. Fig. 4.1 introduces the geometrical quantities relating to a generic computational cell $P$ with volume $V_P$. The cell is connected to the neighbouring control volume $N$ through the face $f$ with area vector $\mathbf{S}_f = S_f\mathbf{n}_f$, where $\mathbf{n}_f$ denotes the unit outer normal vector and $S_f$ is the face area.

The second-order implicit *backward* scheme is employed for the time discretisation. In this scheme, the approximation of the temporal derivatives is based on the new ($t^n$) and two previous time instances ($t^o = t^n - \Delta t$ and $t^{oo} = t^o - \Delta t$), with $\Delta t$ representing the integration time-step.

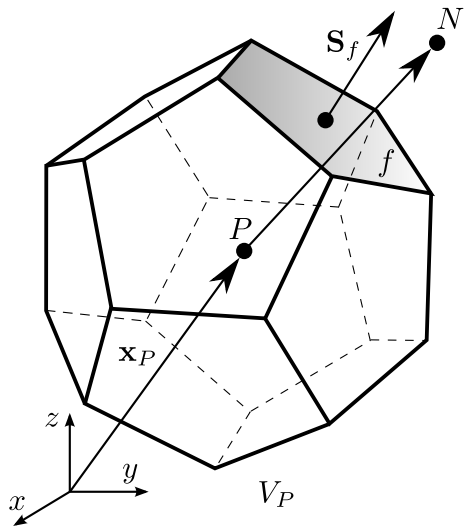


Figure 4.1: Generic polyhedral computational cell.

### 4.1.1 Domain discretisation and simulation setup

The computational domain is split into two regions corresponding to the liquid bulk and the gas bubble, respectively. Both the two regions are decomposed into a set of convex, non-overlapping cells. The interface between the phases is represented by two coincident surfaces. Each surface consists of

a set of boundary faces belonging to the relative mesh.

The region adjacent to the bubble surface and the entire liquid phase is divided in prismatic cells with increasing size moving away from the interface. Generic polyhedrons have been adopted in the inner part of the gas phase since a fully prismatic mesh of a spherical domain is not achievable. The preferential use of prisms is justified by the fact that they allow for a significantly faster solution of the discretised pressure equation, which will be introduced later in this section, in comparison to generic polyhedral cells.

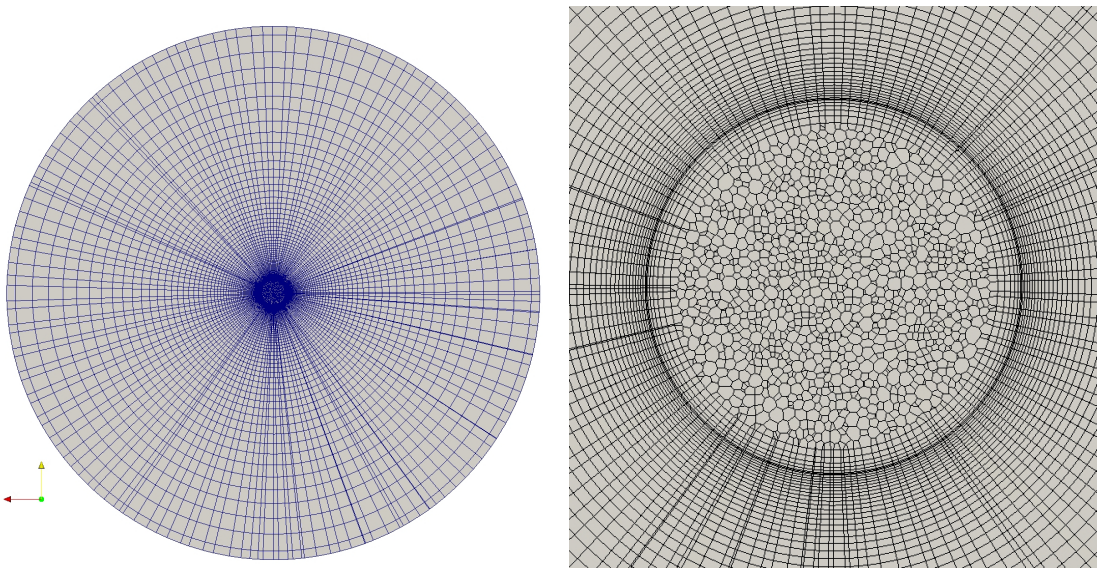

Figure 4.2: Simulation domain and mesh with an enlarged view of the grid close to the interface.

During the simulation the bubble is kept at the centre of the computational domain by means of the moving reference frame technique (see Rusche, 2002, Deising et al., 2016). This approach allows to follow the bubble during its rise through the liquid.

Due to the impossibility to simulate an infinite domain, the liquid phase is delimited by a spherical surface (see Fig. 4.2) on which artificial boundary conditions are applied. The surface radius is chosen equal to $10d_b$ (see Tuković and Jasak, 2012). A mixed Dirichlet/Neumann boundary condition is set for the velocity. The choice for one or the other type depends on whether the current reversed bubble rise velocity $-\mathbf{U}_b$ points inward or outward on a specific boundary face. A velocity equal to $-\mathbf{U}_b$ is imposed in case of inflow. Otherwise, a homogeneous Neumann boundary condition is applied. Regarding the pressure field, the normal gradient is set to zero on the entire surface.

### 4.1.2 Pressure-velocity coupling

At each solution time instance the hydrodynamic problem is solved in both the regions by means of a segregated solution procedure based on the iterative Pressure Implicit with Splitting of Operator

(PISO) algorithm by Issa (1986). The PISO algorithm starts with the solution of the discretised momentum equation which reads for the generic cell $P$

$$\rho_P \frac{3\mathbf{v}_P^n V_P^n - 4\mathbf{v}_P^o V_P^o + \mathbf{v}_P^{oo} V_P^{oo}}{2\Delta t} + \sum_f (\dot{m}_f^{n^*} - \rho_f \dot{V}_f^n)\mathbf{v}_f^n = \sum_f \mu_f \mathbf{n}_f^n \cdot (\nabla \mathbf{v})_f^n S_f^n - (\nabla p)_P^{n^*} V_P^n - \rho_P V_P^n \mathbf{a}_b^o, \tag{4.4}$$

where $\dot{V}_f^n$ is the face volume flux due to the control volume surface motion and $\dot{m}_f^n = \rho_f \mathbf{n}_f^n \cdot \mathbf{v}_f^n S_f^n$ denotes the cell-face mass fluxes. The superscript $n^*$ is used to indicate quantities that have to be treated explicitely employing the current values. For the cell-face mass fluxes $\dot{m}_f^{n^*}$, this is required in order to linearise the convection term of the momentum equation (4.2), while for the pressure term the segregated character of the algorithm does not allow to solve at the same time for the velocity and the pressure fields. Appropriate numerical schemes have to be chosen in order to calculate the face-centre quantities involved in Eq. (4.4), ensuring the boundedness and the second-order accuracy of the discretisation.

The discretised momentum equation (4.4) for the generic cell $P$, previously divived by $V_P^n$, leads to the following linear system

$$a_P \mathbf{v}_P^n + \sum_N a_N \mathbf{v}_N^n = \mathbf{r}_P - (\nabla p)_P^{n^*}, \tag{4.5}$$

where $a_P$ and $a_N$ represent the diagonal and the off-diagonal coefficients, respectively, and $\mathbf{r}_P$ includes all the known terms of Eq. (4.4) except for the pressure. After the solution of the linear system (4.5), the continuity constraint is enforced by means of a pressure equation which results from the combination of the discretised momentum and continuity equations, as outlined in the following steps. The discretised version of the continuity for the generic cell $P$ reads

$$\sum_f \rho_f^n \mathbf{n}_f^n \cdot \mathbf{v}_f^n S_f^n = \sum_f \dot{m}_f^n = 0. \tag{4.6}$$

By analogy with Eq. (4.5), a new cell-centre velocity is formulated as follows

$$\mathbf{v}_P^n = \frac{-\sum_N a_N \mathbf{v}_N^n + \mathbf{r}_P^n}{a_P} - \frac{1}{a_P}(\nabla p)_P^n = \frac{\mathbf{H}_P(\mathbf{v}^n)}{a_P} - \frac{1}{a_P}(\nabla p)_P^n. \tag{4.7}$$

By employing the momentum interpolation method (Ferziger and Perić, 1996), the cell-face velocities in Eq. (4.6) are expressed as

$$\mathbf{v}_f^n = \left(\frac{\mathbf{H}}{a}\right)_f - \left(\frac{1}{a}\right)_f (\nabla p)_f^n, \tag{4.8}$$

where the terms $(\mathbf{H}/a)_f$ and $(1/a)_f$ are obtained by interpolating the velocities (4.7) of the two cell-centres sharing the face $f$. For this purpose, the standard Rhie-Chow interpolation (Rhie and

Chow, 1983) is employed. The substitution of the last expression in Eq. (4.6) results into the pressure equation

$$\sum_f \left(\frac{1}{a}\right)_f \mathbf{n}_f^n \cdot (\nabla p)_f^n S_f^n = \sum_f \mathbf{n}_f^n \cdot \left(\frac{\mathbf{H}}{a}\right)_f S_f^n, \tag{4.9}$$

whose solution provides a new pressure field and, according to Eq. (4.7), a new divergence-free velocity field.

The coupling between the hydrodynamic solutions in both the phases according to the transmission conditions (3.4) and (3.5) is accomplished by boundary conditions imposed on the interfacial surfaces. At the liquid side the pressure value (Dirichlet b.c.) and the velocity normal gradient (Neumann b.c.) are speficified, while at the gas side the pressure gradient (Neumann b.c.) and the velocity value (Dirichlet b.c.) are set. Details about the coupling and the boundary conditions treatment can be found in Tuković and Jasak (2012). The overall two-phase hydrodynamic solution results from an iterative procedure. Each iteration includes the update of the interfacial boundary conditions and, then, the execution of the PISO algorithm in both the domains. The loop is performed until both the transmission conditions are fulfilled within a prescribed tolerance.

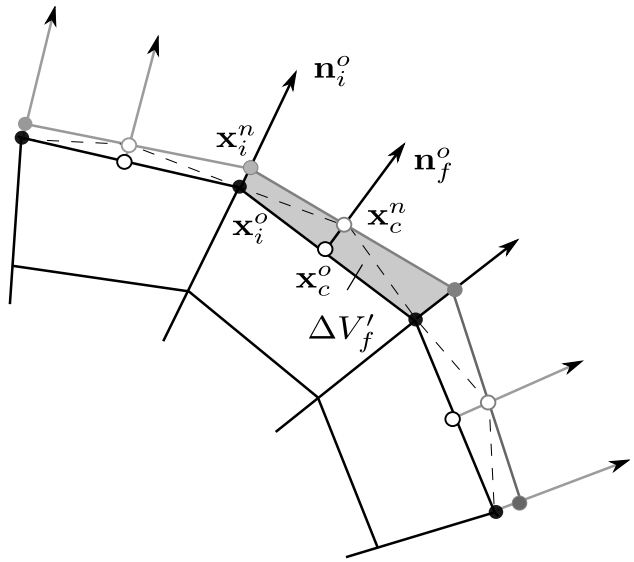


Figure 4.3: Interface movement.

### 4.1.3 Tracking of the interface and mesh motion

The assumption that the transfer of the chemical components has no influence on the two-phase hydrodynamics results in the condition of zero net mass flux across the interfacial faces

$$\dot{m}_f^n - \rho_f \dot{V}_f^n = 0. \tag{4.10}$$

In general, the solution at the end of each hydrodynamic loop iteration does not fulfill Eq. (4.10). Thus, the interface points have to be moved in order to produce the following corrective cell-face volume fluxes

$$\dot{V}_f' = \frac{\dot{m}_f^n}{\rho_f} - \dot{V}_f^n \tag{4.11}$$

and, at the same time, satisfy the discrete form of Eq. (4.3). Demirdžić and Perić (1988) have highlighted that not satisfying this equation introduces errors in the form of artificial mass sources. The displacement is performed in two separate steps. First, additional points located at the face centres, called *control points*, are displaced along the face normal direction $\mathbf{n}_f^o$. Then, a least squares interpolation method is used in order to determine the new positions of the interface points $\mathbf{x}_i^n$. Details about the tracking algorithm can be found in Tuković and Jasak (2012).

The motion of the remaining part of the mesh is accomplished by solution of the following Laplace equation

$$\nabla \cdot (\Gamma \nabla \mathbf{u}) = 0, \tag{4.12}$$

where $\mathbf{u}$ denotes the displacement of the generic mesh vertex. The interface movement previously computed serves as boundary condition for Eq. (4.12). The diffusion coefficient $\Gamma$ is chosen to be inversely proportional to the square of the distance from the interface in order to have a more rigid mesh close to the moving boundary and, thus, preserve the grid quality and resolution.

## 4.2 Species transfer numerical methods

The very thin concentration boundary layers relating to high Péclet numbers require a very fine computational resolution in the vicinity of the interface. The situation becomes even more severe in the presence of chemical reactions which further reduce the boundary layers thickness. This undue resolution requirement makes all the current numerical techniques unable to resolve industrially relevant reactive species transfer processes in reasonable computational times. This forces to develop novel numerical methods capable to overcome these difficulties.

In this work two different numerical methods for the discretisation of the concentration convection-diffusion equations have been developed. This section introduces the details of both the techniques. Their performances in terms of accuracy, stability and efficiency have been assessed by validation cases.

Since the chemical reaction terms do not involve any derivative, their numerical treatment is independent from the method adopted for the approximation of the other terms in Eq. (3.13). For a generic discretisation element $P$, i.e. point, cell, etc., the reaction source term of the species $k$ is computed as follows

$$R_{k,P} = \sum_{i=1,2} \nu_{k,i} r_{i,P}^o. \tag{4.13}$$

The superscript "o" indicates that the non-linear reaction rates $r^o_{i,P},\ i$=1, 2 are calculated explicitly using the concentration values at the old time instance. In the case of stiff problems, i.e. when the chemical time scales are much smaller than the hydrodynamic ones, Eq. (4.13) could provide inaccurate estimations of the chemical terms. A better evaluation is obtained by employing a sub-time stepping procedure which considers an auxiliary problem derived from Eq. (3.13) neglecting the species advection and diffusion. For each element, the resulting non-linear system of ODEs

$$\frac{dc_k}{dt} = \sum_{i=1,2} \nu_{k,i} r_i = R_k, \quad k \in \{A, B, P, S\} \tag{4.14}$$

is solved from $t^o$ to $t^n$ with a time-step smaller than $\Delta t$ in Eq. (4.4) by means of the semi-implicit Bulirsch-Stoer method (Bader and Deuflhard, 1983). Differently from the original method (Bulirsch and Stoer, 1966), this variant has proved to be particularly suitable for stiff systems. By the solution of Eq. (4.14) the reaction source term $R_{k,P}$ of the species $k$ is determined as follows

$$R_{k,P} = \frac{c^{\text{aux}}_{k,P} - c^o_{k,P}}{\Delta t}, \tag{4.15}$$

where the superscript "aux" refers to the final concentrations of the auxiliary problem.

The rest of this section has been focused on the discretisation of the species transport equations disregarding the contributions coming from the chemical reactions.

### 4.2.1 Radial Basis Function-based numerical method

The Radial Basis Functions (RBFs) were developed as a tool for interpolation of multidimensional scattered data. Starting from the pioneering work of Kansa (1990), the Radial Basis Functions have been also used to formulate novel numerical methods for the solution of partial differential equations (PDEs). These methods have proved to be helpful for problems with complex geometries for which it is preferable to use sets of scattered nodes rather than meshes. The argumentation of this section starts with the foundation of every finite-difference technique: the interpolation. The issues of the multivariate polynomial interpolation and the alternative based on the RBFs are introduced in detail in the sections 4.2.1.1 and 4.2.1.2. Section 4.2.1.3 presents the main RBF-based numerical techniques reported in the literature. The Explicit Boundary Radial Basis Function finite-difference method developed in this work is described in Section 4.2.1.4. The test cases used to validate this method are shown in Section 4.2.1.5. Finally, comments about the performances of the method are given in Section 4.2.1.6.

#### 4.2.1.1 Polynomial interpolation

The interpolation problem can be formalised as follows: given $N$ distinct points $\mathbf{x}_1, \mathbf{x}_2, ...., \mathbf{x}_N \in \mathbf{R}^d$ and $N$ values $f_1, f_2, ..., f_N$, a function $f$ is called *interpolant* if and only if

$$f(\mathbf{x}_i) = f_i, \quad \forall\ i \in \{1, 2, ..., N\}. \tag{4.16}$$

Since only physical problems are considered here, the maximum number of spatial dimensions $d$ is 3.

Starting from the easiest case of $d$=1, the most straightforward approach to determine $f$ relies on the usage of polynomials. The interpolant can be written as a polynomial of degree $N-1$

$$f(x) = \sum_{i=0}^{N-1} a_i x^i = a_0 + a_1 x + a_2 x^2 + .....a_{N-1} x^{N-1}. \tag{4.17}$$

The coefficients of the interpolant can be determined by imposing the constraints (4.16). This results in the following linear system of equations

$$\begin{bmatrix} 1 & x_1 & x_1^2 & \cdots & x_1^{N-1} \\ 1 & x_2 & x_2^2 & \cdots & x_2^{N-1} \\ \vdots & \vdots & \vdots & \ddots & \vdots \\ 1 & x_N^1 & x_N^2 & \cdots & x_N^{N-1} \end{bmatrix} \begin{bmatrix} a_0 \\ a_1 \\ \cdots \\ a_{N-1} \end{bmatrix} = \begin{bmatrix} f_1 \\ f_2 \\ \cdots \\ f_N \end{bmatrix} \tag{4.18}$$

whose solution provides the coefficients $a_i$, $\forall\ i \in \{0, 1, .., N-1\}$.

The case $d > 1$ is now considered. The space of all $d$-variate polynomials is denoted by $\Pi^d$. $\Pi_n^d$ is the subspace of $\Pi^d$ containing all the polynomials of degree at most equal to $n$. The members of $\Pi_n^d$ have the following form

$$f(\mathbf{x}) = \sum_{|\boldsymbol{\alpha}_j| \leq n} c_j \mathbf{x}^{\boldsymbol{\alpha}_j}, \tag{4.19}$$

with $\boldsymbol{\alpha}_j \in \mathbf{N}_0^d$, $|\boldsymbol{\alpha}_j| = \sum_{k=1}^{d} \alpha_{j,k}$, $\mathbf{x}^{\boldsymbol{\alpha}_j} = x_1^{\alpha_{j,1}} x_2^{\alpha_{j,2}} \cdots x_d^{\alpha_{j,d}}$. The dimension of $\Pi_n^d$ is $\binom{n+d}{d}$.

**Definition 4.1**. Consider the $N$-dimensional polynomial subspace $\Pi_n^d$ with $N = \binom{n+d}{d}$. The interpolation problem on a set of $N$ distinct points $\mathbf{x}_1, \mathbf{x}_2, ..., \mathbf{x}_N \in \mathbf{R}^d$ is called *correct* (*poised* or *unisolvent*) in $\Pi_n^d$ if for any set of data $f_1, f_2, ..., f_N$ there exists a unique polynomial $f \in \Pi_n^d$ satisfying Eqs. (4.16).

**Theorem 4.1**. The interpolation problem on a set of $N$ distinct points $\mathbf{x}_1, \mathbf{x}_2, ..., \mathbf{x}_N \in \mathbf{R}^d$ is *correct* in $\Pi_n^d$ if the Vandermonde matrix

$$\begin{bmatrix} 1 & 1 & \cdots & 1 \\ \mathbf{x}_1^{\boldsymbol{\alpha}_1} & \mathbf{x}_2^{\boldsymbol{\alpha}_1} & \cdots & \mathbf{x}_N^{\boldsymbol{\alpha}_1} \\ \mathbf{x}_1^{\boldsymbol{\alpha}_2} & \mathbf{x}_2^{\boldsymbol{\alpha}_2} & \cdots & \mathbf{x}_N^{\boldsymbol{\alpha}_2} \\ \vdots & \vdots & \ddots & \vdots \\ \mathbf{x}_1^{\boldsymbol{\alpha}_{N-1}} & \mathbf{x}_2^{\boldsymbol{\alpha}_{N-1}} & \cdots & \mathbf{x}_N^{\boldsymbol{\alpha}_{N-1}} \end{bmatrix} \tag{4.20}$$

is non singular.

It can be deduced from Theorem 4.1 that a well-posed multivariate interpolation problem requires that the determinant of the Vandermonde matrix is always different from zero independently from the

considered set of interpolation points. Theorem 4.2 shows that this condition does not occur. First, another definition is introduced.

**Definition 4.2**. An $N$-dimensional linear subspace $V$ of all continuous functions $C(\mathbf{R}^d)$ with basis $\{b_1, b_2, ..., b_N\}$ is called a *Haar* space of order $N$ if

$$det(\mathbf{A}) \neq 0 \tag{4.21}$$

for any set of points $\mathbf{x}_1, \mathbf{x}_2, .., \mathbf{x}_N \in \mathbf{R}^d$. $\mathbf{A}$ is the matrix with entries $\mathrm{A}_{i,j}$=$b_i(\mathbf{x}_j)$.

**Theorem 4.2** (Haar-Mairhuber-Curtis). In the case $d \geq 2$, there exist no Haar spaces except for the trivial case $N$=1.

As consequence of Theorem 4.2, the multivariate polynomial interpolation is not a well-posed problem, i.e. there is no guarantee about the existence and uniqueness of the interpolant. A pair of examples can highlight this fact. Considering three collinear points in the Euclidean plane, it exists a polynomial interpolant only if the values $f_i$, $i$=1, 2, 3 are in accordance with a linear variation along the line connecting the three points. The interpolation problem has no solution in all the other cases. In the second example 6 points on the unit circle $x^2 + y^2 - 1$=0 are considered. The approximating function $f$ belongs to $\Pi_2^2$. If the quantity $x^2 + y^2 - 1$ is added to the interpolant, it is possible to formulate another interpolating polynomial for the same set of data $f_i$, $i$=1, 2, .., 6 due to the non-uniqueness of this interpolation problem.

Actually, Theorem 4.2 is more general. It tells that a well-posed multivariate interpolation on scattered points cannot be obtained by fixing in advance any set of basis functions. On the contrary, the basis has to depend on the interpolation points.

#### 4.2.1.2 Radial Basis Function interpolation

A powerful and flexible solution to the ill-posedness of the polynomial interpolation in the case of $d > 1$ is obtained by means of the so-called Radial Basis Functions. The members of this class of functions share the fundamental requirement to be symmetric with respect to a reference point $\overline{\mathbf{x}}$, i.e. a RBF $\phi(\mathbf{x})$=$\phi(|\mathbf{x} - \overline{\mathbf{x}}|)$) depends only on the distance of $\mathbf{x}$ from $\overline{\mathbf{x}}$. This feature motivates the usage of the word *radial* in the class name. However, a more precise definition of the RBFs highlighting the other characteristics of these functions will be provided later in this subsection.

Coming back to the interpolation problem, a generic RBF $\phi$ can be used to formulate the following expression for the interpolant $f$

$$f(\mathbf{x}) = \sum_{j=1}^{N} c_j \phi(|\mathbf{x} - \mathbf{x}_j|) + \sum_{k=1}^{M} b_k p_k(\mathbf{x}), \quad \text{with } N \geq M. \tag{4.22}$$

The set $\{p_1, p_2, ..., p_M\}$ is a basis for the space of the $d$-variate polynomials of degree at most $n$, where

$M$ is equal to $\binom{n+d}{d}$. The coefficients $c_j$, $j$=1, 2, .., $N$ and $b_k$, $k$=1, 2, .., $M$ are determined by imposing the conditions

$$\sum_{j=1}^{N} c_j p_k(\mathbf{x}_j) = 0 \qquad k = 1, ...., M \tag{4.23}$$

and the constraints (4.16) on the interpolant (4.22). This results in the linear stystem of equations

$$\begin{bmatrix} \mathbf{\Phi} & \mathbf{P}^{\mathrm{T}} \\ \mathbf{P} & \mathbf{0} \end{bmatrix} \begin{bmatrix} \mathbf{c} \\ \mathbf{b} \end{bmatrix} = \begin{bmatrix} \mathbf{f} \\ \mathbf{0} \end{bmatrix}, \tag{4.24}$$

where the entries of $\mathbf{\Phi}$ and $\mathbf{P}$ are $\Phi_{i,j}$=$\phi(|\mathbf{x}_i - \mathbf{x}_j|)$, $i, j$=1, 2, .., $N$ and $\mathrm{P}_{k,j}$=$p_k(\mathbf{x}_j)$, $k$=1, 2, .., $M$, $j$=1, 2, .., $N$, respectively. In order to understand the meaning of the supplementary conditions (4.23), the concept of *Conditionally Positive Definite* (CPD) function has to be introduced.

**Conditionally Positive Definite Radial Basis Functions**

An interpolation problem with polynomial reproduction up to the order $n$ is considered. If the data $f_1, f_2, .., f_N$ are obtained by sampling a multivariate polynomial $p$ of degree at most $n$ at the points $\mathbf{x}_1, \mathbf{x}_2, .., \mathbf{x}_N$, the polynomial reproduction requirement implies that the interpolant $f$ is equal to $p$ in the entire space $\mathbf{R}^d$ and not only at the interpolation points.

An interpolant of the following form is taken into account

$$f(\mathbf{x}) = \sum_{j=1}^{N} c_j \phi(\mathbf{x} - \mathbf{x}_j) + \sum_{|\boldsymbol{\alpha}_k| \leq n} b_k \mathbf{x}^{\boldsymbol{\alpha}_k}, \tag{4.25}$$

with $\phi : \mathbf{R}^d \mapsto \mathbf{R}$. Enforcing the conditions $f(\mathbf{x}_i) = f_i$, $i = 1, 2, ..., N$, yields the set of equations

$$\sum_{j=1}^{N} c_j \phi(\mathbf{x}_i - \mathbf{x}_j) + \sum_{|\boldsymbol{\alpha}_k| \leq n} b_k \mathbf{x}_i^{\boldsymbol{\alpha}_k} = f_i \qquad i = 1, ..., N, \tag{4.26}$$

which can be cast in the matrix notation

$$\mathbf{\Phi c} + \mathbf{P}^{\mathrm{T}} \mathbf{b} = \mathbf{f}. \tag{4.27}$$

The number of relations in (4.27) is $N$, while the interpolation coefficients are $N + M$ with $M$=$\binom{n+d}{d}$. Therefore, $M$ further constraints are needed in order to obtain a determined problem. These remaining constraints come from the polynomial reproduction requirement.

The data vector $\mathbf{f}$ is assumed to contain the values of a generic multivariate polynomial $p$ of degree at most $n$ at the interpolation points $\mathbf{x}_1, \mathbf{x}_2, .., \mathbf{x}_N$,

$$\mathbf{f} = \mathbf{f}_{poly} = \mathbf{P}^{\mathrm{T}} \tilde{\mathbf{b}}. \tag{4.28}$$

Then, the polynomial reproduction requirement requires that

$$\mathbf{P}^{\mathrm{T}}\tilde{\mathbf{b}} = \mathbf{\Phi c} + \mathbf{P}^{\mathrm{T}}\mathbf{b} \tag{4.29}$$

has $\mathbf{c}$=$\mathbf{0}$ and, accordingly, $\mathbf{b}$=$\tilde{\mathbf{b}}$ as its unique solution. This can be achieved by choosing $\phi$ from the class of the Conditionally Positive Definite functions. The following definition characterizes the members of this class.

**Definition 4.3**. Let $\phi : \mathbf{R}^d \rightarrow \mathbf{C}$ be continuous. The function $\phi$ is CPD of order $n+1$ if for every set $\{\mathbf{x}_1, \mathbf{x}_2, .., \mathbf{x}_N\}$ of distinct points in $\mathbf{R}^d$ and for every set of complex scalars $c_1, c_2, ..., c_N$ satisfying

$$\sum_{j=1}^{N} c_j p(\mathbf{x}_j) = 0 \quad \forall\, p(\mathbf{x}) \in \Pi_n^d, \text{ or equivalently } \quad \mathbf{Pc} = \mathbf{0}, \tag{4.30}$$

the following relation

$$\mathbf{c}^{\mathrm{H}}\mathbf{\Phi c} = \sum_{i,j=1}^{N} \overline{c}_i c_j \phi(\mathbf{x}_i - \mathbf{x}_j) \geq 0 \tag{4.31}$$

is verified, where the superscript "H" denotes the adjoint operator. If, additionally, $\mathbf{c}^{\mathrm{H}}\mathbf{\Phi c}$=$\mathbf{0}$ occurs only when $\mathbf{c}$=$\mathbf{0}$, then $\phi$ is *strictly* CPD of order $n+1$.

It is straightforward to prove that the interpolant (4.25) satisfies the polynomial reproduction requirement up to the order $n$ provided that $\phi$ is strictly CPD of order $n+1$ and $\mathbf{Pc}$=$\mathbf{0}$. Since $\mathbf{P}$ is real, it is possible to rewrite Eq. (4.30) as

$$\mathbf{c}^{\mathrm{H}}\mathbf{P}^{\mathrm{T}} = 0, \tag{4.32}$$

where $\mathbf{P}^{\mathrm{H}}$=$\mathbf{P}^{\mathrm{T}}$ has been used. Multiplying Eq. (4.29) with $\mathbf{c}^{\mathrm{H}}$ and employing Eq. (4.32) leads to

$$\mathbf{c}^{\mathrm{H}}\mathbf{P}^{\mathrm{T}}\tilde{\mathbf{b}} = \mathbf{c}^{\mathrm{H}}\mathbf{\Phi c} + \mathbf{c}^{\mathrm{H}}\mathbf{P}^{\mathrm{T}}\mathbf{b} \implies \mathbf{0} = \mathbf{c}^{\mathrm{H}}\mathbf{\Phi c} + \mathbf{0} \implies \mathbf{c}^{\mathrm{H}}\mathbf{\Phi c} = \mathbf{0}. \tag{4.33}$$

Following the assumption that $\phi$ is strictly CPD of order $n+1$, the unique solution of (4.33) is for $\mathbf{c}$=$\mathbf{0}$, as required by the polynomial reproduction condition.

**Theorem 4.3** (see Micchelli, 1986). Let $\phi$ be strictly CPD of order $n+1$. Then, the function $f$ in (4.25) is the unique solution of the interpolation problem with polynomial reproduction up to the order $n$ provided that the rank of $\mathbf{P}$ is $M$ and $\mathbf{c}$ fulfills $\mathbf{Pc} = \mathbf{0}$.

The requirement of maximum rank for the matrix $\mathbf{P}$ imposes some limitations on the positions of the interpolation points. However, since the maximum degree $n$ of the additional polynomial part is usually small, the conditions on these locations are significantly less restrictive in comparison to those ones of a "pure" multivariate polynomial interpolation on the same set of points $\{\mathbf{x}_1$,$\mathbf{x}_2$,..,$\mathbf{x}_N\}$.

The search for strictly CPD functions of order $n+1$ is usually restricted to the class of the *radial* functions $\phi(\mathbf{x})= \phi(|\mathbf{x}|)=\phi(r)$ which depends only on the euclidean distance from the origin, i.e. the radial coordinate. Furthermore, it is preferable to seek radial functions that are strictly CPD of order $n+1$ for all $d \geq 1$. First results regarding the determination of the conditions under which a radial function is CPD for all $d \geq 1$ were obtained by Schoenberg (1938). Another definition is needed in order to present Schoenberg's results.

**Definition 4.4**. A function $\psi$: $(0,+\infty) \rightarrow \mathbf{R}$ is said to be *completely monotonic* on $(0,+\infty)$ ($\psi \in CM(0,+\infty)$) if $\psi \in C^{\infty}(0,+\infty)$ and if its derivatives satisfy

$$(-1)^k \psi^{(k)}(r) \geq 0 \quad \forall\, r \in (0,+\infty) \quad \forall\, k \in \mathbf{N}_0. \tag{4.34}$$

If, additionally, $\psi$ is continuous at $r$=0, then $\psi$ is $CM[0,+\infty)$.

**Theorem 4.4** (Schoenberg). A function $\psi$ is $CM[0,+\infty)$ if and only if the radial function $\phi(r) = \psi(|\mathbf{x}|^2)$ is CPD of order 0, i.e. positive definite, on $\mathbf{R}^d$ for all $d \geq 1$.

As a consequence of Schoenberg's theorem it follows that the only positive definite radial function for all $d \geq 1$ is the Gaussian $e^{-\epsilon r^2}$ with the parameter $\epsilon > 0$. Considering a function $\psi \in C[0,+\infty) \cap C^{\infty}(0,+\infty)$, Micchelli (1986) showed that the radial function $\phi(r)=\psi(|\mathbf{x}|^2)$ is CPD of order 1 on $\mathbf{R}^d$ for all $d \geq 1$ if and only if $-\frac{d}{dr}\psi(r)$ is $CM(0,+\infty)$. A classical example of $1^{\text{st}}$ order CPD function is represented by the Hardy's multiquadric $\sqrt{1+r^2}$.

The results from Schoenberg and Micchelli were generalized by Guo et al. (1993) and Sun (1995). The following theorem reports their generalization.

**Theorem 4.5** (Guo et al., Sun). Let $\psi \in C[0,+\infty) \cap C^{\infty}(0,+\infty)$. The radial function $\phi(r)=\psi(|\mathbf{x}|^2)$ is CPD of order $m$ on $\mathbf{R}^d$ for all $d \geq 1$ if and only if $(-1)^m \frac{d^m}{dr^m}\psi(r)$ is $CM(0,+\infty)$.

The above results provide the conditions under which a radial function is CPD for all $d \geq 1$. Theorem 4.6 defines the requirements in order to get strictly CPD radial functions.

**Theorem 4.6** (Fasshauer, 2005). If $\psi$ verifies the conditions of Theorem 4.5 and, additionally, is not a polynomial of degree at most $m$, then the radial function $\phi(r)=\psi(|\mathbf{x}|^2)$ is strictly CPD of order $m$ on $\mathbf{R}^d$ for all $d \geq 1$.

A radial function that is strictly CPD of order $m$ for all $d \geq 1$ is called radial basis function of order $m$. In general, the RBFs are subdiveded into two main categories: the piecewise smooth and the infinitely smooth. The most known member of the former group is the Duchon's thin plate spline $r^2 \ln r$. The Gaussian and Hardy's multiquadric represent classical examples of the latter group. The function $\phi$ of the interpolant (4.22) can be chosen among the members of both the categories.

The infinitely smooth RBFs often exhibit a shape parameter $\epsilon$ which allows to vary their shapes from sharply peaked to nearly flat. Large values of $\epsilon$ yield a well-conditioned linear system for the determination of the interpolation coefficients. However, if the data $f_1, f_2, .., f_N$ are obtained by sampling some given function $f^*$, the resulting interpolant unsatisfactorily approximates $f^*(\mathbf{x})$ at a generic $\mathbf{x}$ different from the interpolation points $\mathbf{x}_1, \mathbf{x}_2, ..., \mathbf{x}_N$. Opposite situation is encountered when $\epsilon$ is small, as shown by Fornberg and Wright (2004). Unfortunately, the system matrix approaches very rapidly the singularity condition as $\epsilon$ decreases leading to an ill-conditioned problem. This implies a loss of computational accuracy due to the significant amount of numerical cancellation. Fornberg and Wright proposed an alternative method which bypasses the solution of the linear system. Although they showed accurate computations even for very small $\epsilon$ values, this technique is not straightforwardly applicable when the RBFs are employed for the numerical solution of PDEs. Therefore, the adoption of intermediate values of the free-parameter represents the best compromise between the two aspects.

Some RBF-based numerical methods rely on a more complex interpolation problem. If, in addition to the conditions (4.16), it is enforced that the values of a certain linear differential operator $L$ applied to the interpolant $f$ at some points $\mathbf{x}_{N+1}, \mathbf{x}_{N+2}, ...\mathbf{x}_{N+NL}$ are $g_1, g_2, .., g_{NL}$, then the interpolation is called *Hermitian*. The RBF interpolant for a Hermitian problem is

$$f(\mathbf{x}) = \sum_{j=1}^{N} c_j \phi(|\mathbf{x} - \mathbf{x}_j|) + \sum_{j=1}^{NL} c_j^L L_2 \phi(|\mathbf{x} - \mathbf{x}_{N+j}|) + \sum_{k=1}^{M} b_k p_k(\mathbf{x}), \tag{4.35}$$

where the subscript "2" indicates that the linear differential operator is applied with respect to the second variable of the basis function argument. The condition (4.23) reads now

$$\sum_{j=1}^{N} c_j p_k(\mathbf{x}_j) + \sum_{j=1}^{NL} c_j^L L p_k(\mathbf{x}_{N+j}) = 0 \qquad k = 1, ...., M. \tag{4.36}$$

The linear system for the coefficients $c_j$, $j$=1, 2, .., $N$, $c_j^L$, $j$=1, 2, .., $NL$ and $b_k$, $k$=1, 2, .., $M$ is

$$\begin{bmatrix} \mathbf{\Phi} & L_2[\mathbf{\Phi}] & \mathbf{P}^{\mathrm{T}} \\ L_1[\mathbf{\Phi}] & L_1 L_2[\mathbf{\Phi}] & L[\mathbf{P}^{\mathrm{T}}] \\ \mathbf{P} & L[\mathbf{P}] & \mathbf{0} \end{bmatrix} \begin{bmatrix} \mathbf{c} \\ \mathbf{c}^L \\ \mathbf{b} \end{bmatrix} = \begin{bmatrix} \mathbf{f} \\ \mathbf{g} \\ \mathbf{0} \end{bmatrix}, \tag{4.37}$$

where the different blocks of the matrix are

$$L_2[\mathbf{\Phi}] = L_2[\Phi_{i,j}] = L_2 \phi(|\mathbf{x}_i - \mathbf{x}_{N+j}|), \quad i = 1, 2, .., N \quad \text{and} \quad j = 1, 2, .., NL, \tag{4.38}$$

$$L_1[\mathbf{\Phi}] = L_1[\Phi_{i,j}] = L_1 \phi(|\mathbf{x}_{N+i} - \mathbf{x}_j|), \quad i = 1, 2, .., NL \quad \text{and} \quad j = 1, 2, .., N, \tag{4.39}$$

$$L_1 L_2[\mathbf{\Phi}] = L_1 L_2[\Phi_{i,j}] = L_1 L_2 \phi(|\mathbf{x}_{N+i} - \mathbf{x}_{N+j}|), \quad i = 1, 2, .., NL \quad \text{and} \quad j = 1, 2, .., NL, \tag{4.40}$$

$$L[\mathbf{P}] = L[\mathrm{P}_{k,j}] = L p_k(\mathbf{x}_{N+j}), \quad k = 1, 2, .., M \quad \text{and} \quad j = 1, 2, .., NL. \tag{4.41}$$

The differential operator $L_1$ acts on the first variable of $\phi$. Regarding the blocks $L[\mathbf{P}]$ and $L[\mathbf{P}^{\mathrm{T}}]$

related to the polynomial part of the interpolant, it is not needed to specify any subscript for $L$ since these terms depend only on $\mathbf{x}$. The system matrix is symmetric and it has been shown by Sun (1994) to be non-singular provided that $\phi$ is a radial basis function of order $n+1$.

#### 4.2.1.3 RBF-based numerical methods

The work of Kansa (1990) represents the first attempt to use RBFs for solving PDEs. The boundary value problem

$$L[c(\mathbf{x})] = S(\mathbf{x}) \tag{4.42}$$

$$B[c(\mathbf{x})] = G(\mathbf{x}) \tag{4.43}$$

is considered, with the linear differential operators $L$ and $B$ acting on the generic open set $\Omega \subseteq \mathbf{R}^d$ and its boundaries $\partial\Omega$, respectively. The solution $c(\mathbf{x})$ in the Kansa's method is written as follows

$$c(\mathbf{x}) = \sum_{j=1}^{N} \lambda_j \phi(|\mathbf{x} - \mathbf{x}_j|) + \sum_{j=1}^{M} \lambda_{N+j} p_j(\mathbf{x}), \tag{4.44}$$

where $\phi$ is a RBF of order $n+1$ and the points $\mathbf{x}_1, \mathbf{x}_2, .., \mathbf{x}_N$ are placed both in the interior part and on the contour of the domain. As explained in the previous subsection, the presence of polynomial terms up to the $n^{\text{th}}$ degree depends on the order of $\phi$.

Enforcing the conditions (4.42) and (4.43) at the internal and boundary points, respectively, and the supplementary constraints (4.23) yields the system of equations

$$\begin{bmatrix} L[\mathbf{\Phi}] & L[\mathbf{P}^{\mathrm{T}}] \\ B[\mathbf{\Phi}] & B[\mathbf{P}^{\mathrm{T}}] \\ \mathbf{P} & \mathbf{0} \end{bmatrix} \begin{bmatrix} \\ \boldsymbol{\lambda} \\ \\ \end{bmatrix} = \begin{bmatrix} \mathbf{S} \\ \mathbf{G} \\ \mathbf{0} \end{bmatrix}. \tag{4.45}$$

Although this collocation method has been successfully employed for solving parabolic, hyperbolic and elliptic PDEs, the resulting non-symmetric matrix in (4.45) is not guaranteed to be invertible.

In order to circumvent this issue, Fasshauer (1997) modified the Kansa's method by inserting the operators $L$ and $B$ into the solution expression as follows

$$c(\mathbf{x}) = \sum_{j=1}^{NB} \lambda_j L_2 \phi(|\mathbf{x} - \mathbf{x}_j|) + \sum_{j=NB+1}^{N} \lambda_j B_2 \phi(|\mathbf{x} - \mathbf{x}_j|) + \sum_{j=1}^{M} \lambda_{N+j} p_j(\mathbf{x}). \tag{4.46}$$

In this case, the collocation process leads to the linear system

$$\begin{bmatrix} L_1 L_2[\mathbf{\Phi}] & L_1 B_2[\mathbf{\Phi}] & B[\mathbf{P}^{\mathrm{T}}] \\ B_1 L_2[\mathbf{\Phi}] & B_1 B_2[\mathbf{\Phi}] & L[\mathbf{P}^{\mathrm{T}}] \\ B[\mathbf{P}] & L[\mathbf{P}] & \mathbf{0} \end{bmatrix} \begin{bmatrix} \\ \boldsymbol{\lambda} \\ \\ \end{bmatrix} = \begin{bmatrix} \mathbf{S} \\ \mathbf{G} \\ \mathbf{0} \end{bmatrix}. \tag{4.47}$$

The matrix in (4.47) is symmetric and non-singular (see Wu, 1998).

Despite the very high convergence rates, the computational cost of these global methods grows rapidly as the number of points $N$ increases due to the ill-conditioning of the corresponding fully-populated matrices. Some techniques as RBF-specific preconditioners (see Brown et al., 2005), adaptive selection of the collocation points (see Ling et al., 2006) and multiscale collocation (see Gia et al., 2012) have been developed in order to alleviate this problem.

A different strategy relies on the employment of compactly-supported RBFs (see Wendland, 1995) which are non-zero only in a limited spherical region around the origin. This allows to obtain a sparse global collocation matrix that can be solved more efficiently than the dense matrices arising from the use of RBFs with non-compact support. However, this reduces considerably the set of possible RBFs. Furthermore, each of these compactly-supported functions is not properly a RBF since it is strictly positive definite only up to a fixed maximal value of $d$. Thus, problems with different dimensionality might not be treated with the same basis function.

A *local* approach represents the most common alternative for circumventing the ill-conditioning issue typical of the global methods but maintaining at the same time the possibility to adopt an arbitrary RBF. A local problem for each point is formed considering the closest neighbours. This produces $N$ small overlapping local systems on which a RBF interpolation is built up. Applying the linear differential operator $L$ to the interpolant relating to each point, a finite-difference discretisation, which can be seen as a generalization of the standard finite-difference methods based on polynomials, is formulated (see Wright and Fornberg, 2006). An additional step required by this approach is the construction of the neighbour lists. An efficient algorithm, which performs efficiently even in the case of point distributions with spatially-varying resolution, is described in Awile et al. (2012).

In the local RBF Hermitian method of Stevens et al. (2009), the interpolant

$$\begin{aligned} c^{(k)}(\mathbf{x}) = \sum_{j=1}^{NS} \lambda_j^{(k)} \phi(|\mathbf{x}-\mathbf{x}_j^{(k)}|) + \sum_{j=NS+1}^{NS+NB} \lambda_j^{(k)} B_2 \phi(|\mathbf{x}-\mathbf{x}_j^{(k)}|) + \\ \sum_{j=NS+NB+1}^{NS+NB+NL} \lambda_j^{(k)} L_2 \phi(|\mathbf{x}-\mathbf{x}_j^{(k)}|) + \sum_{j=1}^{M} \lambda_{N+j}^{(k)} p_j(\mathbf{x}) \end{aligned} \tag{4.48}$$

is considered for each local system $k$. $NS$ is the number of solution centres, i.e. the points at which the numerical solution of the boundary value problem (4.42) and (4.43) is obtained. $NL$ denotes the number of PDE centres at which the differential equation (4.42) is enforced. If the locations of the solution and PDE centres coincide, the stencil is called *collocated*, otherwise *staggered*. Finally, $NB$ represents the number of boundary nodes within the local system $k$. $N$ is given by the sum $NS$+$NB$+$NL$.

Enforcing the constraints

$$\begin{aligned} &c^{(k)}(\mathbf{x}_i^{(k)}) = c_i^{(k)} && i = 1, 2, .., NS, \\ &B[c^{(k)}(\mathbf{x}_i^{(k)})] = G(\mathbf{x}_i^{(k)}) && i = NS+1, .., NS+NB, \\ &L[c^{(k)}(\mathbf{x}_i^{(k)})] = S(\mathbf{x}_i^{(k)}) && i = NS+NB+1, .., NS+NB+NL \end{aligned} \tag{4.49}$$

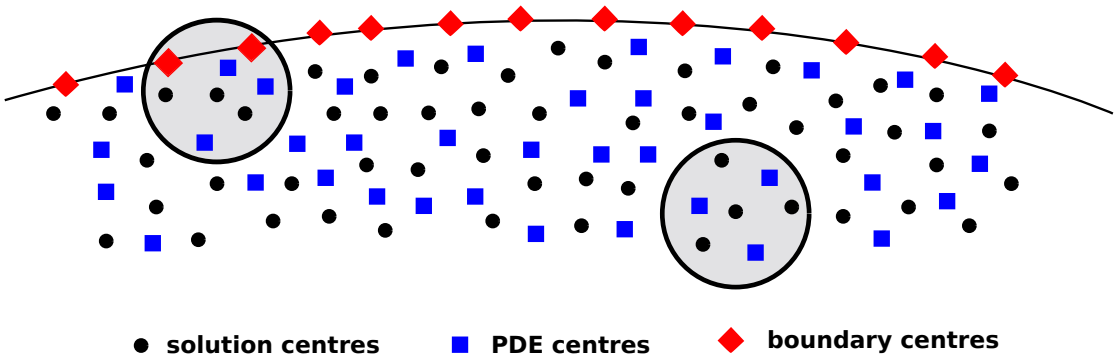


Figure 4.4: Schematic representation of two staggered local systems.

and the supplementary conditions

$$\sum_{j=1}^{NS} \lambda_j^{(k)} p_i(\mathbf{x}_j^{(k)}) + \sum_{j=NS+1}^{NS+NB} \lambda_j^{(k)} Bp_i(\mathbf{x}_j^{(k)}) + \sum_{j=NS+NB+1}^{NS+NB+NL} \lambda_j^{(k)} Lp_i(\mathbf{x}_j^{(k)}) = 0 \qquad i = 1, ...., M \quad (4.50)$$

leads to the symmetric linear system

$$\begin{bmatrix} \mathbf{\Phi} & B_2[\mathbf{\Phi}] & L_2[\mathbf{\Phi}] & \mathbf{P}^{\mathrm{T}} \\ B_1[\mathbf{\Phi}] & B_1B_2[\mathbf{\Phi}] & B_1L_2[\mathbf{\Phi}] & B[\mathbf{P}^{\mathrm{T}}] \\ L_1[\mathbf{\Phi}] & L_1B_2[\mathbf{\Phi}] & L_1L_2[\mathbf{\Phi}] & L[\mathbf{P}^{\mathrm{T}}] \\ \mathbf{P} & B[\mathbf{P}] & L[\mathbf{P}] & \mathbf{0} \end{bmatrix}^{(k)} \begin{bmatrix} \boldsymbol{\lambda} \end{bmatrix}^{(k)} = \begin{bmatrix} \mathbf{c} \\ \mathbf{G} \\ \mathbf{S} \\ \mathbf{0} \end{bmatrix}^{(k)}, \quad (4.51)$$

where the vector $\mathbf{c}^{(k)}$ in the r.h.s. of (4.51) is unknown. The application of the differential operator $L$ at the centrepoint of the local system $k$ gives

$$S(\mathbf{x}_{\mathrm{cp}}^{(k)}) = L[c^{(k)}(\mathbf{x}_{\mathrm{cp}}^{(k)})] = L[\mathbf{H}^{(k)}(\mathbf{x}_{\mathrm{cp}}^{(k)})]\boldsymbol{\lambda}^{(k)} = (L[\mathbf{H}^{(k)}(\mathbf{x}_{\mathrm{cp}}^{(k)})][\mathbf{A}^{(k)}]^{-1})\mathbf{d}^{(k)} = \mathbf{W}_{\mathrm{L}}^{(k)}(\mathbf{x}_{\mathrm{cp}}^{(k)})\mathbf{d}^{(k)}, \quad (4.52)$$

where $\mathbf{A}^{(k)}$ and $\mathbf{d}^{(k)}$ are the matrix and the r.h.s of the linear system (4.51), respectively, and the row vector $\mathbf{H}^{(k)}(\mathbf{x}_{\mathrm{cp}}^{(k)})$ is

$$\begin{aligned} \mathbf{H}^{(k)}(\mathbf{x}_{\mathrm{cp}}^{(k)}) = & [\phi(|\mathbf{x}_{\mathrm{cp}}^{(k)} - \mathbf{x}_1^{(k)}|) \cdot\cdot \phi(|\mathbf{x}_{\mathrm{cp}}^{(k)} - \mathbf{x}_{NS}^{(k)}|) \\ & B_2[\phi(|\mathbf{x}_{\mathrm{cp}}^{(k)} - \mathbf{x}_{NS+1}^{(k)}|)] \cdot\cdot B_2[\phi(|\mathbf{x}_{\mathrm{cp}}^{(k)} - \mathbf{x}_{NS+NB}^{(k)}|)] \\ & L_2[\phi(|\mathbf{x}_{\mathrm{cp}}^{(k)} - \mathbf{x}_{NS+NB+1}^{(k)}|)] \cdot\cdot L_2[\phi(|\mathbf{x}_{\mathrm{cp}}^{(k)} - \mathbf{x}_N^{(k)}|)] \\ & p_1(\mathbf{x}_{\mathrm{cp}}^{(k)}) \cdot\cdot p_M(\mathbf{x}_{\mathrm{cp}}^{(k)})]. \end{aligned} \quad (4.53)$$

Eq. (4.52) provides a relation between the unknown values $c_i^{(k)}$, $i$=1, 2, .., $NS$ at the solution centres. Therefore, if this operation is applied to every local system, a sparse global linear system of equations for all the solution centres in the computational domain is obtained. The boundary conditions of the problem are implicitly taken into account since they have already been imposed at the

local level in the stencils containing boundary centres.

In the more general case of an initial-boundary value problem

$$\frac{\partial c(\mathbf{x},t)}{\partial t} = L[c(\mathbf{x},t)] + S(\mathbf{x}), \tag{4.54}$$

$$B[c(\mathbf{x},t)] = G(\mathbf{x}), \tag{4.55}$$

$$c(\mathbf{x},0) = c^0(\mathbf{x}), \tag{4.56}$$

the local RBF Hermitian method can be adopted after a casting of the time-dependent problem into a pseudo-stationary one. Using a first-order implicit approximation of the time derivative, the differential equation (4.54) can be rewritten as follows

$$\frac{c^n(\mathbf{x}) - c^o(\mathbf{x})}{\Delta t} = L[c^n(\mathbf{x})] + S(\mathbf{x}), \tag{4.57}$$

where $c^n(\mathbf{x})$ and $c^o(\mathbf{x})$ denote $c(\mathbf{x},t^n)$ and $c(\mathbf{x},t^o)$, respectively. By introducing the modified linear differential operator $\overline{L}$

$$\overline{L} = 1 - \Delta t L, \tag{4.58}$$

the pseudo-stationary formulation of Eq. (4.57) reads

$$\overline{L}[c^n(\mathbf{x})] = c^o(\mathbf{x}) + S(\mathbf{x})\Delta t = \overline{S}^o(\mathbf{x}). \tag{4.59}$$

The local RBF Hermitian method described above is used to solve Eq. (4.59) together with the boundary conditions (4.55) at each time-step. After having obtained the solution at a certain instance, the corresponding $c$-field serves to calculate the source term $\overline{S}^o$ for the next time-step. In principle, the first-order scheme for the time derivative could be replaced with other approximations yielding different expressions for the modified linear differential operator and the source term.

A special feature of this method is the implicit *upwinding*. It is well known that for convective-dominated problems the numerical scheme has to take into account the magnitude and the direction of the local velocity field in order to avoid spurious oscillations in the solution. Stevens et al. showed that the Hermitian characteristic of the local interpolation, which requires the fulfillment of the PDE (4.42) or (4.59) at some centres around the local system centrepoint, provides an implicit upwinding effect even in the case of spherically-symmetric stencils.

Although the local RBF Hermitian method has been proven to tackle accurately several different problems, it needs the solution of a large global system and many small local ones. The determination of the local matrix coefficients is considerably expensive since it involves many operations for the computations of the basis function derivatives. Furthermore, in the case of time-dependent differential operators, as for advection problems with velocity fields variable in time, the $\mathbf{A}^{(k)}$ coefficients change continuously. Since the small systems are usually treated by means of direct linear solvers, the time-dependency of $L$ makes necessary to invert the local matrices at every time-step. For all these reasons,

the local RBF Hermitian method represents a step forward with respect to the Kansa's and Fasshauer's global methods, but not yet sufficiently efficient for the solution of the extremely thin concentration boundary layers of the species transfer processes.

The method of Sărler and Vertnik (2006) presents the advantages that the local matrices can be inverted only once and no global system has to be solved. The former aspect derives from the replacement of the Hermitian interpolation with a standard one. Each local interpolant reads

$$c^{(k)}(\mathbf{x}) = \sum_{j=1}^{N} \lambda_j^{(k)} \phi(|\mathbf{x} - \mathbf{x}_j^{(k)}|) + \sum_{j=1}^{M} \lambda_{N+j}^{(k)} p_j(\mathbf{x}), \tag{4.60}$$

where $N$ is equal to $NS+NB$. The boundary nodes are treated as solution centres at the local level. This means that the first set of conditions in Eq. (4.49) is applied at both the node types. The interpolation problem leads to the following symmetric linear system

$$\begin{bmatrix} \mathbf{\Phi} & \mathbf{P}^{\mathrm{T}} \\ \mathbf{P} & \mathbf{0} \end{bmatrix}^{(k)} \begin{bmatrix} \boldsymbol{\lambda} \end{bmatrix}^{(k)} = \begin{bmatrix} \mathbf{c} \\ \mathbf{0} \end{bmatrix}^{(k)}. \tag{4.61}$$

The matrix in Eq. (4.61) depends only on the position of the discretisation points. Therefore, their coefficients do not change unless the points are moved. Accordingly, the inverse of these matrices can be computed at the beginning of the simulation and then stored.

The lack of a global system follows from the adoption of an explicit time-stepping which implies that the vector $\mathbf{c}^{(k)}$ in the r.h.s. of Eq. (4.61) consists of the values at the old time instance. Hence, the local systems become uncoupled and can be solved independently from each other. After their solution, the new value at each centrepoint is calculated as follows

$$c^{n}(\mathbf{x}_{\mathrm{cp}}^{(k)}) = c^{o}(\mathbf{x}_{\mathrm{cp}}^{(k)}) + \Delta t(L[c^{(k)}(\mathbf{x}_{\mathrm{cp}}^{(k)})] + S(\mathbf{x}_{\mathrm{cp}}^{(k)})). \tag{4.62}$$

For the local systems including one or more Neumann boundary nodes, a second step is performed. The system

$$\begin{bmatrix} \mathbf{\Phi} & B_2[\mathbf{\Phi}] & \mathbf{P}^{\mathrm{T}} \\ B_1[\mathbf{\Phi}] & B_1B_2[\mathbf{\Phi}] & B[\mathbf{P}^{\mathrm{T}}] \\ \mathbf{P} & B[\mathbf{P}] & \mathbf{0} \end{bmatrix}^{(k)} \begin{bmatrix} \boldsymbol{\lambda} \end{bmatrix}^{(k)} = \begin{bmatrix} \mathbf{c} \\ \mathbf{G} \\ \mathbf{0} \end{bmatrix}^{(k)} \tag{4.63}$$

is considered, where $\mathbf{c}^{(k)}$ contains now the new values at the solution centres. After having determined the coefficients $\boldsymbol{\lambda}^{(k)}$ in Eq. (4.63), the updated value of the generic Neumann node $\mathbf{x}_{\mathrm{NEU},i}^{(k)}$ is computed as

$$c^{(k)}(\mathbf{x}_{\mathrm{NEU},i}^{(k)}) = \mathbf{H}^{(k)}(\mathbf{x}_{\mathrm{NEU},i}^{(k)})\boldsymbol{\lambda}^{(k)}, \tag{4.64}$$

where the row vector $\mathbf{H}^{(k)}(\mathbf{x}_{\mathrm{NEU},i}^{(k)})$ is

$$\begin{aligned}\mathbf{H}^{(k)}(\mathbf{x}^{(k)}_{\mathrm{NEU},i}) =&[\phi(|\mathbf{x}^{(k)}_{\mathrm{NEU},i}-\mathbf{x}^{(k)}_{1}|)\cdot\cdot\,\phi(|\mathbf{x}^{(k)}_{\mathrm{NEU},i}-\mathbf{x}^{(k)}_{NS}|)\\ &B_2[\phi(|\mathbf{x}^{(k)}_{\mathrm{NEU},i}-\mathbf{x}^{(k)}_{NS+1}|)]\cdot\cdot\,B_2[\phi(|\mathbf{x}^{(k)}_{\mathrm{NEU},i}-\mathbf{x}^{(k)}_{NS+NB}|)]\\ &p_1(\mathbf{x}^{(k)}_{\mathrm{NEU},i})\cdot\cdot\,p_M(\mathbf{x}^{(k)}_{\mathrm{NEU},i})].\end{aligned} \tag{4.65}$$

Since a certain boundary node can belong to distinct local systems, an average of the different values obtained from Eq. (4.64) is needed. Sărler and Vertnik have not reported the procedure adopted in their work. However, a weighted averaged based on the distances between the boundary point and the centrepoints of the corresponding local systems represents a reasonable choice for this scope.

#### 4.2.1.4 Explicit Boundary RBF Finite-Difference method

As outlined in the previous subsection, the method of Sărler and Vertnik outperforms the other RBF-based numerical techniques in terms of computational cost. In the present work, this method has been simplified. The second step dedicated to the update of the values at Neumann boundary nodes has been eliminated by the enforcement of the boundary conditions directly into the first set of local linear systems, in analogy to the boundary treatment of the local RBF Hermitian method by Stevens et al. Therefore, the interpolant becomes

$$c^{(k)}(\mathbf{x}) = \sum_{j=1}^{NS}\lambda_j^{(k)}\phi(|\mathbf{x}-\mathbf{x}_j^{(k)}|) + \sum_{j=NS+1}^{NS+NB}\lambda_j^{(k)}B_2\phi(|\mathbf{x}-\mathbf{x}_j^{(k)}|) + \sum_{j=1}^{M}\lambda_{N+j}^{(k)}p_j(\mathbf{x}), \tag{4.66}$$

with $N$=$NS$+$NB$. Applying the first and second set of constraints of (4.49) at the solution and boundary centres, respectively, a local linear system analogous to that one in (4.63) is obtained. The only difference is that the vector $\mathbf{c}^{(k)}$ contains now the solution values at the old time instance. After having solved these systems and determined the coefficients $\boldsymbol{\lambda}^{(k)}$, the new internal and boundary values are calculated by means of Eqs. (4.62) and (4.64), respectively. The inverse distance weighted average mentioned above has been used to generate unique values at the Neumann boundary nodes.

#### 4.2.1.5 Validation cases

The method described in the previous subsection has been implemented within the OpenFOAM framework. The implementation required the development of completely new libraries.

In the following, different validation cases with increasing complexity are presented. The Gaussian RBF has been used in all the simulations. The shape parameter $\epsilon$ for each local system $k$ has been made adaptive by setting it according to the local distance between the nodes.

**One-phase validation cases**

As a first step, the method has been validated against one-phase test cases. Therefore, the further complication related to the presence of two different regions with transmission conditions at their interface has been neglected here. First, the problem of the diffusion between two planes has been

considered. An uniform value of 1 mol/m$^3$ is kept constant on two infinite planes placed at $x$=$\pm l$, respectively. A zero initial value is set in the intermediate region. The one-dimensional analytical solution of this problem (see Crank, 1979) is

$$c(x,t) = 1 - \frac{4}{\pi}\sum_{n=0}^{+\infty}\frac{(-1)^n}{2n+1}e^{-\frac{D(2n+1)^2\pi^2}{4l^2}t}\cos(\frac{(2n+1)\pi x}{2l}), \tag{4.67}$$

where $D$ is the diffusion coefficient. An equivalent version of this test case is obtained by considering only half of the domain and inserting a symmetry condition, i.e. zero normal gradient, at $x$=0.

Fig. 4.5 shows the left half of the domain with $l$=0.005 m used for the numerical simulation. The points have been randomly generated on a planar surface. Different point distributions with approximate spacing ranging from $5 \times 10^{-4}$ m to $5 \times 10^{-5}$ m have been tested. The local system for each node is made up of the adjacent neighbours. This results into an average size of 6-7 nodes. Additional zero normal gradient boundary conditions have been placed on two surfaces perpendicular to the lateral plane. This allows to make finite the height of the domain without introducing any modification compared to the original problem. The diffusivity $D$ has been set equal to $1 \times 10^{-5}$ m$^2$/s.

Fig. 4.6 shows the comparison between the numerical results obtained with three different "grids" and the analytical solution at the time $t$=0.01 s. It can be noted that the profile relating to the third point distribution is almost indistinguishable from the analytical one.

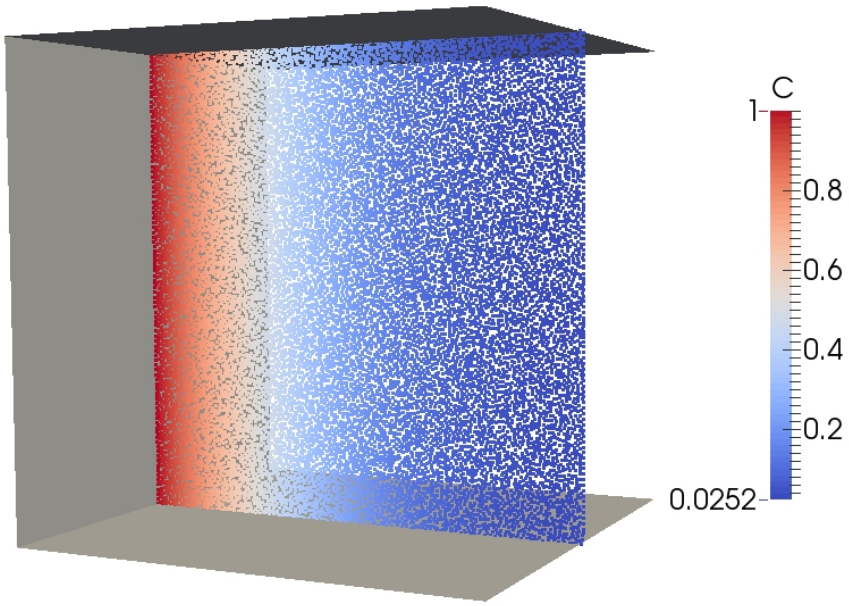


Figure 4.5: Domain and computational nodes colored by species concentration of the one-phase diffusion problem.

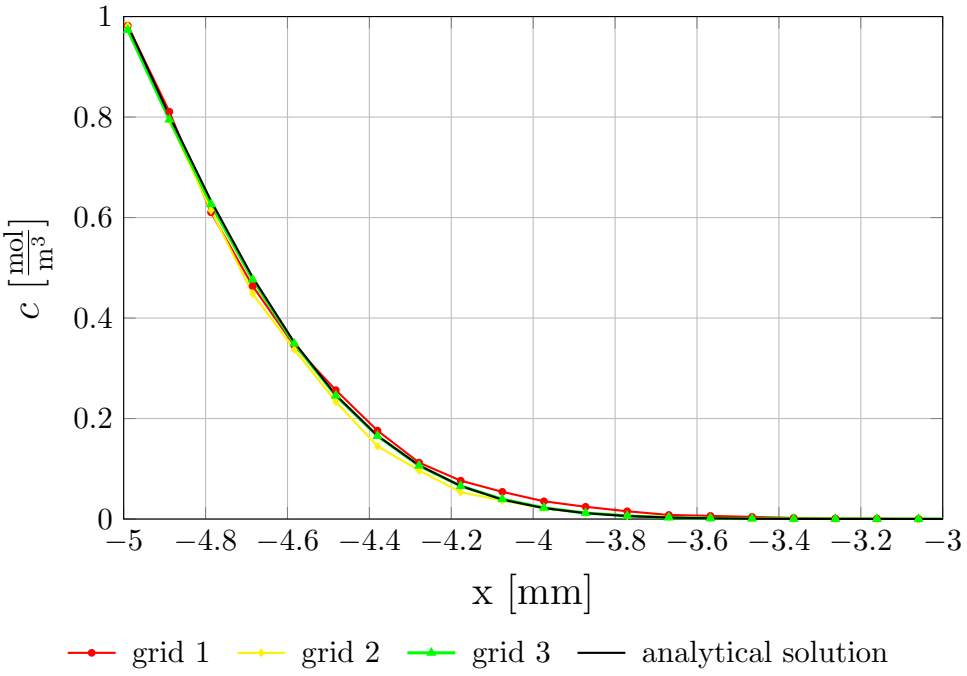


Figure 4.6: Comparison between the numerical results and the analytical solution for the one-phase diffusion problem.

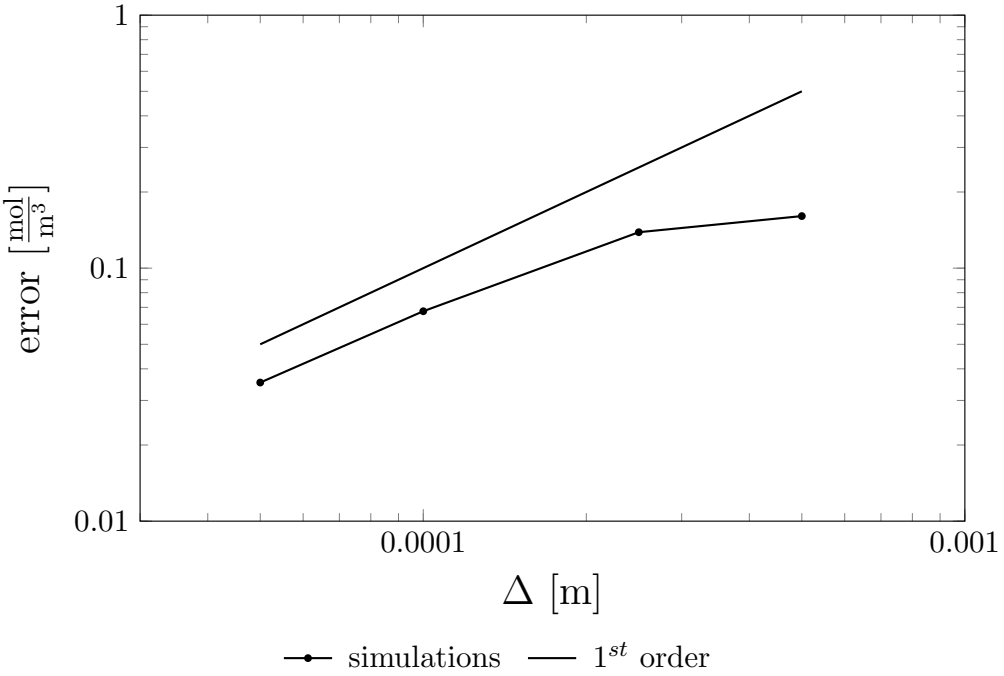


Figure 4.7: Error as function of the inter-point spacing $\Delta$ for the one-phase diffusion problem.

Fig. 4.7 reports the errors corresponding to the different simulations as function of the point spacing $\Delta$. The errors are computed as sum of the absolute differences between the numerical and analytical values of the profiles in Fig. 4.6. The figure highlights that the accuracy of the method tends to the first order as the distance between the computational nodes decreases.

In the second validation case, the transport of a species convected away from a spherical fluid interface with radius of 0.001 m by a flow in the Stokes regime has been considered. An uniform velocity vector with magnitude of 0.005 m/s is imposed at a spherical boundary surface with radius of 0.016 m. The closed-form expression of this velocity field has been obtained by Satapathy and Smith (1961). It depends on the ratio between the viscosities outside and inside the fluid interface. The ratio has been set here equal to 1000. An uniform concentration $c$=1 mol/m$^3$ is assigned at the inner surface, while a mixed Dirichlet/Neumann boundary condition is applied at the outer one. The mixed boundary condition prescribes a concentration value of 1 mol/m$^3$ or zero normal gradient in the case of inflow or outflow, respectively. The diffusion coefficient $D$ is assumed equal to 1e$-$05 m$^2$/s, yielding a Péclet number of 1. Zero initial concentration is considered in the region between the two spherical surfaces.

The closed-form solution of this transport problem is not known. For this reason, the reference solution has been provided by finite-volume numerical simulations using OpenFOAM. Different computations with increasing mesh resolution have been performed in order to obtain mesh-independent numerical results.

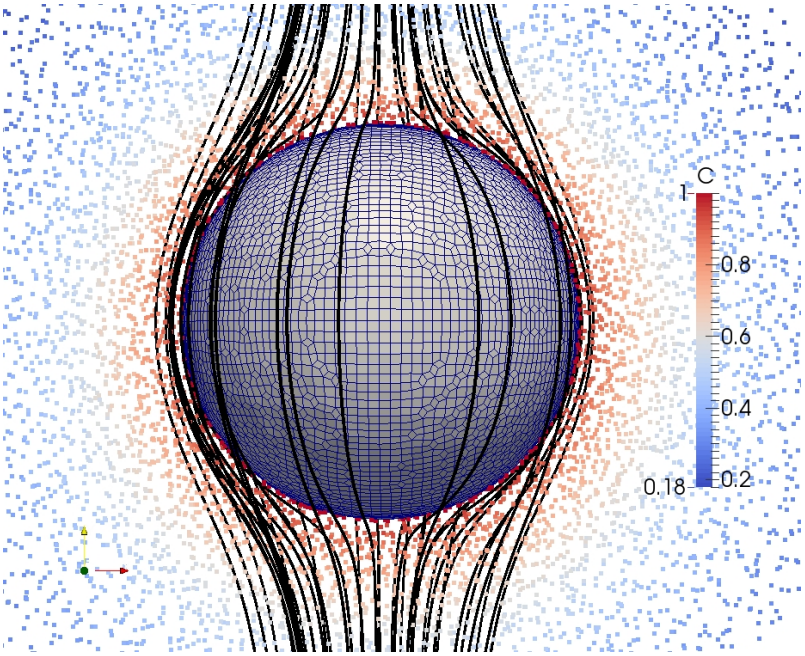


Figure 4.8: Part of the domain in the vicinity of the inner surface, streamlines and computational nodes colored by species concentration of the one-phase convection-diffusion problem.

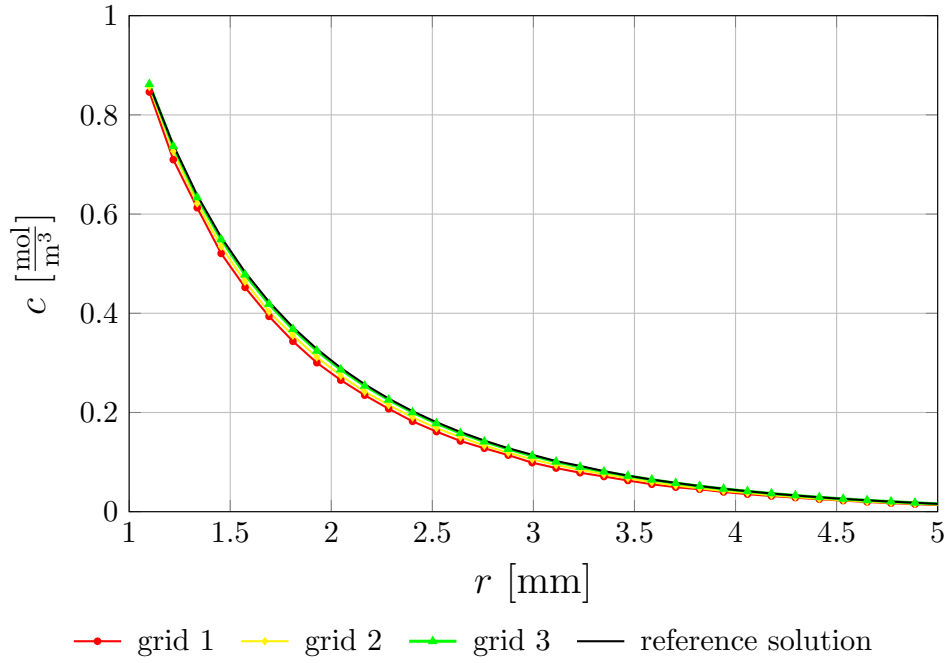


Figure 4.9: Comparison between the numerical results and the finite volume reference solution for the one-phase convection-diffusion problem.

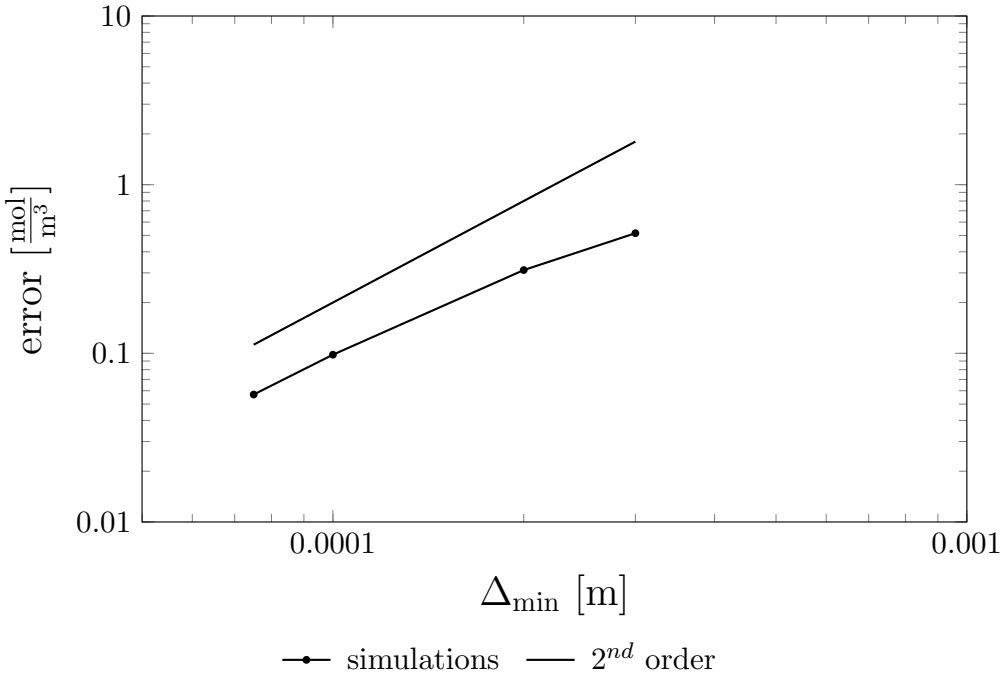


Figure 4.10: Error as function of the minimal inter-point spacing $\Delta_{\text{min}}$ for the one-phase convection-diffusion problem.

Fig. 4.8 shows the part of the domain close to the fluid interface. Different point distributions with approximate spacing at the interface ranging from 3e−04 m to 7.5e−05 m have been tested. A linear decay of the resolution moving away from the interface has been imposed. The ratio between the resolutions at the two spherical surfaces has been kept fixed to 4. The local system for each node is made up of the adjacent neighbours. This results into an average size of 12 nodes.

In Fig. 4.9 the numerical results obtained with three different point distributions are compared to the finite-volume reference solution on a radial line starting at the top of the bubble at the time $t$=0.5 s. The figure shows the convergence of the simulation results to the reference solution.

Fig. 4.10 reports the errors corresponding to the different simulations as function of the minimun point spacing $\Delta_{\min}$, i.e. at the fluid interface. The errors are computed as sum of the absolute differences between the numerical and reference values of the profiles in Fig. 4.9. A second-order accuracy emerges from Fig. 4.10 as the point distribution becomes finer. The increased order of accuracy derives from the adoption of larger stencils in comparison to those ones used in the previous test case.

**Two-phase validation cases**

The validation cases presented here regard the transport of an inert species across a fluid interface. In addition to the convection-diffusion conservation law, the solution has to fulfill the transmission conditions (3.14) and (3.15) at the interface. For this purpose, the explicit Dirichlet-Neumann coupling algorithm (see Weber et al., 2017) has been adopted in the present work. A Dirichlet b.c. is imposed at the side of the interface in the domain **A**, while a Neumann b.c. is assigned at the other side of the interface in the domain **B**. A single iteration of this algorithm consists of the following steps:

1. the convection-diffusion equation is solved in the domain **A**;
2. the solution in the domain **A** is used to update the interface normal gradients of the domain **B** according to Eq. (3.15);
3. the convection-diffusion equation is solved in the domain **B**;
4. the solution in the domain **B** is used to update the interface values of the domain **A** according to Eq. (3.14).

This procedure is repeated until both the transmission conditions are fulfilled within a prescribed tolerance. Relaxation factors have to be introduced in order to preserve the stability and accelerate the convergence rate of the method. A schematic diagram of the explicit Dirichlet-Neumann algorithm is depicted in Fig. 4.11.

In the first two-phase validation case, two domains identical to that one reported in Fig. 4.5 have been connected through the corresponding lateral planes. The two transmission conditions are imposed on the resulting connecting surface. Only the diffusion acts in the respective internal regions. The initial concentrations are 1 mol/m$^3$ and 0 mol/m$^3$, respectively. The length $l$ of each domain is equal to 0.005 m. The ratio between the concentrations at the two sides of the interface, i.e. the

Henry coefficient, is set to 30. The diffusion coefficient $D_1$ in the first region is 1e−04 $m^2/s$, while $D_2$ is 1e−06 $m^2/s$.

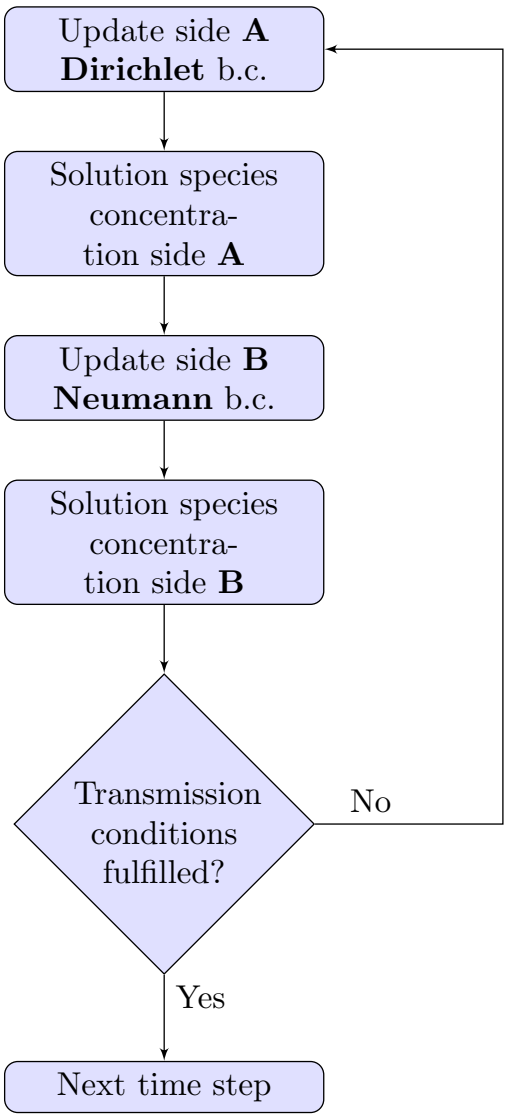


Figure 4.11: Explicit Dirichlet-Neumann coupling algorithm.

The analytical solution of this problem (see Crank, 1979) is

$$c(x,t) = \begin{cases} 1 + (C_1(t) - 1)[1 - \frac{4}{\pi}\sum_{n=0}^{+\infty} \frac{(-1)^n}{2n+1} e^{-\frac{D_1(2n+1)^2\pi^2}{4l^2}t} \cos(\frac{(2n+1)\pi x}{2l})], & 0 < x \leq l \\ \frac{C_1(t)}{\mathrm{H}}[1 - \frac{4}{\pi}\sum_{n=0}^{+\infty} \frac{(-1)^n}{2n+1} e^{-\frac{D_2(2n+1)^2\pi^2}{4l^2}t} \cos(\frac{(2n+1)\pi x}{2l})], & -l \leq x < 0 \end{cases} \tag{4.68}$$

with $C_1(t)$ representing the time-dependent concentration of the first region at the interface. Enforcing the second transmission condition, the following expression for $C_1(t)$ is obtained

$$C_1(t) = \frac{1}{1 + \frac{\sum_{n=0}^{+\infty} e^{-\frac{D_2(2n+1)^2\pi^2}{4l^2}t}}{\mathrm{H\,J}\sum_{n=0}^{+\infty} e^{-\frac{D_1(2n+1)^2\pi^2}{4l^2}t}}}, \tag{4.69}$$

where the factor J is equal to the ratio $D_1/D_2$.

The two sets of computational points used for the numerical simulation are shown in Fig. 4.12. The points have been randomly generated on a planar surface with an approximate spacing of 5e−05 m. The local system for each node is made up of the adjacent neighbours. This results into an average size of 6-7 nodes.

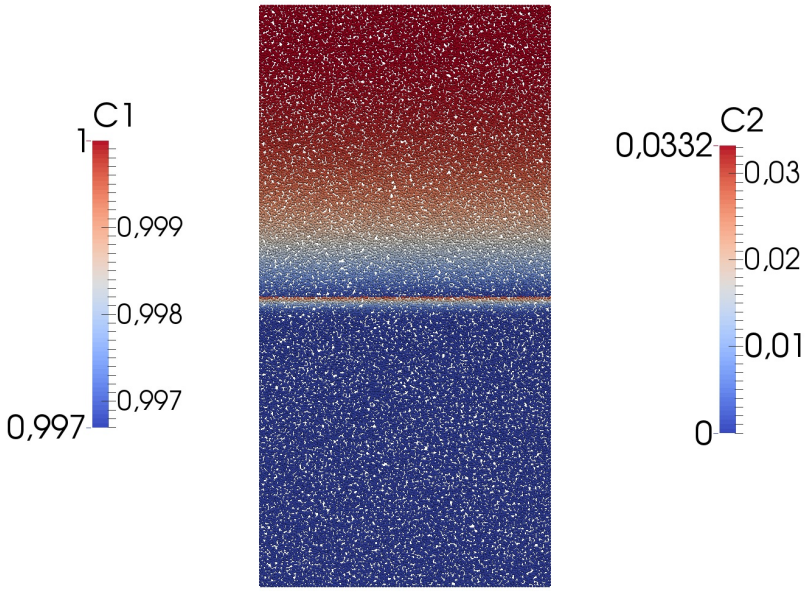


Figure 4.12: Domain and computational nodes colored by species concentration of the two-phase diffusion problem.

Fig. 4.13 reports the simulation and analytical values at the time $t$=0.01 s for small negative values of x. A good agreement between the two profiles is shown, concluding that the method is capable to solve accurately the considered problem.

The last validation case regards the two-phase convection-diffusion transport with Stokes flow inside and outside a spherical fluid interface. Different from the corresponding one-phase case, the species transport equation is solved here in both the regions. Furthermore, the two transmission conditions are imposed at the interface.

The values of the geometrical, kinematic and material parameters are equal to the ones used for the corresponding one-phase problem. Additionally, the diffusion coefficient $D_1$ in the inner region is

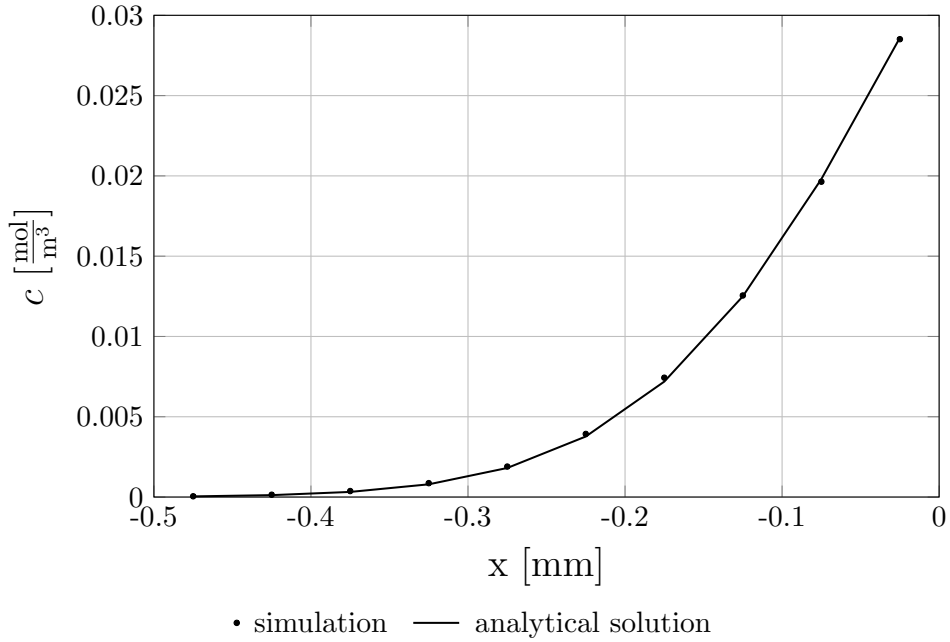


Figure 4.13: Comparison between the numerical results and the analytical solution for the two-phase diffusion problem.

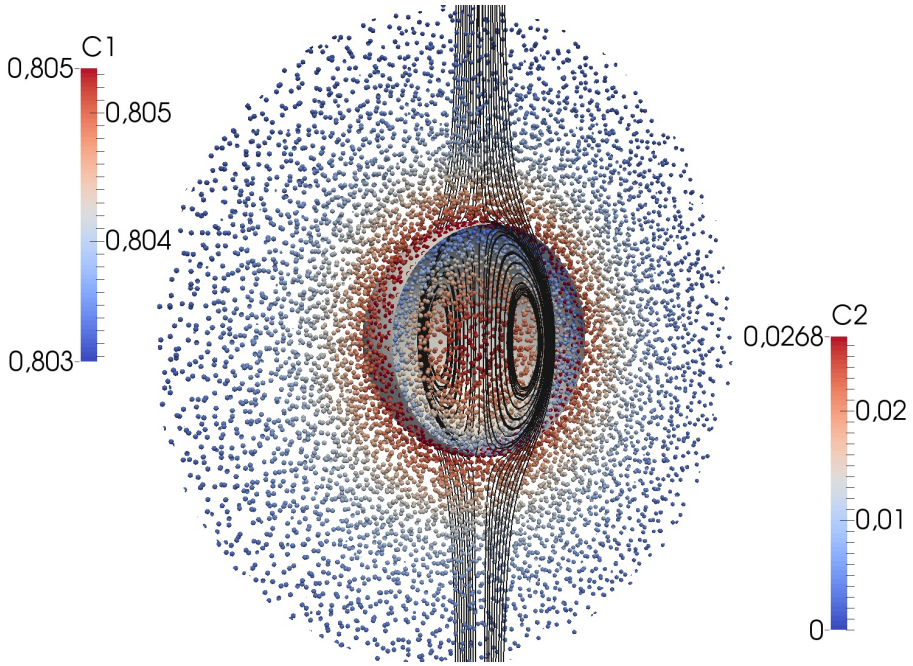


Figure 4.14: Domain, streamlines and computational nodes colored by species concentration of the two-phase convection-diffusion problem.

set to 1e−04 $m^2/s$. Accordingly, the value of J is 10. The Henry coefficient is chosen equal to 30. The initial concentrations inside and outside the fluid interface are 1 $mol/m^3$ 0 $mol/m^3$, respectively.

The analytical solution of this problem is not known. Similar to the corresponding one-phase case, the reference solution has been computed by means of finite-volume numerical simulations using OpenFOAM. Different mesh resolutions have been tested in order to obtain mesh-independent reference results.

A non-uniform point distribution with spacing at the interface equal to 1e−04 m has been employed. According to a linear grading coefficient of 4, the resolution at the outer boundary surface has been set to 4e−04 m. The local system for each node is made up of the adjacent neighbours. This results into an average size of 12 nodes.

The comparison between the reference and RBF solutions on a 2 mm-long radial line starting at the interface and crossing the outer region is shown in Fig. 4.15. The good agreement between the two profiles highlights the capability of the proposed RBF method to solve species transfer problems in the presence of low advective contribution.

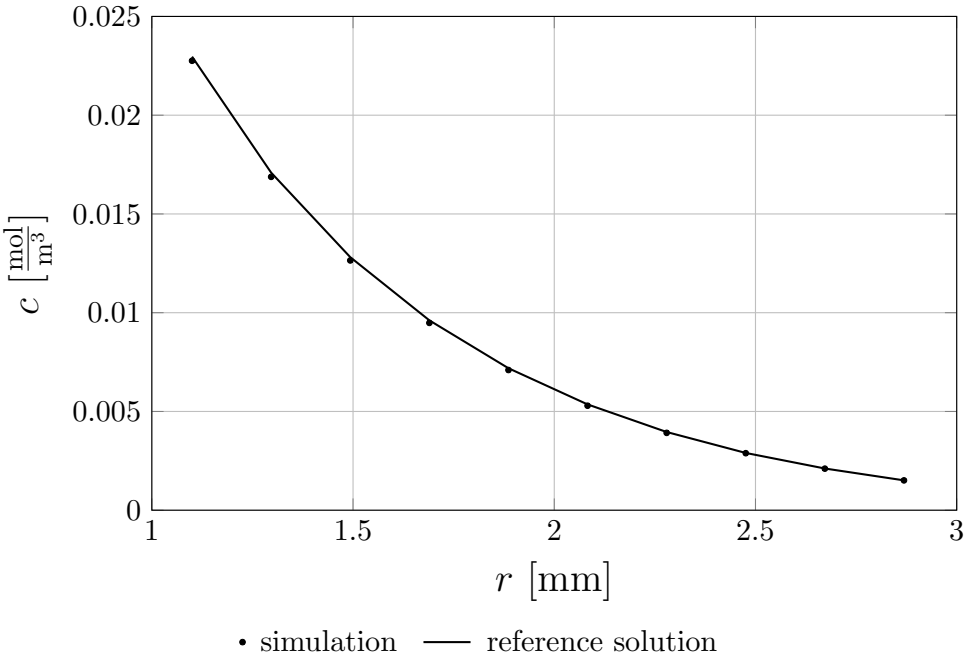


Figure 4.15: Comparison between the numerical results and the finite volume reference solution for the two-phase convection-diffusion problem.

#### 4.2.1.6 Critical aspects: time performances and stability issues

Although the validation cases of the previous subsection have been accurately solved by the developed RBF-based finite-difference method, two critical aspects emerged from these tests. The first regards the computational cost. In some cases, this turned out to be even ten time larger than that of a finite-

volume simulation at similar mesh resolution and inter-point spacing. Though some improvements could be gained with a more efficient code implementation, the gap between the two methods is so large that it is unlikely to reach comparable computational performances.

The second deficiency concerns the stability. Increasing the magnitude of the boundary velocity in the convection-diffusion problem with Stokes flow around a fluid interface, the simulation has proved to be soon unstable with concentration values in the inner part of the domain larger than at the interface.

In order to introduce an upwinding effect, a different approach based on the adoption of a different stencil for the discretisation of the convective term has been considered. The plane (or line in 2D) passing through a generic local centrepoint and perpendicular to its velocity vector divides the space in two parts. The subset of the original stencil containing only the nodes in the upstream half is used for the numerical treatment of the convection. This modification yields a slight improvement, though an intrinsic stability cannot be guaranteed.

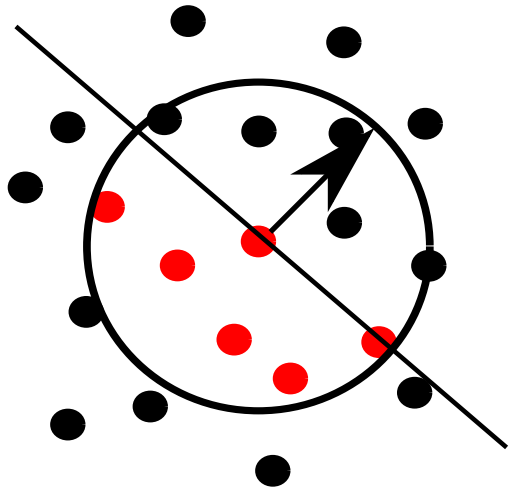

Figure 4.16: Example of upwind stencil; the red dots are used for the discretisation of the convective term.

Another attempt to solve the stability issue has been made by building up the numerical method on a Hermitian RBF interpolation. As shown by Stevens et al., the introduction of PDE centres in the interpolation problem provides an implicit upwinding effect. However, their method, which has been already described in Section 4.2.1.3, is computationally expensive. In order to make it more performant, its formulation has been adapted to an explicit approach. This has been obtained by removing from the local interpolants the first $NS$ terms and, at the same time, adding the centrepoint to the list of PDE centres. The resulting expression for the $k^{\text{th}}$ interpolant is

$$c^{(k)}(\mathbf{x}) = \sum_{j=1}^{NB} \lambda_j^{(k)} B_2\phi(|\mathbf{x} - \mathbf{x}_j^{(k)}|) + \sum_{j=NB+1}^{NB+NL} \lambda_j^{(k)} \overline{L}_2\phi(|\mathbf{x} - \mathbf{x}_j^{(k)}|) + \sum_{j=1}^{M} \lambda_{N+j}^{(k)} p_j(\mathbf{x}), \tag{4.70}$$

where $N$ is here equal to $NS + NB$. Accordingly, the first set of constraints in (4.49) has been eliminated from the local linear system of equations which reads now

$$\begin{bmatrix} B_1B_2[\mathbf{\Phi}] & B_1\overline{L}_2[\mathbf{\Phi}] & B[\mathbf{P}^{\mathrm{T}}] \\ \overline{L}_1B_2[\mathbf{\Phi}] & \overline{L}_1\overline{L}_2[\mathbf{\Phi}] & \overline{L}[\mathbf{P}^{\mathrm{T}}] \\ B[\mathbf{P}] & \overline{L}[\mathbf{P}] & \mathbf{0} \end{bmatrix}^{(k)} \begin{bmatrix} \boldsymbol{\lambda} \end{bmatrix}^{(k)} = \begin{bmatrix} \mathbf{G} \\ \mathbf{S} \\ \mathbf{0} \end{bmatrix}^{(k)}. \tag{4.71}$$

The polynomial reproduction conditions have been modified as follows

$$\sum_{j=1}^{NB} \lambda_j^{(k)} Bp_i(\mathbf{x}_j^{(k)}) + \sum_{j=NB+1}^{NB+NL} \lambda_j^{(k)} \overline{L}p_i(\mathbf{x}_j^{(k)}) = 0 \qquad i = 1, ...., M. \tag{4.72}$$

The field value at the new time instance for a generic discretisation point is calculated by simply retrieving the value of the corresponding interpolant at the local centrepoint. This yields

$$c^n(\mathbf{x}_{\mathrm{cp}}^{(k)}) = \mathbf{H}^{(k)}(\mathbf{x}_{\mathrm{cp}}^{(k)})\boldsymbol{\lambda}^{(k)} = \mathbf{H}^{(k)}(\mathbf{x}_{\mathrm{cp}}^{(k)})(\mathbf{A}^{(k)})^{-1}\mathbf{d}^{(k)} = \mathbf{W}^{(k)}(\mathbf{x}_{\mathrm{cp}}^{(k)})\mathbf{d}^{(k)}, \tag{4.73}$$

where the row vector $\mathbf{W}^{(k)}(\mathbf{x}_{\mathrm{cp}}^{(k)})$ is given by the product between

$$\begin{aligned} \mathbf{H}^{(k)}(\mathbf{x}_{\mathrm{cp}}^{(k)}) =& [B_2[\phi(|\mathbf{x}_{\mathrm{cp}}^{(k)} - \mathbf{x}_1^{(k)}|)] \cdot\cdot B_2[\phi(|\mathbf{x}_{\mathrm{cp}}^{(k)} - \mathbf{x}_{NB}^{(k)}|)] \\ & L_2[\phi(|\mathbf{x}_{\mathrm{cp}}^{(k)} - \mathbf{x}_{NB+1}^{(k)}|)] \cdot\cdot L_2[\phi(|\mathbf{x}_{\mathrm{cp}}^{(k)} - \mathbf{x}_N^{(k)}|)] \\ & p_1(\mathbf{x}_{\mathrm{cp}}^{(k)}) \cdot\cdot p_M(\mathbf{x}_{\mathrm{cp}}^{(k)})] \end{aligned} \tag{4.74}$$

and the inverse of the local system matrix. The adoption of a Hermitian RBF interpolation leads to an improvement regarding the stability. However, even in this case it is not possible to achieve an intrinsic stability.

Though the results of Stevens et al. have shown slight under- and overshoots in some advective-dominated test cases, the unboundedness grows slowly in time. On the contrary, larger growth rates of the solution unboundedness emerged from the computations of the current study. The difference might be due to the dissimilarity between the node arrangements. Stevens adopted in the majority of the cases structured sets of nodes. Only in some test cases he opted for scattered points, though the spacing between the nodes does not exihibit significant spatial variations. In the present case, the need for high resolutions at the interface imposes the presence of a considerable grading of the point spacing.

The change from an implicit to an explicit method represents a further possible cause of instability. However, as previously pointed out, the implicit approach proposed by Stevens et al. is computationally excessively expensive and, therefore, it does not represent a viable way to cope with the very thin concentration boundary layers.

In consequence of the highlighted stability issues, it turned out that the current formulations of the RBF method do not allow to deal with advective-dominated problems, as necessary for the investigation of species transfer processes at bubble interfaces.

### 4.2.2 Two-mesh approach

The second numerical method for the solution of the species transport equations relies on a finite-volume discretisation. Hence, the concentration equation (3.13) for a generic component $k$ is rewritten as follows

$$\frac{d}{dt}\int_{V(t)} c_k \, dV + \oint_{S(t)} \mathbf{n}\cdot(\mathbf{v}-\mathbf{v}_S)c_k \, dS = \oint_{S(t)} \mathbf{n}\cdot(D_k\nabla c_k)\, dS \tag{4.75}$$

by integration on a moving non-material control volume $V(t)$. As already mentioned before, the chemical reaction terms are disregarded in this context. The discretised form of the convection-diffusion transport equation (4.75) for a generic cell $P$ with volume $V_P$ is

$$\frac{3c^n_{k,P}V^n_P - 4c^o_{k,P}V^o_P + c^{oo}_{k,P}V^{oo}_P}{2\Delta t} + \sum_f \left(\frac{\dot{m}^n_f}{\rho_f} - \dot{V}^n_f\right) c^n_{k,f} = \sum_f D_{k,f}\mathbf{n}^n_f \cdot (\nabla c_k)^n_f S^n_f. \tag{4.76}$$

Due to the low species diffusion coefficients in the liquid phase, an accurate solution of Eq. (4.76) requires a mesh resolution higher than that one needed for the two-phase hydrodynamics. Therefore, the name of the approach derives from the fact that the two problems are solved by means of different meshes.

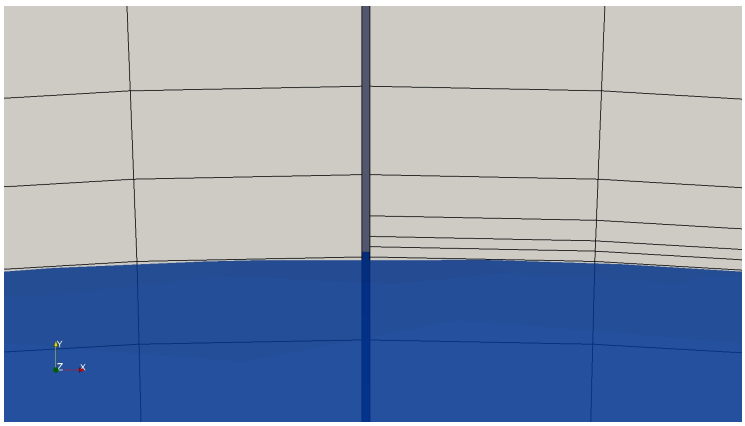

Figure 4.17: Example of mesh refinement.

Refining the liquid-sided interfacial cell layer of the hydrodynamic grid in normal direction, along which the largest concentration variations occur, provides a second mesh sufficiently fine to accurately resolve the species transfer. This can be performed straightforwardly due to the presence of surface-fitted prismatic cell layers around the interface, as visible in Fig. 4.2. Fig. 4.17 shows side by side the two meshes. The high diffusion coefficients inside the bubble determine small concentration gradients within the gas phase which can be captured without any refinement in this region.

The two meshes do not differ significantly from each other regarding the overall number of cells. In terms of computational costs, it could be possible to employ solely the finer mesh for both the problems. However, the stability of the hydrodynamic algorithm is more problematic than that one of the

species transfer. This imposes more severe limitations on the cell grading in the vicinity of the interface. For this reason, it is necessary to solve the flow field problem on a less varying grid, adopting the aggressive grading towards the bubble surface only for the solution of the species transport equations.

The velocity field has to be mapped from the coarser to the finer mesh. An inverse distance weighted interpolation represents a straightforward way to perform the mapping. The cell-face mass fluxes $\dot{m}'_f{=}\rho_f \mathbf{n}_f^n \cdot \mathbf{v}'_f S_f^n$, where $\mathbf{v}'_f$ indicates the velocity vector obtained from this interpolation procedure, do not generally fulfill the discretised mass balance. In order to get a divergence-free mapped velocity field, a Laplace equation for the pressure correction $p'$ is solved on the refined mesh. This equation reads

$$\sum_f \mathbf{n}_f^n \cdot (\nabla p')_f^n S_f^n \Delta t = \sum_f \left( \frac{\dot{m}'_f}{\rho_f} \right). \tag{4.77}$$

After having solved Eq. (4.77), the cell-face mass fluxes are corrected as follows

$$\dot{m}_f^n = \dot{m}'_f - \rho_f \mathbf{n}_f^n \cdot (\nabla p')_f^n S_f^n \Delta t, \tag{4.78}$$

ensuring the solenoidality of the velocity field.

The second mesh needs to be displaced during the simulation in accordance with the motion of the hydrodynamic mesh. This can be achieved with negligible computational overhead due to the high similarity between the two grids. An identical displacement can be applied for the large amount of coincident nodes. Each additional point created in the refinement process is located on some edge of the hydrodynamic mesh. Its movement is computed by using the nodal displacements of the corresponding edge through an inverse distance weighted interpolation.

As for the velocity field, a mixed Dirichlet-Neumann boundary condition is employed for all the species at the outer spherical surface. A prescribed uniform inlet value $c_{A,\mathrm{in}}$ is set for $A$, while 0 mol/m$^3$ is assigned to the other species.

The explicit Dirichlet-Neumann coupling algorithm, as described in Section 4.2.1.5, is adopted to enforce the transmission conditions (3.14) and (3.15).

#### 4.2.2.1 Validation

The two-mesh approach has been implemented within the OpenFOAM framework using the finite-volume library already present in the original software distribution.

A physisorption problem for an almost spherical rising bubble with $d_b$=1.49 mm has been chosen as a validation case. The adopted values of the hydrodynamic and species transfer material parameters are reported in Tab. 4.1. The values of the material parameters of the two phases can be considered to be representative of an air bubble in a glycol-water mixture. The initial concentration of the species $B$ in the gas phase has been set to 8.72 mol/m$^3$. The Henry coefficient $\mathrm{H}_B$ has been chosen equal to 30.

The height of the first liquid-sided cell layer at the interface is around 4.5 μm. Four different meshes

have been considered for the species transfer problem applying from zero up to three refinement levels.

The resulting bubble rise velocity $U_b$ is 0.174 m/s corresponding to a bubble Reynolds number $\mathrm{Re}_b$ of about 58. As it can be computed by using the values in Tab. 4.1, the Schmidt number $\mathrm{Sc}_B$ is 1e04. Accordingly, the Péclet number $\mathrm{Pe}_B$ is approximately 5.8e05.

Table 4.1: Values of the material parameters for the validation case of the two-mesh approach.

| Parameter | Value and Units |
|---|---|
| $\mu_l$ | 4.46e−03 $\frac{\mathrm{kg}}{\mathrm{ms}}$ |
| $\mu_g$ | 1.81e−05 $\frac{\mathrm{kg}}{\mathrm{ms}}$ |
| $\rho_l$ | 1000 $\frac{\mathrm{kg}}{\mathrm{m}^3}$ |
| $\rho_g$ | 1.205 $\frac{\mathrm{kg}}{\mathrm{m}^3}$ |
| $\sigma$ | 0.073 $\frac{\mathrm{kg}}{\mathrm{s}^2}$ |
| $D_{B,l}$ | 4.46e−10 $\frac{\mathrm{m}^2}{\mathrm{s}}$ |
| $D_{B,g}$ | 4.46e−04 $\frac{\mathrm{m}^2}{\mathrm{s}}$ |

Table 4.2: Sherwood number values for the validation case of the two-mesh approach.

| No. refinements | Sherwood |
|---|---|
| 0 | 551.4 |
| 1 | 692.9 |
| 2 | 711 |
| 3 | 707 |

Fig. 4.18 shows the concentration field on a longitudinal section for the four different meshes. In comparison to Fig. 4.18a, the employment of one refinement level determines drastic changes regarding the concentration boundary layer. Almost no differences are visible with finer meshes. However, the quantitative information provided in Tab. 4.2 highlights that the Sherwood number is subjected to further significant variations by adopting more than one refinement. This is confirmed by Fig. 4.19 in which the local Sherwood number profiles along the polar angle relating to the four cases are reported. In fact, the addition of a second refinement step results into noticeable modifications of the local profile.

The results can be compared to the correlation of Takemura and Yabe (1998) for the Sherwood number. The correlation has been obtained by revising a coefficient of the expression

$$\mathrm{Sh}_{\mathrm{eq}} = \frac{2}{\sqrt{\pi}}\left(1 - \frac{2}{3}\frac{1}{\left(1 + 0.1415\mathrm{Re}_b^{2/3}\right)^{3/4}}\right)^{1/2}(2.5 + \sqrt{\mathrm{Pe}_B}) \tag{4.79}$$

given by Clift et al. (1978) in order to improve the agreement with their experimental results. Ac-

cording to their correction, Eq. (4.79) becomes

$$\mathrm{Sh}_{\mathrm{eq}} = \frac{2}{\sqrt{\pi}}\left(1 - \frac{2}{3}\frac{1}{\left(1 + 0.09\mathrm{Re}_b^{2/3}\right)^{3/4}}\right)^{1/2}(2.5 + \sqrt{\mathrm{Pe}_B}). \tag{4.80}$$

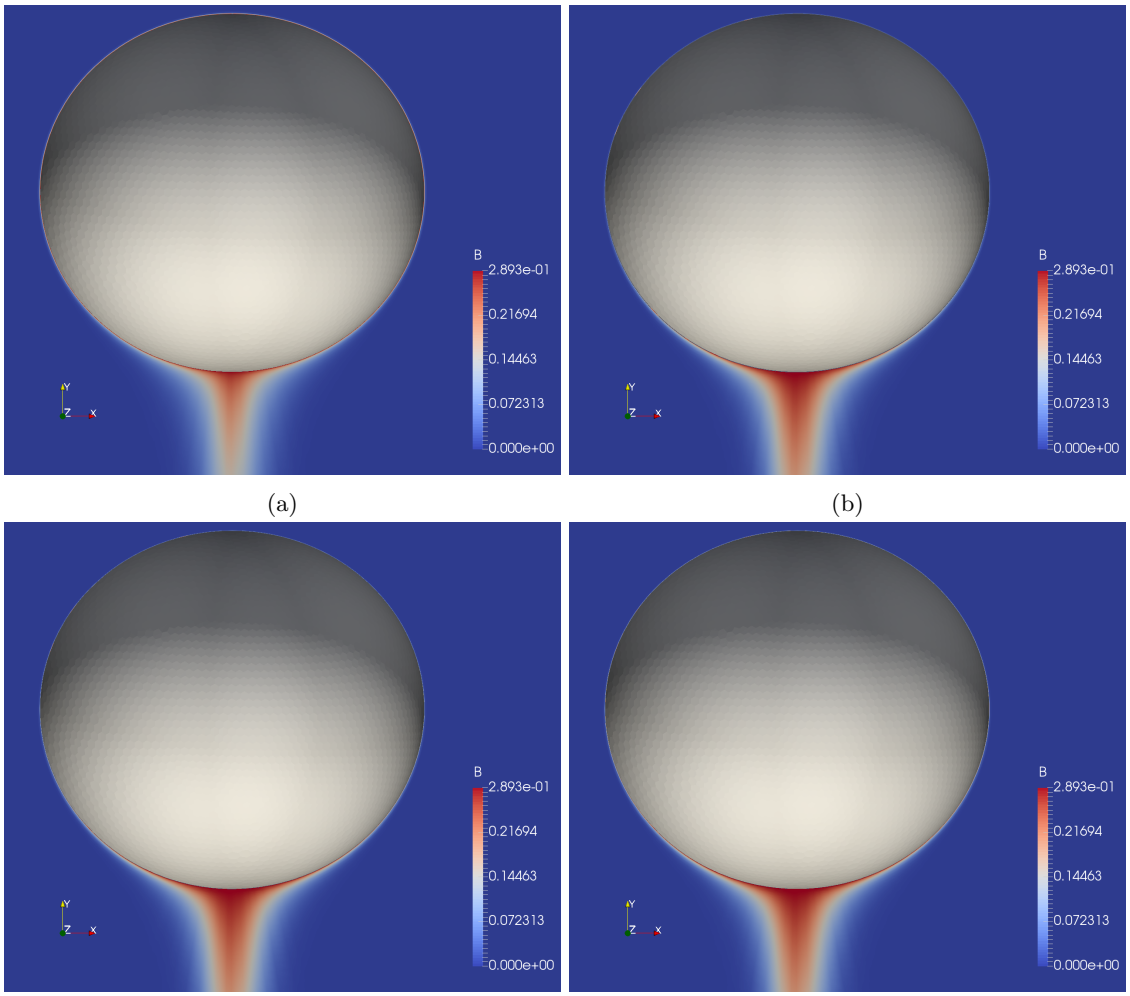


Figure 4.18: Concentration field of the species B on a longitudinal section for the four meshes with zero up to three refinement levels.

The validity range is for $\mathrm{Re}_b \leq 100$ and $\mathrm{Pe}_B > 1$. The equivalent Sherwood number $\mathrm{Sh}_{\mathrm{eq}}$ in Eqs. (4.79) and (4.80) is given by the product between Sh and the factor $A_{b,\mathrm{eq}}/A_b$. The term $A_{b,\mathrm{eq}}$ represents the area of the spherical bubble with equivalent volume. Since the bubble considered in this validation test is nearly spherical, the factor $A_{b,\mathrm{eq}}/A_b$ is virtually one. Therefore, the difference between the Sh and $\mathrm{Sh}_{\mathrm{eq}}$ values is negligible.

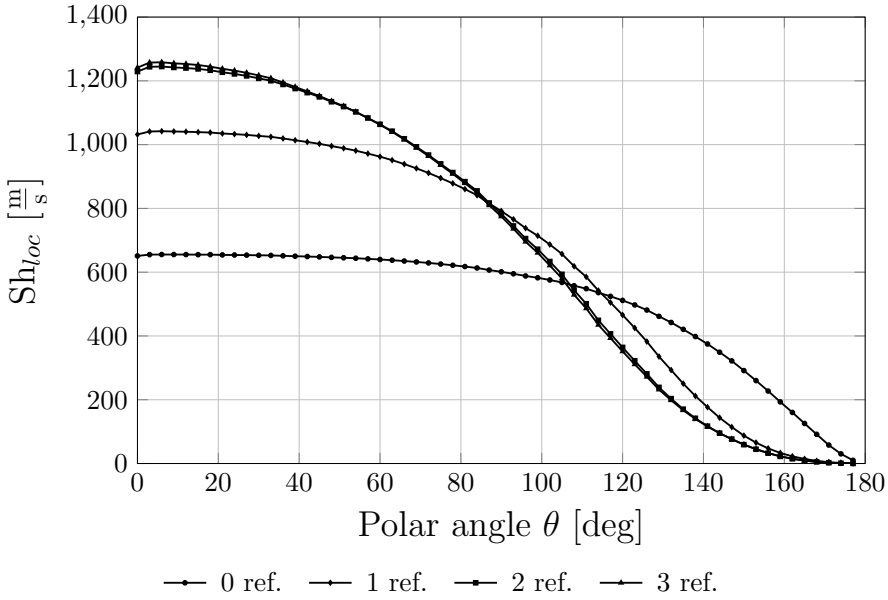


Figure 4.19: Local Sherwood number as function of the polar angle for the four meshes with zero up to three refinement levels.

The correlation (4.80) gives for this problem a value of approximately 696. The result obtained with the finest mesh (see Tab. 4.2) differs from this value by 1.5% against the 20.8% corresponding to the case without any refinement. This allows to conclude that the two-mesh approach with a suitable number of refinements is able to solve accurately the species transfer in case of high Péclet numbers.

# Chapter 5

# Investigation of species transfer from deformable single rising bubbles

In this chapter the results of species transfer simulations with and without chemical reactions using the two-mesh approach are presented and discussed. In order to investigate the sensitivity of the transfer process with respect to the operating conditions, different values of the Reynolds, Damköhler and Schmidt numbers have been considered. These values together with the material and geometrical parameters are given in Section 5.1.1. A grid independence study is reported in Section 5.1.2. In Section 5.1.3 the results of the simulations of physisorption are compared to experimental and theoretical correlations. A detailed analysis regarding the mass transfer coefficient and the reaction selectivity is presented in the sections 5.2 and 5.3. The effects due to a decrease of the diffusion coefficient of the gaseous component are highlighted in Section 5.4. Finally, the simulation results are compared to the film theory predictions in Section 5.5. Film theory is usually adopted to model small-scale phenomena in large-scale simulations of bubble column reactors. Therefore, the comparison allows to assess the accuracy level of this simplified model.

## 5.1 Simulations

### 5.1.1 Parameter space

All the computations have been performed with a constant Morton number equal to 1e−08 given by the density, viscosity and surface tension values reported in Table 5.1. The values of the material parameters of the two phases can be considered to be representative of an air bubble in a glycol-water mixture. Five different bubble diameters have been considered. The resulting Eötvös and bubble Reynolds numbers range from 0.3 to 2 and from 58 to 232, respectively. Fig. 5.1 shows the simulated

points on the chosen iso-Morton line in the well-known diagram of Clift et al. (1978).

The size variations induce drastic changes regarding the bubble deformation and the wake structure. The increase of Eo from 0.3 up to 1 leads to a shape variation from nearly spherical to ellipsoidal with an aspect ratio around 1.6. The wakes of these bubbles are closed and the interface deformation is not strong enough to create recirculations in the rear region. Steady vortical structures appear behind the bubble with a further increase of Eo up to 1.5. At the same time, the aspect ratio rises almost to 2. For the case Eo=2, an unsteady hydrodynamics is observed. The bubble does not rise straight anymore and its trajectory becomes helical. The wake shows unsteadiness as well due to vortices created at the interface and, then, convected and dissipated downstream.

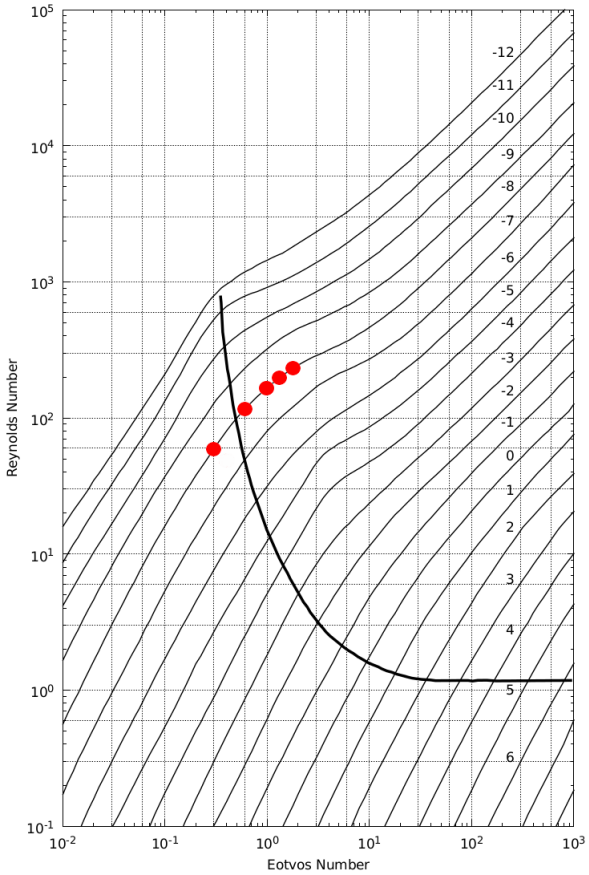


Figure 5.1: Simulated points in the diagram by Clift et al. (1978).

Fig. 5.2 shows the streamlines in the vicinity of the bubble together with a full 3D representation of the interface for each value of the Eötvös number. In the first four pictures, the flow fields exhibit azimuthal symmetry. The last picture shows the symmetry breakup and, accordingly, a deviation of the rising direction due to unsteady effects. Another very important aspect of Fig. 5.2e is the winding of the streamlines which differently from the other cases do not go straight downstream but are intertwined with each other producing 3D vortical structures.

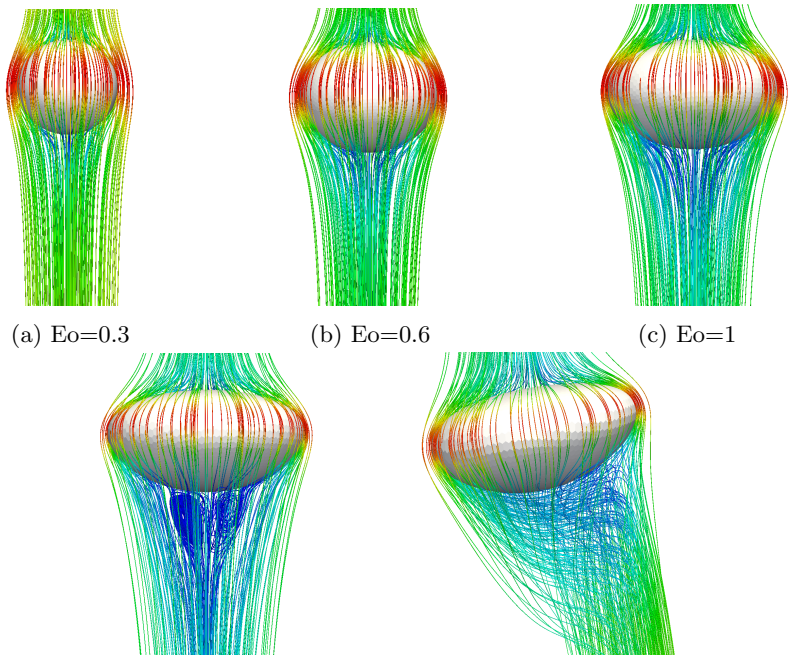

(a) Eo=0.3 (b) Eo=0.6 (c) Eo=1

(d) Eo=1.5 (e) Eo=2

Figure 5.2: Flow streamlines and 3D bubble surface for each value of the Eötvös number.

For each diameter, eight reactive simulations of a competitive-consecutive mechanism (cf. Eq. (3.12)) have been carried out. The chemical reaction coefficients have been varied according to different values for the Damköhler number of the first reaction and for the ratio $\kappa$=$\mathrm{Da}_2/\mathrm{Da}_1$. $\mathrm{Da}_1$ has been chosen equal to 0.01, 0.1, 1 and 10, while $\kappa$ has been set to 10 and 100. These ranges cover a wide spectrum of relevant reaction intensities. Due to the presence of the bubble rise velocity in the Damköhler number, preliminary simulations of the different flow fields have been required in order to obtain the corresponding $U_b$ terms. As for the reference concentration $c_{A,\infty}$ of Eq. (3.19), the inlet value $c_{A,\mathrm{in}}$ of the species $A$ has been used. The concentration $c_{A,\mathrm{in}}$ has been assumed equal to 8.72 mol/m$^3$. Furthermore, simulations of the single reaction prototype for the different values of $\mathrm{Da}_1$ reported above as well as of physisorption have been performed for each bubble size.

The species diffusivity in the liquid phase has been fixed to 1e−07 m$^2$/s for the components $A$, $P$ and $S$, while for the species $B$ it has been set to 4.46e−07 m$^2$/s. The corresponding Schmidt number $\mathrm{Sc}_B$ is equal to 10. Each simulation has been then repeated with $\mathrm{Sc}_B$=100. The results for the larger $\mathrm{Sc}_B$ are reported in Section 5.4. The diffusivity in the gas phase for $B$ has been set to 4.46e−04 m$^2$/s. The resulting values of the ratio $D_{B,g}/D_{B,l}$ are equal to 1000 and 10000 for $\mathrm{Sc}_B$ of 10 and 100, respectively. These values are representative of liquid-side controlled mass transfer processes as found in bubble column reactors. The species $A$ and $B$ have been initialized to 8.72 mol/m$^3$ in the liquid and gas phases, respectively.

For the sake of comparison, all the quantities of interest obtained from the simulations have been sampled at a reference time equal to $35d_b/U_b$, where the ratio $d_b/U_b$ defines a characteristic time scale.

Table 5.1: Values of the material and geometric parameters.

| Parameter | Value and Unit |
|---|---|
| $\mu_l$ | 4.46e−03 $\frac{\text{kg}}{\text{ms}}$ |
| $\rho_l$ | 1000 $\frac{\text{kg}}{\text{m}^3}$ |
| $\mu_g$ | 1.81e−05 $\frac{\text{kg}}{\text{ms}}$ |
| $\rho_g$ | 1.205 $\frac{\text{kg}}{\text{m}^3}$ |
| $\sigma$ | 0.073 $\frac{\text{kg}}{\text{s}^2}$ |
| $d_b$ | 1.49, 2.11, 2.73, 3.34, 3.86 mm |
| $D_{A,l}, D_{P,l}, D_{S,l}$ | 1e−07 $\frac{\text{m}^2}{\text{s}}$ |
| $D_{B,l}$ | 4.46e−07, 4.46e−08 $\frac{\text{m}^2}{\text{s}}$ |
| $D_{B,g}$ | 4.46e−04 $\frac{\text{m}^2}{\text{s}}$ |

Table 5.2: Values of the dimensionless numbers.

| Dimensionless number | Value |
|---|---|
| Mo | 1e−08 |
| Eo | 0.3, 0.6, 1, 1.5, 2 |
| $\text{Re}_b$ | 58, 118, 173, 219, 232 |
| $\text{Da}_1$ | 0.01, 0.1, 1, 10 |
| $\kappa$ | 10, 100 |
| $\text{Sc}_A$, $\text{Sc}_P$, $\text{Sc}_S$ | 44.6 |
| $\text{Sc}_B$ | 10, 100 |
| $\text{H}_B$ | 30 |

### 5.1.2 Mesh convergence

All the simulations have been performed with the same hydrodynamic and species transfer meshes scaled according to the considered bubble diameter. The overall number of computational cells of the mesh used for the hydrodynamic problem is about 400000. Three refinement levels have been applied to generate the grid for the species transport equations, resulting in approximately 420000 cells. In every refinement step each cell adjacent to the interface has been split along the normal direction into two almost identical parts, producing an interfacial layer height equal to 1/8 of its counterpart in the hydrodynamic mesh.

The number of refinements has resulted from a grid independence study. The analysis has been performed on the most demanding case of the computational campaign with $\text{Sc}_B$=100, Eo=1.5 and the reaction coefficients given by $\text{Da}_1$=10 and $\kappa$=100. Five different meshes have been considered with

Table 5.3: Grid independence results.

| No. refinements | Global Sherwood |
|---|---|
| 0 | 466.21 |
| 1 | 563.09 |
| 2 | 592.81 |
| 3 | 598.46 |
| 4 | 599.03 |

zero to four refinement levels.

Table 5.3 shows the Sherwood values for the five different cases at a sampling time equal to 0.2 s. It emerges clearly the need for a grid finer than that one used for the hydrodynamic problem which leads to a poor prediction of the species transfer. The relative deviation between the last two values is about 0.1%, allowing to conclude that three refinements are sufficient to resolve the smallest scales occurring in the simulation set.

### 5.1.3 Comparison to correlations

The Sherwood numbers resulting from the simulations of physisorption have been compared to the predictions of the theoretical correlations by Lochiel and Calderbank (1964) and Winnikow (1967). Lochiel and Calderbank assumed a potential flow around an oblate spheroidal bubble with axisymmetric condition. Under these circumstances, the Sherwood number in the case of physisorption is

$$\mathrm{Sh} = \frac{2}{\sqrt{\pi}}\mathrm{Pe}_k^{1/2}\left[\frac{8a^{1/3}E^3}{3(\sin^{-1}E - aE)}\right]/\left[1 + \frac{a^2}{2E}\ln\left(\frac{1+E}{1-E}\right)\right], \tag{5.1}$$

where $a$ is the aspect ratio of the spheroid given by the ratio between the semi-minor and semi-major axes and $E{=}(1-a^2)^{1/2}$ is the eccentricity.

The expression of Winnikow relies on the boundary layer theory. Considering a spherical bubble with axisymmetric condition, Winnikow has obtained again for the case of physisorption the following result for Sh,

$$\mathrm{Sh} = \frac{2}{\sqrt{\pi}}\left(1 - \frac{2.89}{\mathrm{Re}_b^{1/2}}\right)\mathrm{Pe}_k^{1/2}. \tag{5.2}$$

The simulation results have been also compared to the experimental correlation of Takemura and Yabe (Eq. (4.80)). The values of the equivalent Sherwood number provided by Eq. (4.80) have been corrected with the area strech factors in Table 5.4.

Although the validity ranges of Eqs. (5.1), (5.2) and (4.80) do not include all the Reynolds numbers considered in this work, these correlations represent an important term of comparison for the numerical results. Significant deviations from their values might indicate an insufficient accuracy of the numerical

method. An analogous comparison for the chemisorption results was not possible due to the lack of reference correlations.

Despite the unsteady hydrodynamic condition, the Sherwood number corresponding to the largest bubble diameter reaches a steady value. As visible in Fig. 5.3, the perturbations induced by the unsteadinesses on the mass transfer are negligible. Therefore, it is possible to take the value of the Sherwood number at the end of the simulation without the necessity of averaging over a representative time period.

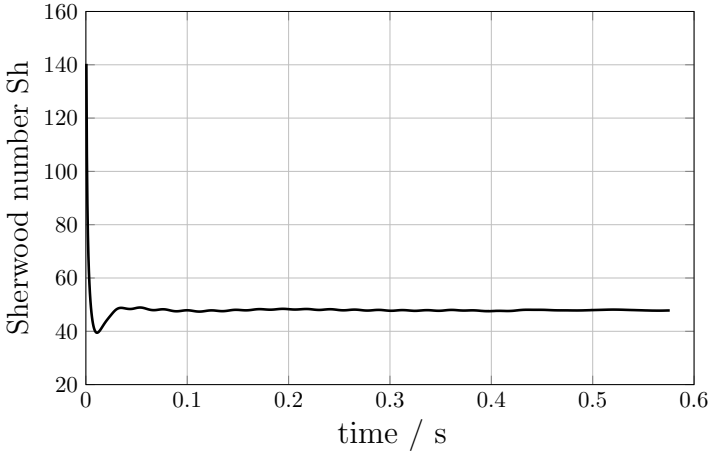


Figure 5.3: Sherwood number over time of the simulation of physisorption, $\mathrm{Re}_b$=232.

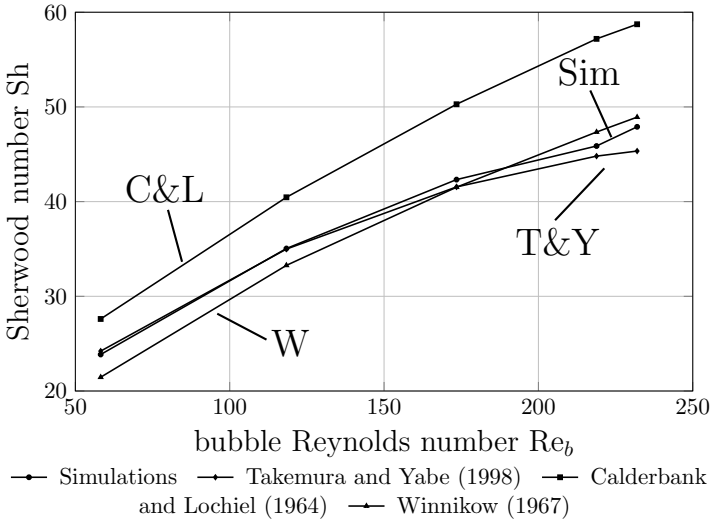


Figure 5.4: Sherwood number as function of the bubble Reynolds number for physisorption, $\mathrm{Sc}_B$=10.

Fig. 5.4 shows that the simulation results are in good agreement with the correlation of Takemura and Yabe for Reynolds numbers less than 150. From this point on, the two curves start to diverge with a maximum relative deviation about 5% at $\mathrm{Re}_b$=232. The discrepancy can be ascribed to the

limited validity range of the experimental formula up to $\mathrm{Re}_b$ equal to 100. The bubbles remain mainly spherical in this range. Therefore, the correlation does not contain the effects of higher bubble surface deformations on the mass transfer.

Larger differences emerge from the comparison with the theoretical work of Lochiel and Calderbank. The drastic assumption of potential flow results in an overestimation of the Sherwood number with a maximum relative deviation about 22% at the largest Reynolds number. On the contrary, the agreement with the boundary layer solution of Winnikow improves as the Reynolds number increases. The corresponding values at $\mathrm{Re}_b$=232 differ by approximately 2%.

The analogous comparison for Schmidt number equal to 100 is reported in Fig. 5.5. The situation depicted in this figure is nearly identical to that one of Fig. 5.4 with similar relative deviations between the simulations and the correlations. Therefore, the above comments relating to the case of Schmidt number equal to 10 are valid here, too.

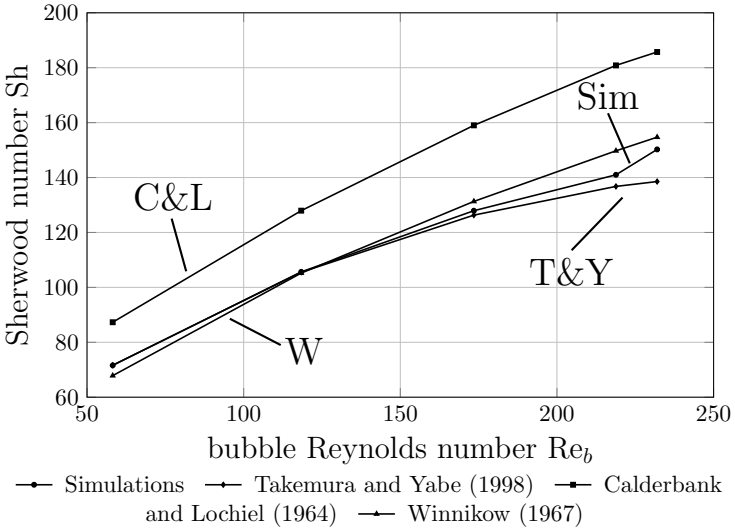


Figure 5.5: Sherwood number as function of the bubble Reynolds number for physisorption, $\mathrm{Sc}_B$=100.

## 5.2 Species transfer

If it is assumed that all the bubbles in the reactor have similar size and behavior, the overall molar transfer rate $\dot{n}$ can be approximated as

$$\dot{n} = \beta_l A_b N_b \bar{c}_{B,l}, \tag{5.3}$$

where the product of the bubble area $A_b$ and the number of bubbles in the reactor $N_b$ gives the total interfacial area $A_i$ between the liquid and gas phases. The total interfacial area can be rewritten as

$$A_i = A_b N_b = A_b \frac{V\epsilon_g}{V_b} = V\epsilon_g \frac{A_{b,\mathrm{eq}}\chi}{V_b} \approx 4.84\, V\epsilon_g \frac{\chi}{V_b^{1/3}}, \tag{5.4}$$

where $V$ is the volume of the reactor, $\epsilon_g$ is the void fraction, $V_b$ is the bubble volume and $\chi$ denotes the area strech factor, i.e. the ratio $A_b/A_{b,\mathrm{eq}}$. If the reactor volume $V$ and the void fraction $\epsilon_g$ are considered fixed, the amount of interfacial area available for the mass transfer depends on the ratio $\chi/V_b^{1/3}$. The values of $\chi/V_b^{1/3}$ obtained from the geometrical information reported in Table 5.4 for the different hydrodynamic conditions are shown in Fig. 5.6. It emerges that the adoption of smaller bubbles leads to a significantly larger interfacial area. More precisely, at fixed void fraction and reactor volume, the contact area between the two phases for $d_b$=1.49 mm is around 2.3 times larger than that one for $d_b$=3.86 mm.

Table 5.4: Simulations results - bubble geometry.

| $d_b$/m | $A_b$/m$^2$ | $A_{b,\mathrm{eq}}$/m$^2$ | $\chi/-$ | $V_b$/m$^3$ |
|---|---|---|---|---|
| 1.49e−03 | 7.018e−06 | 7.018e−06 | 1 | 1.745e−09 |
| 2.11e−03 | 1.418e−05 | 1.404e−05 | 1.009 | 4.937e−09 |
| 2.73e−03 | 2.438e−05 | 2.341e−05 | 1.042 | 1.062e−08 |
| 3.34e−03 | 3.837e−05 | 3.511e−05 | 1.093 | 1.952e−08 |
| 3.86e−03 | 5.214e−05 | 4.681e−05 | 1.114 | 3.003e−08 |

Table 5.5: Simulation results - contact times.

| $d_b$/m | $U_b$/m s$^{-1}$ | $\tau_{\mathrm{hyd}}$/s |
|---|---|---|
| 1.49e−03 | 0.174 | 8.603e−03 |
| 2.11e−03 | 0.25 | 8.46e−03 |
| 2.73e−03 | 0.284 | 9.621e−03 |
| 3.34e−03 | 0.292 | 1.144e−02 |
| 3.86e−03 | 0.268 | 1.439e−02 |

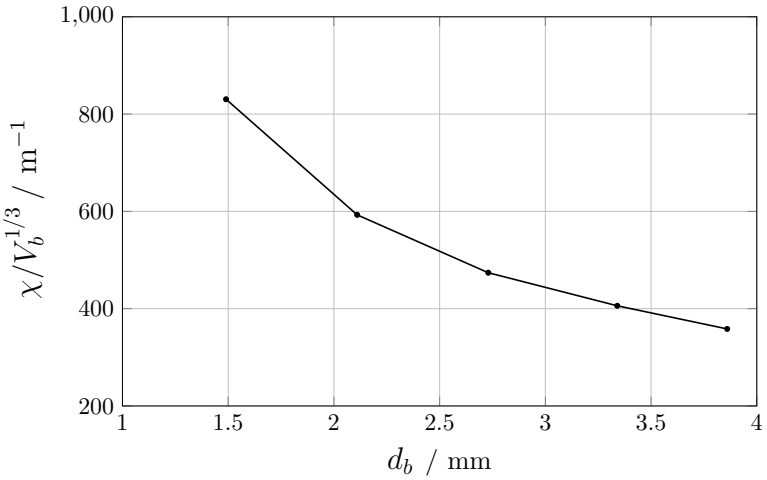


Figure 5.6: Factor $\chi/V_b^{1/3}$ as function of the bubble diameter.

As resulting from Eq. (5.3), the other quantity affecting the overall species transfer is the transfer coefficient $\beta_l$ (see Eq. (3.23)). The dependence of $\beta_l$ from the Reynolds number, i.e. the bubble diameter, has been analysed in the case of physisorption. As visible in Fig. 5.7, the mass transfer coefficient exhibits a non-monotonic profile. A maximum occurs at a bubble diameter equal to 2.11 mm. Starting from this point, a decrease occurs.

Looking at the profiles of the local mass transfer coefficient is enlightening in order to understand the behavior of $\beta_l$ in Fig. 5.7. These profiles along the polar angle $\theta$ for the different bubble diameters are reported in Fig. 5.8. The largest diameter with unsteady hydrodynamic conditions is not shown due to the lack of symmetry with respect to the azimuthal angle.

Lower $\beta_{l,loc}$ values correspond to larger bubbles in the region I of Fig. 5.8. This can be ascribed to the longer residence times due to the increasing flattening of the interface at the top of the bubble. An increase of the mass transfer coefficient is visible in the vicinity of the equatorial line (region II) for the third and fourth diameter. The high deformations of the large bubbles cause in this region high tangential velocities responsible for the thinning of the concentration boundary layer. However, large interface deformations have two main counter-effects which determine the rapid decrease of $\beta_l$ in Fig. 5.7. The first one concerns the contact time $\tau_{\mathrm{hyd}}$ experienced by a fluid particle flowing around the bubble. As a rough estimate, the contact time can be assumed proportional to the ratio $d_b/U_b$. The values of $d_b/U_b$ for the different bubble sizes are reported in Table 5.5 and shown in Fig. 5.9. The value of $U_b$ for the largest diameter has been obtained by averaging over a representative time period the time-dependent rising velocity after the initial transient. As emerges from Table 5.5, the increase of the diameter is not sufficiently compensated by the increase of the rising velocity, resulting into a longer contact time and, therefore, a less effective refreshment of the concentration boundary layer by the fluid flow for large bubbles.

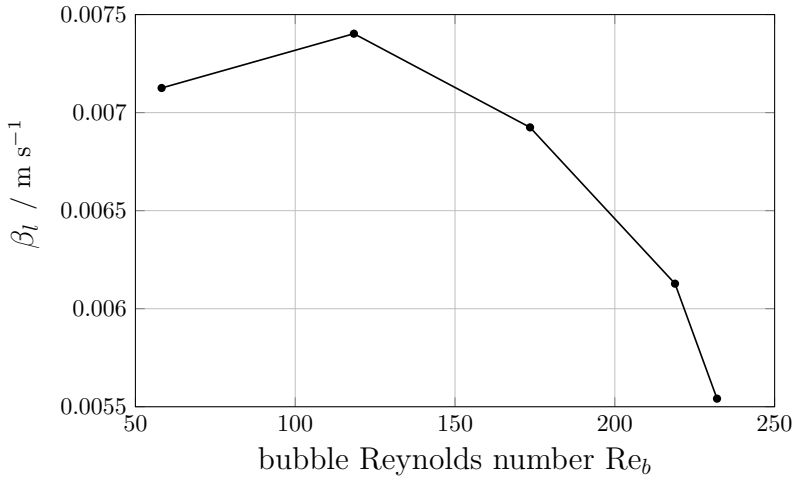


Figure 5.7: Mass transfer coefficient as function of the bubble Reynolds number for physisorption.

The second counter-effect relates to the appearance of recirculations in the rear of the bubble. The advective exchange between this region and the rest of the liquid is completely suppressed due to the closed streamlines. Therefore, only diffusion can transport the species $B$ out of this region. Furthermore, the presence of vortices generates a stagnation line which additionally hinders the species transfer upstream. Both these two aspects contribute to the drastic decrease of the local mass transfer coefficient for $d_b$=3.34 mm. The corresponding profile in Fig. 5.8 lies below the other curves almost for all polar angles.

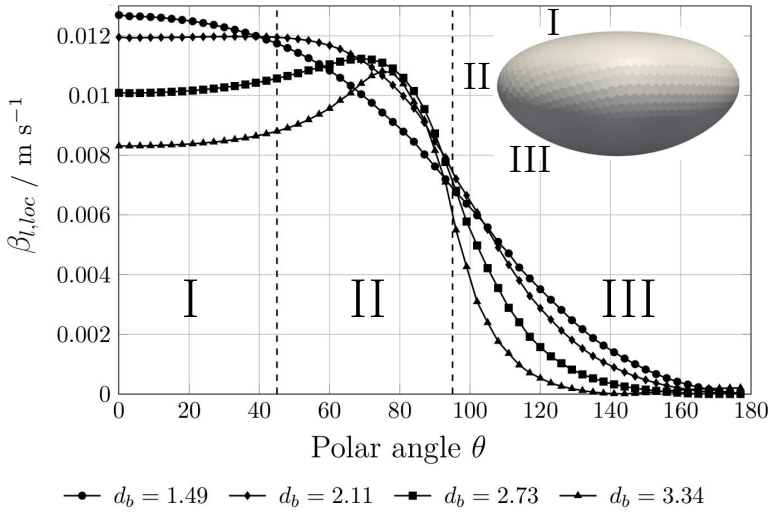


Figure 5.8: Local mass transfer coefficient as function of the polar angle for physisorption, a representation of the different polar sectors along the interface is at the top-right corner of the figure.

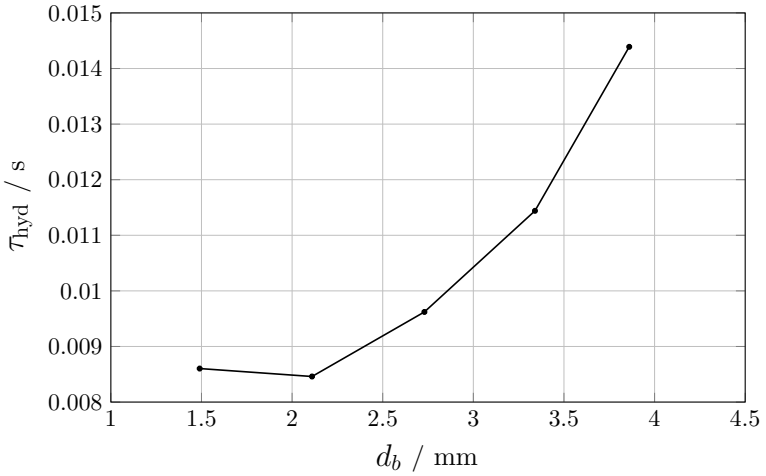


Figure 5.9: Contact times as function of the bubble diameter.

With regard to the results of chemisorption, the plots of the enhancement factor as function of the bubble Reynolds number at different Damköhler values have been reported in Fig. 5.10 for the single reaction and competitive-consecutive prototypes, respectively. Besides the trivial observation that larger Damköhler numbers, i.e. higher reaction rates, lead to higher enhancement factors, it can be noted that the dependence of E from the bubble Reynolds number is weak for both the reaction prototypes. In fact, the different isolines in Fig. 5.10a present small relative deviations between their minimum and maximum values. The largest deviation is approximately 6% for $Da_1$=10. In both Figs. 5.10b and 5.10c, it is instead about 5.5% for $Da_1$=1. Therefore, the plot of the mass transfer coefficients of the chemisorption would provide profiles similar to the physisorption curve in Fig. 5.7.

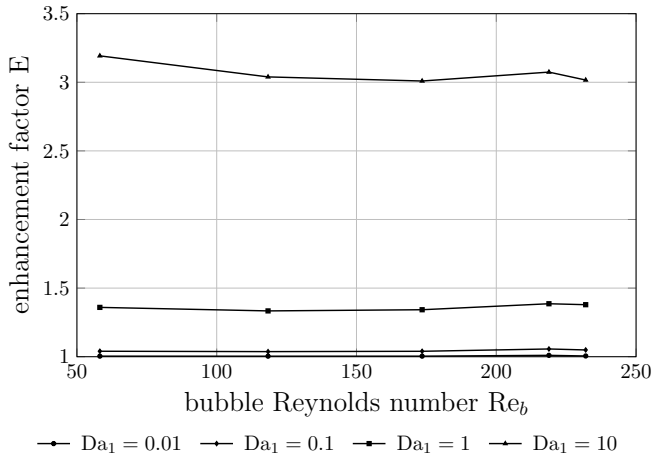


(a) single reaction prototype

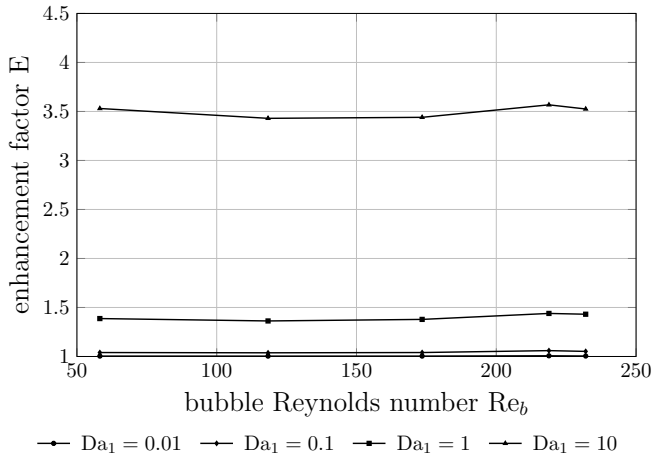


(b) competitive-consecutive prototype with $\kappa$=10

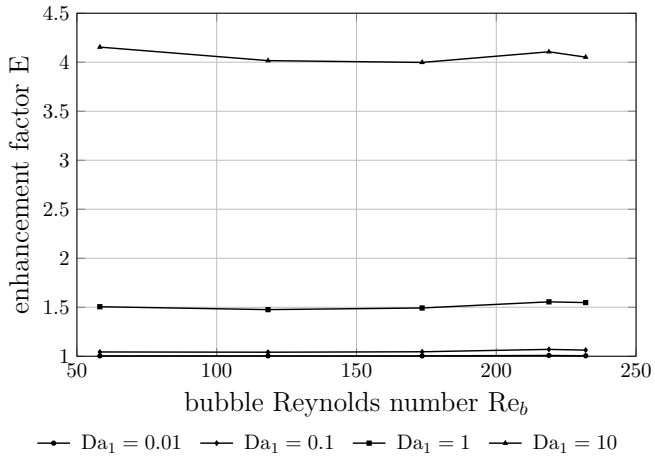


(c) competitive-consecutive prototype with $\kappa$=100

Figure 5.10: Enhancement factor as function of the bubble Reynolds number at different Damköhler values for the single reaction and competitive-consecutive reaction prototypes.

Further insights can be gained by looking again at the local profiles. In Fig. 5.11 the local mass transfer coefficient has been plotted against the polar angle for the different bubble diameters in the cases of single reaction and competitive-consecutive prototypes with $\mathrm{Da}_1$=1 and $\kappa$=10. A similarity between the different plots with or without chemical reactions is clearly visible by comparing Figs. 5.8 and 5.11. Some differences appear only at the rear of the bubble. Contrary to Fig. 5.8, the profiles in Fig. 5.11 exhibit an increasing local mass transfer coefficient for large polar angles. The deceleration of the liquid and, consequently, the higher concentrations of the gas component intensify the chemical reactions in this region, enhancing the refreshing of the boundary layer. This argument becomes even more evident for a bubble diameter of 3.34 mm due to the presence of the recirculating vortices. However, the interfacial area affected by this intense enhancement of the species transfer is only a small part of the total bubble surface (cf. Fig. 5.12) with a limited contribution to the overall enhancement.

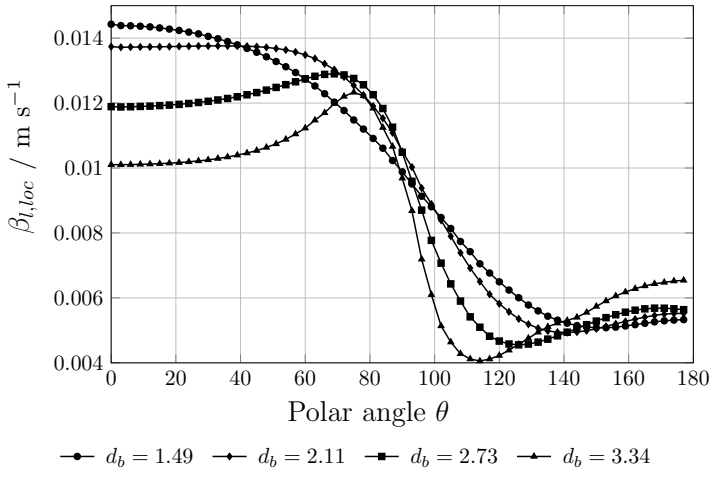


(a) single reaction prototype

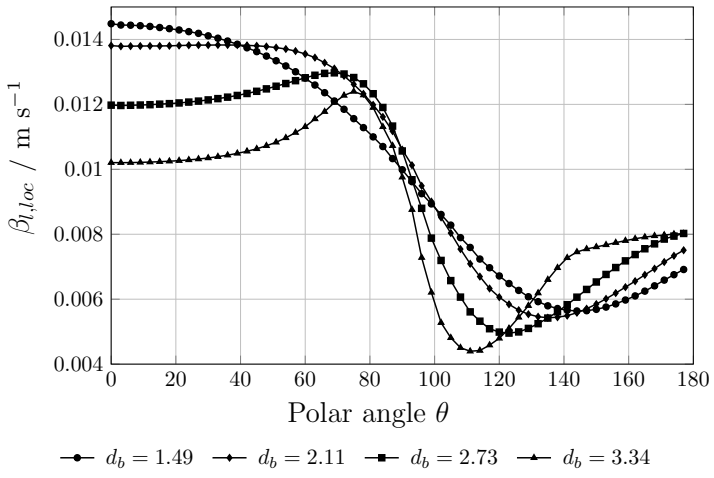


(b) competitive-consecutive prototype

Figure 5.11: Local mass transfer coefficient as function of the polar angle for single reaction and competitive-consecutive prototypes, $\mathrm{Da}_1$=1 and $\kappa$=10.

Another important aspect of Fig. 5.11 regards the discrepancies between the local profiles of Figs. 5.11a and 5.11b at large polar angles. In this region, the species $P$ produced by the first reaction is hardly drained away by the poor advective transport and, thus, it can react with $B$ yielding the undesired component $S$. As will be more deeply examined in Section 5.3, this phenomenon causes a drop of the global selectivity, particularly significant in the case of steady recirculations. However, the presence of the side reaction determines an increase of the mass transfer coefficient since it also consumes the dissolved reactant $B$.

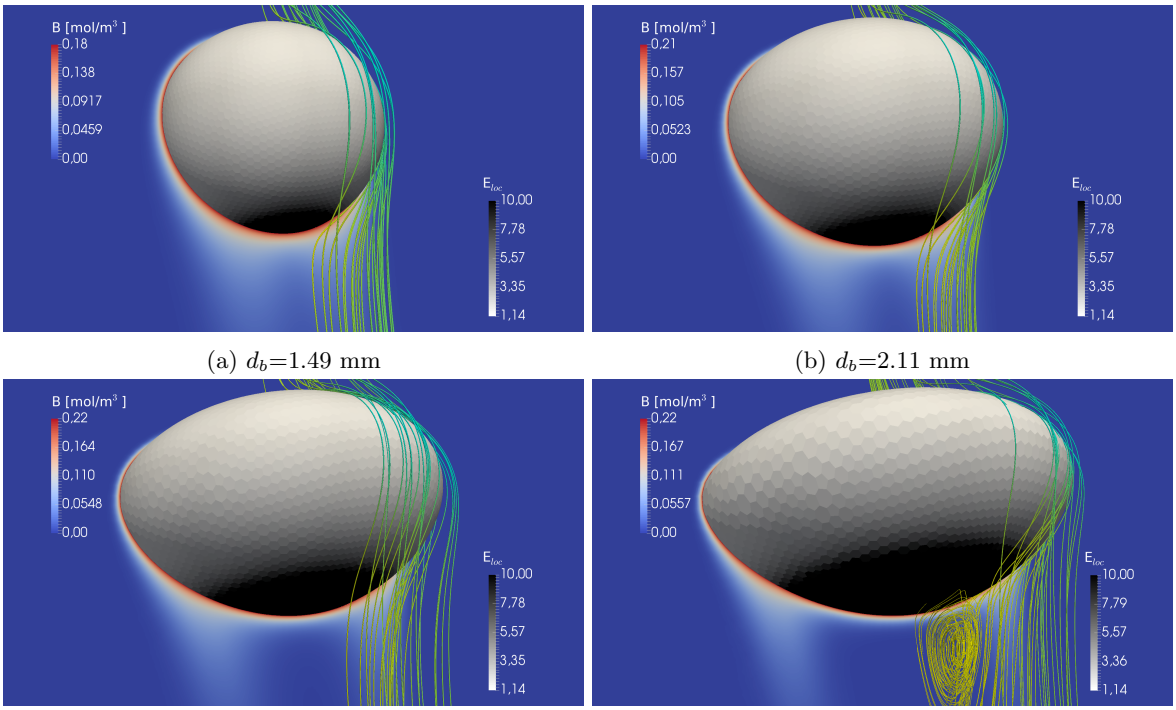


(a) $d_b$=1.49 mm (b) $d_b$=2.11 mm

(c) $d_b$=2.73 mm (d) $d_b$=3.34 mm

Figure 5.12: Local enhancement factor fields for the competitive-consecutive reaction prototype with $Da_1$=1 and $\kappa$=10 for different bubble diameters, each figure also includes the concentration field of the species $B$ and streamlines.

## 5.3 Reaction selectivity

In addition to the mass transfer coefficient, the other important quantity in the context of reactive mass transfer processes is the reaction selectivity (see Eq. (3.25)). Khinast (2001) has investigated the impact of different hydrodynamic conditions and chemical reaction intensities on the selectivity of the competitive-consecutive reaction prototype considered in this work by means of a 2D cylindrical fixed-bubble model. The aspect ratio of the bubbles was fixed to 1, 0.5 and 0.25 respectively, while the Damköhler was set to 0.01, 0.1 and 1 with values for $\kappa$ of 1, 20 and 500. The Schmidt numbers of the different species are comparable to those ones assumed in the present study. The outcomes of his

simplified model have shown three main aspects regarding the behavior of the selectivity. At a given $\kappa$, this quantity exhibits higher values for smaller $\mathrm{Da}_1$. It increases monotonically with the Reynolds numbers for nearly spherical bubbles. In the more ellipsoidal cases, the onset of recirculating vortices determines a selectivity drop due to the complete lack of advective transport between the rear of the bubble and the rest of the fluid domain. This leads to a progressive depletion of the liquid component $A$ and, thus, to a preferential reactivity of the dissolved gas with the product $P$. The selectivity value starts to rise again with a further increment of the Reynolds causing the transition from the closed to the open wake structure. The final result is a non monotone $S - \mathrm{Re}_b$ curve for ellipsoidal bubbles.

Fig. 5.13 shows the $S - \mathrm{Re}_b$ profiles coming from the numerical simulations for all the $\mathrm{Da}_1$ values at $\kappa$=10. This figure depicts a qualitatively different situation in comparison to the plots presented by Khinast. The general tendency to have higher selectivities with increasing Reynolds number is not present in the current analysis. On the contrary, a slow reduction can be observed as the Reynolds number becomes larger for moderate and fast reactions, i.e. Damköhler number equal to 1 and 10, respectively.

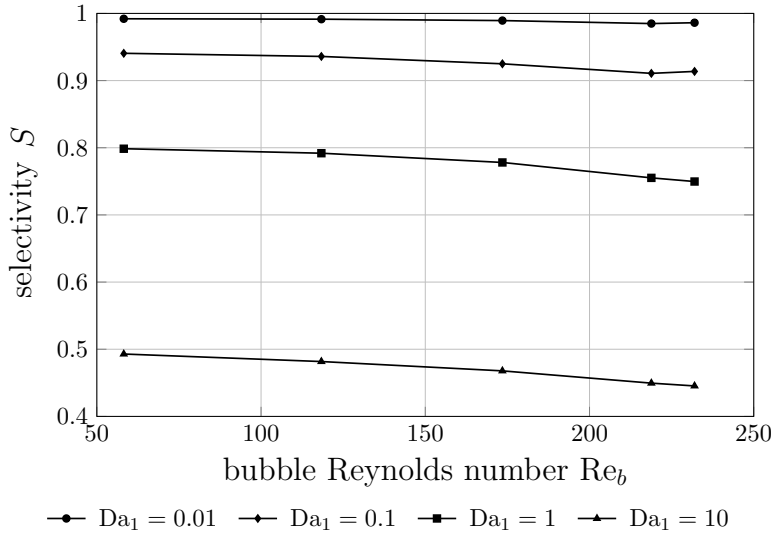


Figure 5.13: Selectivity as function of the bubble Reynolds number at different Damköhler values for the competitive-consecutive prototype, $\kappa$=10.

Focusing on the two cases addressed in Fig. 5.14, it is possible to ascribe the above mentioned behavior to the combination of unsteady and 3D effects. For the largest bubble, the breakup of the azimuthal symmetry implies that the fluid particles flowing around the bubble at one side of the interface experience a longer contact time in comparison to the fluid particles flowing at the other side. Furthermore, the presence of vortical structures developing perpendicularly to the cutting plane in Fig. 5.14, which can be captured solely by 3D simulations, additionally prolongs the residence time of these particles in the vicinity of the bubble surface. This region is characterized by a high concentration of the dissolved component which can react intensively with the product of the first reaction, leading to the creation of a significant amount of the side-product. This mechanism is confirmed by

the concentration and reaction rate fields in Fig. 5.15. The final result is an enlargement of the low-selectivity area for $d_b$=3.86 mm, as visible by comparing Figs. 5.14a and 5.14b.

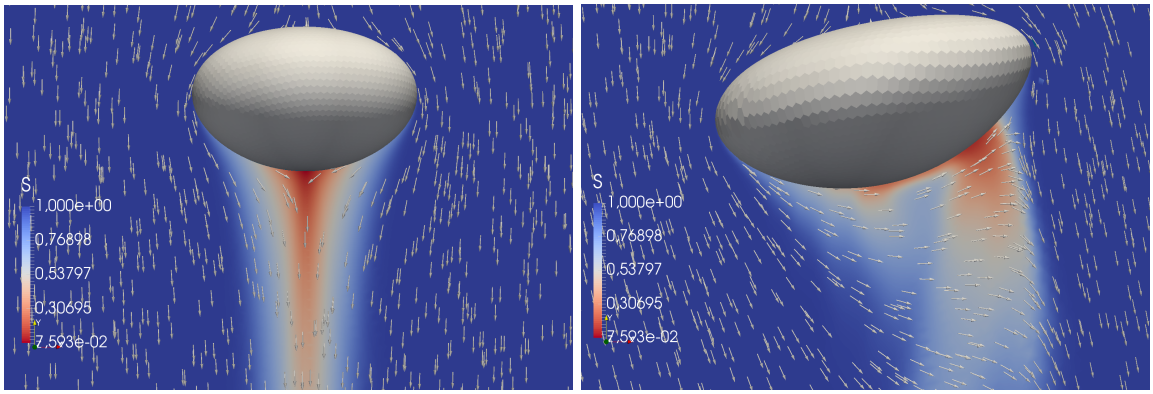


(a) $d_b = 2.73$ mm (b) $d_b = 3.86$ mm

Figure 5.14: Local selectivity fields of the competitive-consecutive prototype with $\mathrm{Da}_1$=1 and $\kappa$=10 for two different bubble diameters, each figure includes the projections of the velocity vectors on the cutting plane.

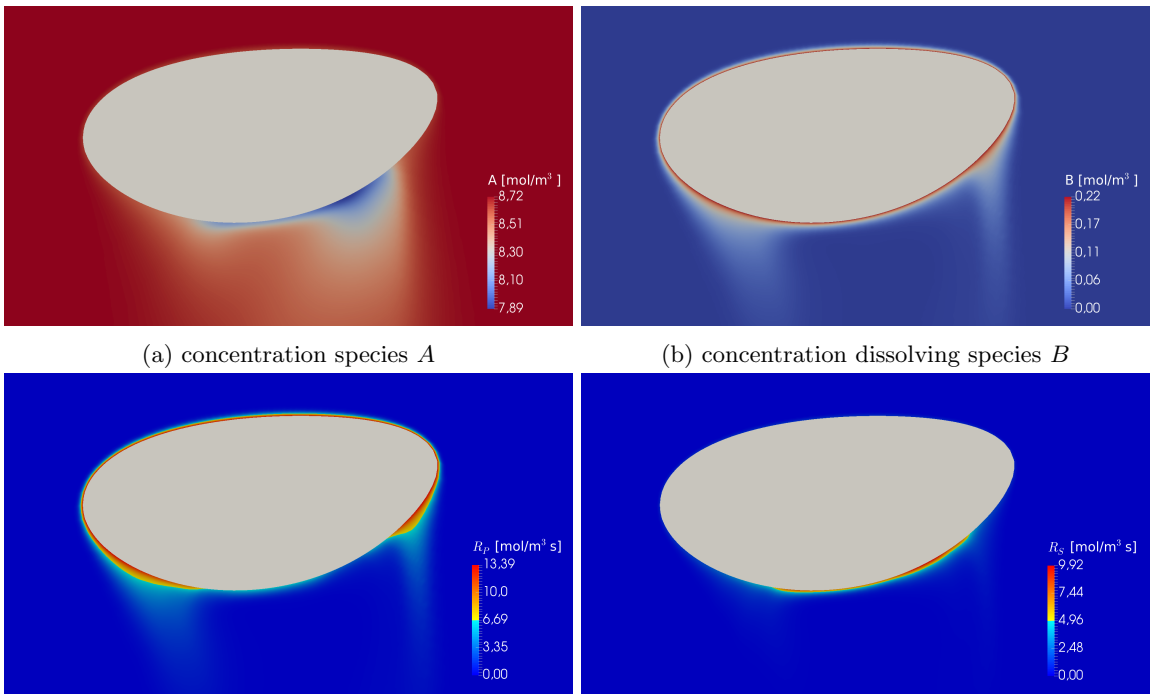


(a) concentration species $A$ (b) concentration dissolving species $B$

(c) reaction rate product $P$ (d) reaction rate side-product $S$

Figure 5.15: Concentration and reaction rate fields of the competitive-consecutive reaction prototype with $\mathrm{Da}_1$=1 and $\kappa$=10 for a bubble diameter $d_b$=3.86 mm.

In the case of slow reactions ($\mathrm{Da}_1$=0.01, 0.1), it can still be noted that the steady vortices produce a selectivity value slightly smaller than that one relating to the unsteady bubble. The same phenomenon is also visible in Fig. 5.16, which shows the $S - \mathrm{Re}_b$ profiles for $\kappa$=100. For slow reactions, the concentration boundary layers of the dissolving species become thicker. Accordingly, they penetrate more deeply into the recirculating vortices intensifying the selectivity drop due to the complete lack of advective transport between this region and the rest of the liquid domain, as already pointed out by Khinast in the 2D case and confirmed here for 3D bubbles.

The increase of the second reaction rate causes obviously a significant lowering of all the selectivity values, as visible by comparing Figs. 5.13 and 5.16. Furthermore, as emerges from the two curves with higher $\mathrm{Da}_1$ in Fig. 5.16, this quantity becomes almost independent from the Reynolds numbers for fast reactions. Under these circumstances, the reaction zone is very small and, thus, it is not noticeably affected by the different hydrodynamic conditions.

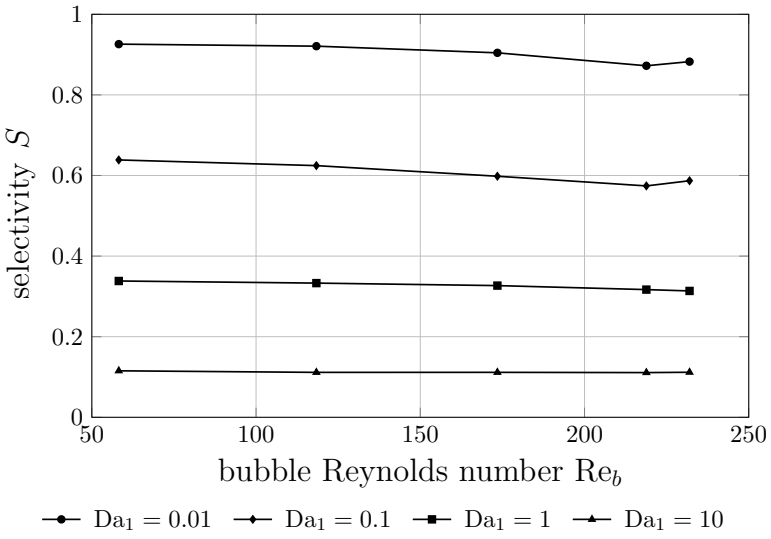


Figure 5.16: Selectivity as function of the bubble Reynolds number at different Damköhler values for the competitive-consecutive reaction prototype with $\kappa$=100.

## 5.4 Higher Schmidt number cases

In industrial applications, the diffusivity of the gaseous component in the liquid phase is usually small and, thus, the thickness of the concentration boundary layers can reach the dimension of a few micrometers. Therefore, it is fundamental to assess the impact of high Schmidt numbers on the reactive mass transfer processes. In the following, the results of the simulations with $\mathrm{Sc}_B$=100 are presented and compared to those reported in the previous two sections relating to the case of $\mathrm{Sc}_B$=10. Realistic diffusion coefficients, as found in bubble column reactors, correspond to Schmidt numbers at least one order of magnitude larger, i.e. $\mathrm{Sc}_B \geq 1000$. Such high values of this nondimensional number require a numerical resolution that is not achievable at the moment by the method developed in this

work. Further refinements of the interfacial cell layers in normal direction would produce too large aspect ratios, compromising the stability of the numerical solution. In order to maintain reasonable aspect ratios and, therefore, preserve the stability, the normal refinements should be accompanied by a decrease of the size of the mesh faces representing the interface. This would result in a significant increase of the overall number of mesh cells, leading to an excessive computational cost. However, the comparison performed in this section already provides important insights regarding the effects of lower diffusion coefficients.

Starting from the analysis of the mass transfer coefficients, it can be observed in Fig. 5.17 that the profile of $\beta_l$ as function of the bubble Reynolds number relating to the physisorption problem is similar to that one presented in Fig. 5.7 for $\mathrm{Sc}_B$=10. Also in this case the behavior of the contact time with respect to $\mathrm{Re}_b$ appears to determine the shape of the mass transfer coefficient curve. However, a quantitative inspection reveals that the relative differences between the maximum and the minimum values of the profiles in Figs. 5.17 and 5.7 are about 28% and 33%, respectively. As a consequence of the thinner concentration boundary layers due to the higher transport resistance in the liquid phase, their interaction with the wake region decreases, leading to a more limited influence of the hydrodynamic conditions on the species transfer processes.

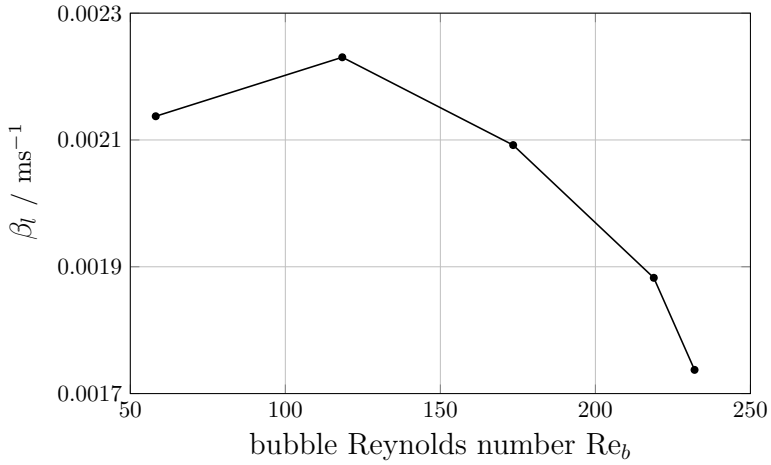


Figure 5.17: Mass transfer coefficient as function of the bubble Reynolds number for physisorption, $\mathrm{Sc}_B = 100$.

Fig. 5.18 shows the enhancement factor values of the competitive-consecutive prototype as function of the bubble Reynolds number at different $\mathrm{Da}_1$. Figs. 5.18a and 5.18b correspond to the cases of $\kappa$ equal to 10 and 100, respectively. The weak dependence of the enhancement factor from $\mathrm{Re}_b$ observed in Fig. 5.10 is also visible here. This is confirmed by computing the relative deviation between the minimum and maximum values for each isoline of Fig. 5.18a. The larger relative deviation is slightly less than 5% at $\mathrm{Da}_1$=1. A similar value is obtained for the profiles in Fig. 5.18b.

In analogy to Figs. 5.13 and 5.16, Fig. 5.19 shows the reaction selectivity of the competitive-consecutive mechanism at the different values of $\mathrm{Da}_1$ and $\kappa$. It is noted that the selectivity values are higher than those relating to the case of $\mathrm{Sc}_B$=10. This general aspect can be explained by inspection

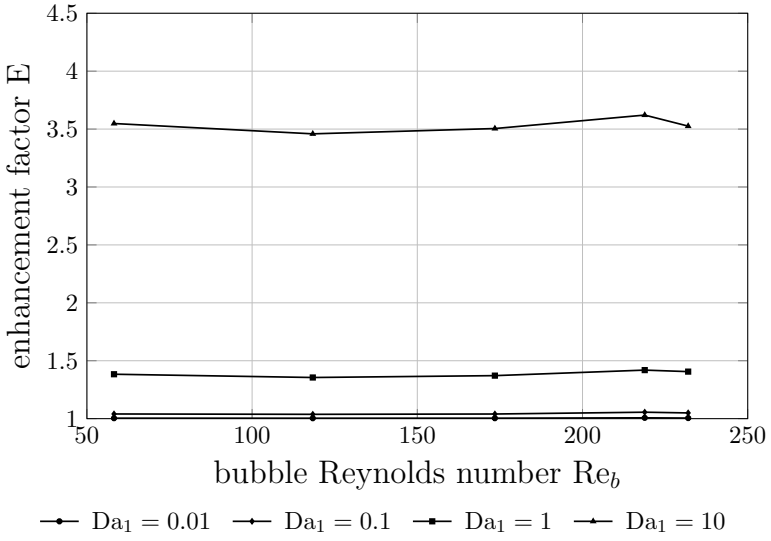


(a) $\kappa$=10

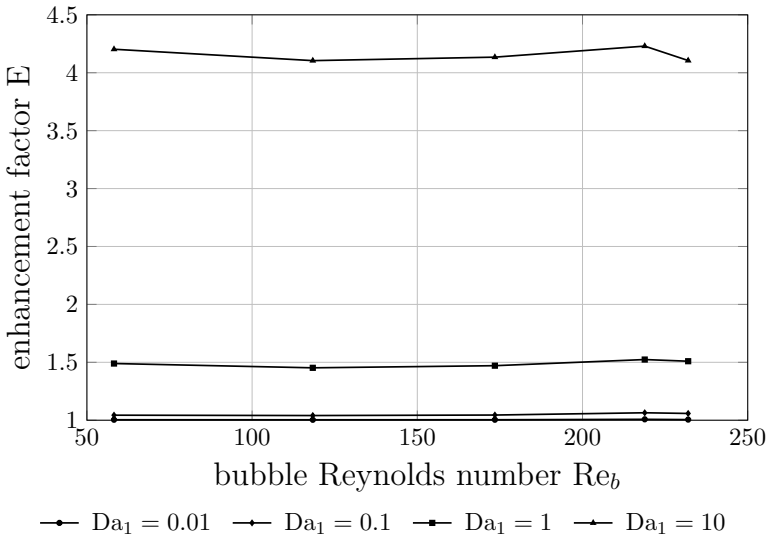


(b) $\kappa$=100

Figure 5.18: Enhancement factor as function of the bubble Reynolds number at different Damköhler values for the competitive-consecutive prototype, $\mathrm{Sc}_B = 100$.

of the local selectivity expression. Substituting the reaction rates of Eq. (3.12) into the local selectivity definition (3.26), this becomes

$$S_{loc}(t,x) = \frac{1-\kappa\frac{c_P}{c_A}}{1+\kappa\frac{c_P}{c_A}}. \tag{5.5}$$

Eq. (5.5) highlights that the decrease of the dissolved component concentration due to the lower diffusivity, which in turn leads to a smaller production of $P$ and a lower consumption of $A$, determines

an increase of the local and, consequently, global selectivities.

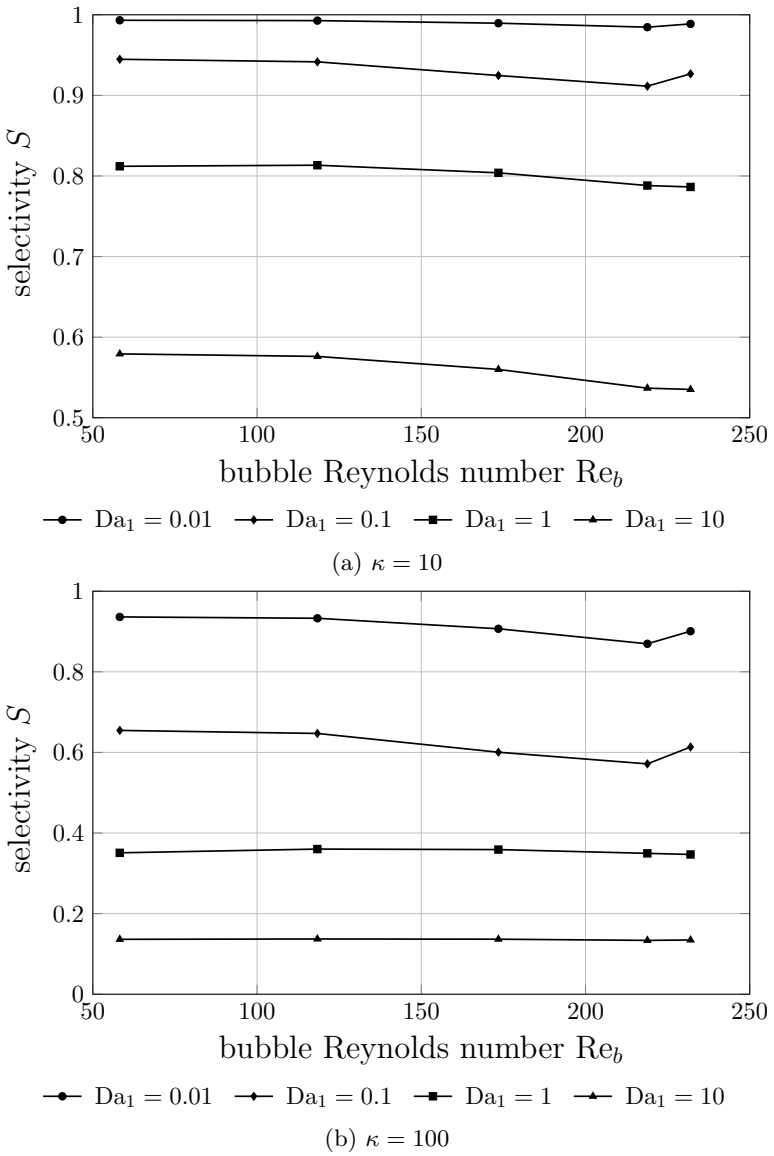


(a) $\kappa = 10$

(b) $\kappa = 100$

Figure 5.19: Selectivity as function of the bubble Reynolds number at different Damköhler values for the competitive-consecutive reaction prototype, $\mathrm{Sc}_B = 100$.

From the qualitative point of view, significant discrepancies between the plots of Figs. 5.19 and 5.13-5.16 are not present. However, more detailed information can be gained from Figs. 5.20 and 5.21. Fig. 5.20 reports the selectivity profiles at $\mathrm{Da}_1$=1 contained in Figs. 5.13 and 5.19a, respectively. Fig. 5.21 shows the profiles corresponding to $\mathrm{Da}_1$=0.1. Fig. 5.20 highlights that the dependence of the reaction selectivity from the Reynolds number is reduced at the larger value of the Schmidt number. In fact, the relative deviation between the minumum and maximum values of the curve corresponding

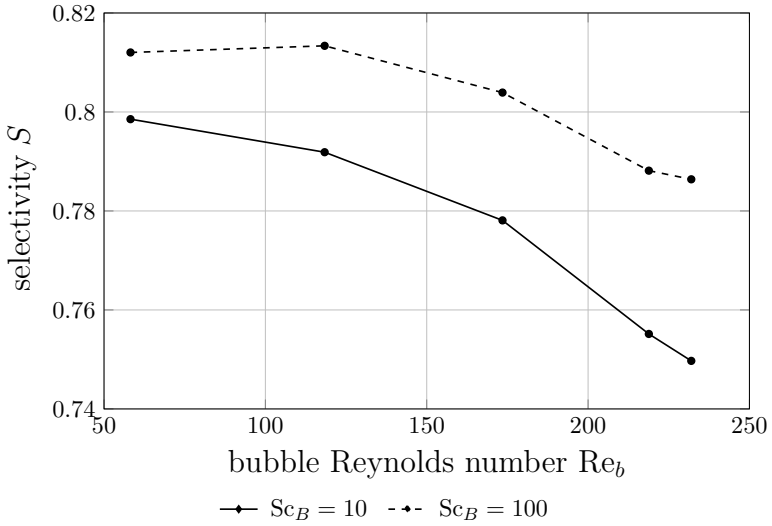


Figure 5.20: Selectivity as function of the bubble Reynolds number for the competitive-consecutive reaction prototype with $\mathrm{Da}_1$=1 and $\kappa$=10.

to the case of $\mathrm{Sc}_B$=10 is approximately 6%, while this drops to about 3% for $\mathrm{Sc}_B$ equal to 100. This behavior can be ascribed to the reduced interaction between the smaller concentration boundary layers due to the higher Schmidt number and the different wake patterns, as already explained for the plot of the mass transfer coefficient in Fig. 5.17.

At first glance, the situation depicted in Fig. 5.20 appears to be reversed in Fig. 5.21. In the latter figure, the relative deviation of the curve for $\mathrm{Sc}_B$=100 is larger than that for $\mathrm{Sc}_B$=10. This results from the fact that the two curves touch each other at $\mathrm{Re}_b$=219 at which both exhibit their minimum

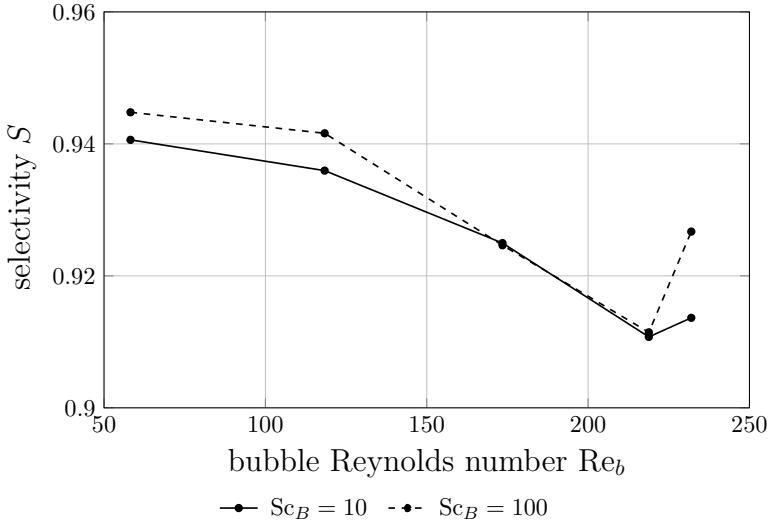


Figure 5.21: Selectivity as function of the bubble Reynolds number for the competitive-consecutive reaction prototype with $\mathrm{Da}_1$=0.1 and $\kappa$=10.

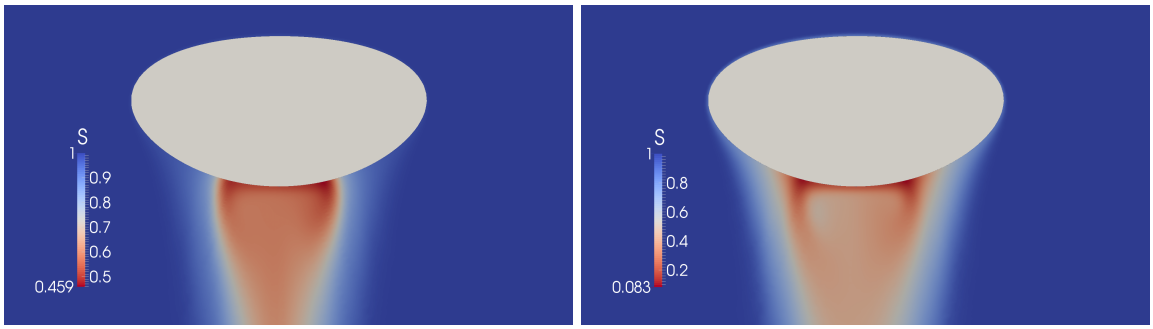


(a) $\mathrm{Da}_1 = 0.1$ (b) $\mathrm{Da}_1 = 1$

Figure 5.22: Local selectivity fields of the competitive-consecutive reaction prototype for two different values of the Damköhler number, $\mathrm{Re}_b = 219$ and $\kappa = 10$.

value. The independence of the selectivity from $\mathrm{Sc}_B$ at $\mathrm{Re}_b$=219 can be understood by looking at the local field shown in Fig.5.22a. It can be seen that in this case this quantity is mainly determined by the recirculating vortices, since the chemical reactions take place almost exclusively there. This region approaches similar conditions independently from the value of the Schmidt number, though with time-scales to it related, due to the absence of advective exchange between the vortices and the rest of the fluid domain, leading to the nearly equal selectivity values as shown in Fig. 5.21. This behavior has not been encountered at $\mathrm{Da}_1$=1 because the increase of the reaction intensities yields a different local field, as it emerges from the comparison between Figs. 5.22a and 5.22b. In this other case, the chemical reactions occur also more upstream and, therefore, the selectivity is not determined anymore exclusively by the recirculations. Under these circumstances, the changes in the fluid domain outside of the recirculations induced by the increase of the Schmidt number are responsible for the difference in the values of $S$ at $\mathrm{Re}_b$=219 visible in Fig. 5.20.

As a final remark, if the relative deviations between the minumum and maximum values of both the curves in Fig. 5.21 were computed neglecting the points at $\mathrm{Re}_b$=219, a minor dependence of the selectivity from $\mathrm{Re}_b$ would be again obtained in the higher Schmidt number case.

## 5.5 Comparison between simulations and film theory

Numerical simulations of bubble column reactors are usually carried out by means of Euler-Euler or Euler-Lagrange models. Some physico-chemical aspects are not directly resolved in these approaches but taken into account through closure relations. Reactive mass transfer simulations require a correlation for the enhancement factor which is usually provided by film or surface-renewal models. However, the strong simplifications assumed in these models can result in inaccurate correlations and, therefore, erroneous predictions of the reactor performances.

In this section, the accuracy of closure relations for the enhancement factor has been assessed by comparison to the numerical results of this work. Since the predictions of the different simplified models for both the reaction prototypes considered in the present study differ only slightly (see

Danckwerts, 1970, Onda et al., 1972 and Huang et al., 1980), only the closure relations based on the film theory have been considered here.

Regarding the single second-order irreversible reaction, Onda et al. (1972) derived, similar to Hikita (1964), the following expression

$$\mathrm{E} = \frac{\mathrm{Ha} \cdot \eta}{\tanh(\mathrm{Ha} \cdot \eta)} (1 - \frac{c_{B,\mathrm{b}}}{c_{B,\mathrm{i}}} \operatorname{sech}(\mathrm{Ha} \cdot \eta)), \tag{5.6}$$

where Ha is reported in Eq. (3.27), $c_{B,\mathrm{i}}$ and $c_{B,\mathrm{b}}$ denote the concentration of $B$ at the interface and at the film-bulk boundary, respectively, and $\eta$ is defined as

$$\eta = \sqrt{\frac{c_{A,\mathrm{i}}}{c_{A,\mathrm{b}}}}. \tag{5.7}$$

The concentrations $c_{A,\mathrm{i}}$ and $c_{A,\mathrm{b}}$ are the counterparts of $c_{B,\mathrm{i}}$ and $c_{B,\mathrm{b}}$ for the species $A$. Considering that the film in the numerical simulations is represented by the concentration boundary layer, the ratio $c_{B,\mathrm{b}}/c_{B,\mathrm{i}}$ in Eq. (5.6) takes very small values since the concentration at the border of the boundary layer is significantly lower than that at the interface. Thus, Eq. (5.6) can be reasonably simplified to

$$\mathrm{E} = \frac{\mathrm{Ha} \cdot \eta}{\tanh(\mathrm{Ha} \cdot \eta)}. \tag{5.8}$$

For each case of the simulation campaign, the quantity $\eta$ has been obtained by assuming $c_{A,\mathrm{b}}$ equal to $c_{A,\mathrm{in}}$ and computing $c_{A,\mathrm{i}}$ as the surface average of the liquid-sided interfacial concentration values of the species $A$ provided by the corresponding computation.

Table 5.6 contains the numerical and theoretical enhancement factors for the three largest Reynolds numbers at $\mathrm{Sc}_B$=10. It can be seen that the values predicted by Eq. (5.8) are in good agreement with the simulation results. The highest relative deviations are for intermediate chemical reactions intensities, i.e. $\mathrm{Da}_1$=1. However, they do not exceed 5%. The comparison for $\mathrm{Sc}_B$=100 limited to the case of $\mathrm{Re}_b$=219 is reported in Table 5.6. The maximum relative deviation is here even smaller with a value less than 3%.

The numerical enhancement factors have been plotted as function of the Hatta number in Figs. 5.23 and 5.24. For each Reynolds number or, equivalently, bubble diameter, the different Ha corresponding to the four $\mathrm{Da}_1$ chosen in this study are approximately 0.1, 0.31, 1 and 3.15 with small deviations from these average values due to the specific bubble size (cf. Fig. 5.23). A nearly total independence from the Reynolds number results from the overlapping of the profiles in Fig. 5.23. The distinct hydrodynamic conditions do not influence significantly the E−Ha curve. Fig. 5.10a has already pointed out this behavior. In fact, it emerged from this figure that the enhancement factors corresponding to the five Reynolds numbers at a fixed value of $\mathrm{Da}_1$ are comparable. The maximum deviation is approximately 6% for $\mathrm{Da}_1$=10. This result has been explained through the analysis of the local mass transfer coefficients. Taking as example the case of $\mathrm{Da}_1$=1, the comparison of Figs. 5.8 and 5.11a has highlighted that the local enhancement profiles along the polar angle are very similar for the various bubble sizes. Slight differences are present solely in the rear of the bubble with a minor contribution

to the global enhancement due to the limited areal extension of this region. Fig 5.23 suggests that the small influence of the Reynolds number on the enhancement factor at fixed $Da_1$ becomes negligible at fixed Ha. This is in agreement with the film theory relation (5.8) which does not contain the Reynolds number.

Table 5.6: Comparison of the enhancement factors obtained from the simulations of the single second-order reaction prototype with the predictions of the film theory solution by Onda et al. (1972), $Sc_B = 10$.

| $Re_b$ | $Da_1$ | $E_{sim}$ | $E_{Onda}$ | err / % |
|---|---|---|---|---|
| 173 | 0.01 | 1.004 | 1.0032 | 0.08 |
| | 0.1 | 1.0395 | 1.032 | 0.72 |
| | 1 | 1.3423 | 1.2999 | 3.16 |
| | 10 | 3.0093 | 3.0345 | 0.84 |
| 219 | 0.01 | 1.01 | 1.0035 | 0.64 |
| | 0.1 | 1.0563 | 1.0343 | 2.09 |
| | 1 | 1.386 | 1.3186 | 4.87 |
| | 10 | 3.0742 | 3.109 | 1.13 |
| 232 | 0.01 | 1.0054 | 1.0034 | 0.2 |
| | 0.1 | 1.0492 | 1.0334 | 1.51 |
| | 1 | 1.379 | 1.3111 | 4.93 |
| | 10 | 3.0163 | 3.0782 | 2.05 |

Table 5.7: Comparison of the enhancement factors obtained from the simulations of the single second-order reaction prototype with the predictions of the film theory solution by Onda et al. (1972), $Sc_B = 100$.

| $Re_b$ | $Da_1$ | $E_{sim}$ | $E_{Onda}$ | err / % |
|---|---|---|---|---|
| 219 | 0.01 | 1.007 | 1.0037 | 0.33 |
| | 0.1 | 1.0533 | 1.0363 | 1.61 |
| | 1 | 1.3785 | 1.3386 | 2.9 |
| | 10 | 3.1672 | 3.2443 | 2.43 |

For both the values of the Schmidt number, the $E - Ha$ curves resulting from the numerical simulations at $Re_b$=219 have been plotted in Fig. 5.24. The difference between the two curves in this figure is negligible. Accordingly, it can be deduced that the enhancement factor is also independent from the Schmidt number. Even this aspect is already captured by the film theory. In fact, $Sc_B$ does not appear in Eq. (5.8).

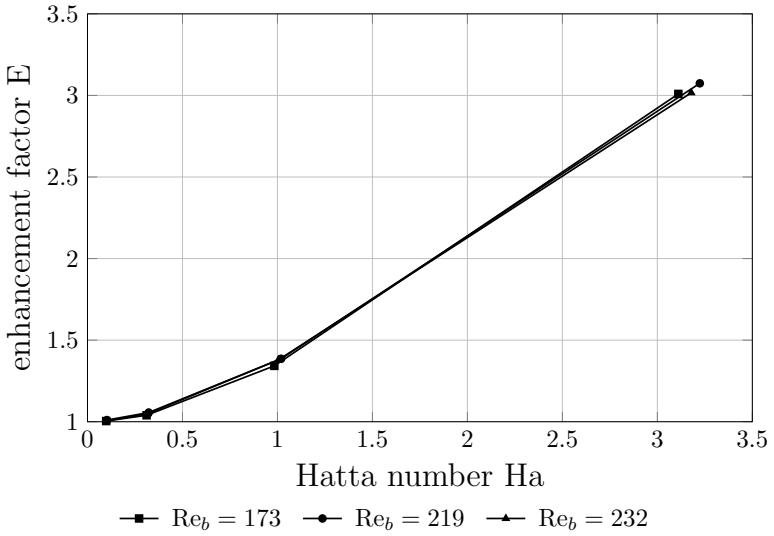


Figure 5.23: Enhancement factor as function of the Hatta number obtained from the simulations of the single second-order reaction prototype, $\mathrm{Re}_b = 173, 219, 232$ and $\mathrm{Sc}_B = 10$.

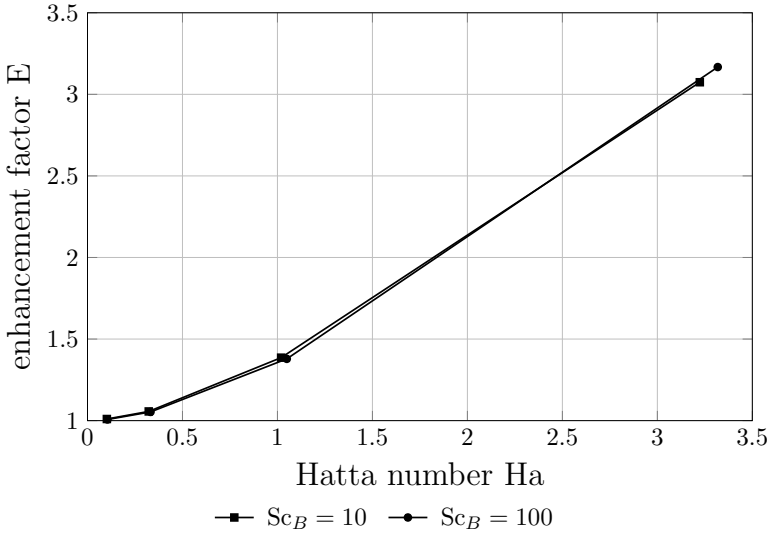


Figure 5.24: Enhancement factor as function of the Hatta number obtained from the simulations of the single second-order reaction prototype, $\mathrm{Re}_b = 219$ and $\mathrm{Sc}_B = 10, 100$.

Onda et al. also derived an expression for the enhancement factor of the competitive-consecutive mechanism considered in this work. They found that Eq. (5.6) for the single second-order irreversible reaction holds true even for this more complex reaction prototype. The only difference resides in the definition of $\eta$ which now reads

$$\eta = \sqrt{\frac{c_{A,\mathrm{i}}}{c_{A,\mathrm{b}}} + \kappa \frac{c_{P,\mathrm{i}}}{c_{A,\mathrm{b}}}}. \tag{5.9}$$

Now, the quantity $\eta$ also depends on the concentration $c_{P,\mathrm{i}}$ of the species $P$ at the interface and the ratio $\kappa$ between the two reaction coefficients. Analogously to $c_{A,\mathrm{i}}$, the quantity $c_{P,\mathrm{i}}$ for each case of the simulation campaign has been computed as the surface average of the liquid-sided interfacial concentration values of the species $P$ resulting from the corresponding computation.

The conditions, which previously allowed to assume that the ratio $c_{B,\mathrm{b}}/c_{B,\mathrm{i}}$ takes very small values, apply also in the case of the competitive-consecutive mechanism. This is here even more pronounced since the dissolving component is also consumed by the second reaction, leading to lower concentration values of the species $B$ in the liquid bulk in comparison to the single reaction prototype. For this reason, the enhancement factors have been again determined according to the simplified formula (5.8).

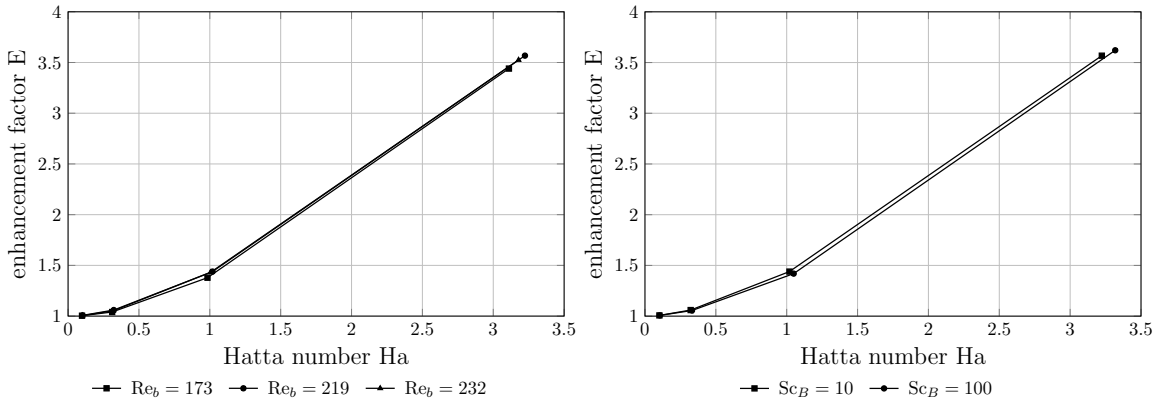


(a) (b)

Figure 5.25: Enhancement factor as function of the Hatta number obtained from the simulations of the competitive-consecutive reaction mechanism with $\kappa = 10$: (a) $\mathrm{Re}_b = 173, 219, 232$ and $\mathrm{Sc}_B = 10$; (b) $\mathrm{Re}_b = 219$ and $\mathrm{Sc}_B = 10, 100$.

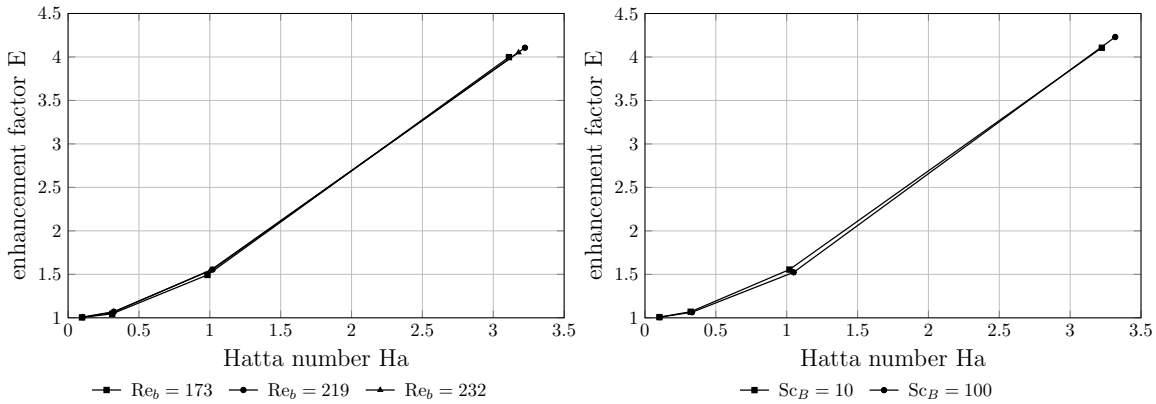


(a) (b)

Figure 5.26: Enhancement factor as function of the Hatta number obtained from the simulations of the competitive-consecutive reaction mechanism with $\kappa = 100$: (a) $\mathrm{Re}_b = 173, 219, 232$ and $\mathrm{Sc}_B = 10$; (b) $\mathrm{Re}_b = 219$ and $\mathrm{Sc}_B = 10, 100$.

Figs. 5.25a and 5.26a show the enhancement factor profiles as function of the Hatta number of the competitive-consecutive mechanism with $\kappa$ equal to 10 and 100, respectively, for the three largest Reynolds numbers at $Sc_B$=10. The different profiles overlap almost perfectly in both the figures, similar to what has been observed in Fig. 5.23 regarding the single reaction prototype. In fact, also here the differences between the enhancement factor values corresponding to the various Reynolds numbers along the iso-Damköhler lines (cf. Figs. 5.10b and 5.10c) become negligible at fixed Ha. Therefore, it turns out that the enhancement factor E depends basically on the Hatta number Ha and that a direct influence of the hydrodynamic conditions, i.e. $Re_b$, is not present, in agreement with the film theory.

Even a significant dependence from the Schmidt number is not visible, as it emerges from the comparison of the $E-Ha$ curves relating to the two different values of $Sc_B$ in Figs. 5.25b and 5.26b. Again the film theory proves to capture the qualitative evidence of the numerical simulations.

A quantitative measure of the accuracy of the film theory in predicting the enhancement factors for the competitive-consecutive mechanism is provided by Tables 5.8 and 5.9. Table 5.8 relating to $\kappa$=10 indicates that the higher relative deviations between the numerical and theoretical values are mostly encountered at $Da_1$=1, while these mainly occur at $Da_1$=10 in the case of $\kappa$=100 reported in Table 5.9. However, the maximum relative deviations of the two tables are both only slightly larger than 5%. As a final remark, it can be noted that the errors are generally lower at $Sc_B$=100 for both values of $\kappa$, similar to what has been observed for the single reaction prototype.

Table 5.8: Comparison of the enhancement factors obtained from the simulations of the competitive-consecutive mechanism with the predictions of the film theory solution by Onda et al. (1972), $\kappa = 10$.

| | | $Sc_B = 10$ | | | $Sc_B = 100$ | | |
|---|---|---|---|---|---|---|---|
| $Re_b$ | $Da_1$ | $E_{sim}$ | $E_{Onda}$ | err / % | $E_{sim}$ | $E_{Onda}$ | err / % |
| 173 | 0.01 | 1.004 | 1.0032 | 0.08 | 1.004 | 1.0035 | 0.05 |
| | 0.1 | 1.0403 | 1.0325 | 0.75 | 1.04 | 1.0355 | 0.44 |
| | 1 | 1.3784 | 1.3325 | 3.33 | 1.3713 | 1.3532 | 1.32 |
| | 10 | 3.4401 | 3.55 | 3.2 | 3.5046 | 3.6349 | 3.72 |
| 219 | 0.01 | 1.0072 | 1.0035 | 0.37 | 1.0071 | 1.0037 | 0.34 |
| | 0.1 | 1.0598 | 1.0354 | 2.3 | 1.0556 | 1.0372 | 1.74 |
| | 1 | 1.4392 | 1.3641 | 5.22 | 1.4191 | 1.3727 | 3.27 |
| | 10 | 3.5676 | 3.6968 | 3.62 | 3.6208 | 3.7313 | 3.05 |
| 232 | 0.01 | 1.0048 | 1.0034 | 0.15 | 1.0052 | 1.0034 | 0.17 |
| | 0.1 | 1.0519 | 1.0342 | 1.69 | 1.0493 | 1.0346 | 1.4 |
| | 1 | 1.4312 | 1.3534 | 5.43 | 1.406 | 1.3492 | 4.04 |
| | 10 | 3.5252 | 3.6545 | 3.67 | 3.5256 | 3.6075 | 2.33 |

Table 5.9: Comparison of the enhancement factors obtained from the simulations of the competitive-consecutive mechanism with the predictions of the film theory solution by Onda et al. (1972), $\kappa = 100$.

| | | $Sc_B = 10$ | | | $Sc_B = 100$ | | |
|---|---|---|---|---|---|---|---|
| $Re_b$ | $Da_1$ | $E_{sim}$ | $E_{Onda}$ | err / % | $E_{sim}$ | $E_{Onda}$ | err / % |
| 173 | 0.01 | 1.0041 | 1.0033 | 0.08 | 1.0041 | 1.0036 | 0.05 |
| | 0.1 | 1.0459 | 1.0362 | 0.93 | 1.0448 | 1.0384 | 0.61 |
| | 1 | 1.4927 | 1.455 | 2.53 | 1.4708 | 1.4557 | 1.03 |
| | 10 | 3.998 | 4.1851 | 4.68 | 4.1346 | 4.3012 | 4.03 |
| 219 | 0.01 | 1.0082 | 1.0036 | 0.45 | 1.0078 | 1.0038 | 0.4 |
| | 0.1 | 1.0702 | 1.0405 | 2.78 | 1.0643 | 1.0415 | 2.15 |
| | 1 | 1.5553 | 1.4912 | 4.12 | 1.5238 | 1.48 | 2.88 |
| | 10 | 4.1064 | 4.3142 | 5.06 | 4.2298 | 4.377 | 3.48 |
| 232 | 0.01 | 1.005 | 1.0034 | 0.16 | 1.0054 | 1.0035 | 0.19 |
| | 0.1 | 1.0626 | 1.0391 | 2.22 | 1.0584 | 1.0386 | 1.87 |
| | 1 | 1.5476 | 1.4769 | 4.57 | 1.5095 | 1.4511 | 3.87 |
| | 10 | 4.052 | 4.259 | 5.11 | 4.1054 | 4.2285 | 3 |

# Chapter 6

# Summary and Outlook

In the present work, reactive mass transfer processes from single rising bubbles have been investigated by means of Direct Numerical Simulations. In order to cope with the multiscale issue relating to these processes, a numerical strategy based on separate discretisations of the two-phase hydrodynamics and the mass transfer has been adopted. Following this strategy, two numerical techniques have been developed. These techniques differ regarding the solution of the species concentration transport equations, while for the two-phase hydrodynamics an Arbitrary Lagrangian Eulerian Interface-Tracking method is used in both the cases. In the first approach, Radial Basis Functions are employed to build up a finite-difference discretisation. This method is capable to deal with complex geometries and, therefore, ideal for large bubble surface deformations. Furthermore, the use of unstructered sets of points offers a greater flexibility in controlling the numerical resolution at the interface in comparison to mesh-based methods. However, it resulted to be computationally expensive and unstable in advection-dominated cases. Therefore, before it can be adopted to simulate reactive mass transfer processes in two-phase systems, further research is required in order to find a solution to its current problems. As an alternative, the species transport equations are solved on an auxiliary mesh obtained from the refinement of the grid used for the two-phase hydrodynamics in the region adjacent to the bubble surface. The so-called two-mesh approach proved to be capable to accurately resolve the very thin concentration boundary layers with reasonable computational costs.

A systematic analysis of the interaction between two-phase hydrodynamics, mass transfer and chemical reactions has been carried out by means of a large set of Direct Numerical Simulations using the two-mesh approach. A single reaction prototype and a competitive-consecutive mechanism, which are representative of many chemical engineering applications based on bubble column reactors, have been considered. Two-phase systems with different values of the Reynolds, Damköhler and Schmidt numbers have been simulated. This allowed to assess the influence of distinct hydrodynamic conditions, slow to fast chemical reactions and low to moderate dissolving species diffusivities on the transfer processes. The changes induced by the above mentioned nondimensional parameters on the mass transfer coefficient and the reaction selectivity have been investigated in detail. These two quantities determine the overall conversion rate of the reaction system and, therefore, are of fundamental

importance for all the applications based on such processes.

A number of results emerged from the numerical simulations. Firstly, for the investigated Reynolds number range corresponding to bubble diameters varying between approximately 1.5 mm and 4 mm, the computations have highlighted that higher mass transfer coefficients and reaction selectivities are found for smaller bubbles. However, in the case of $\mathrm{Sc}_B$=100, the influence of the bubble size on these two quantities diminishes due to the very thin concentration boundary layers, which result to be less affected by changes in the hydrodynamics. For the same reason, the conditions $\mathrm{Da}_1 \geq 1$ and $\kappa$=100 even cause nearly total independence from the bubble diameter. In fact, the concentration boundary layers become extremely thin for such high chemical reactions intensities.

The enhancement factor resulted to be only slightly dependent from the Reynolds number. By comparing the local mass transfer coefficients of both reactive and non-reactive cases, it turned out that the different bubble diameters are characterized by very similar local enhancement profiles. Noticeable differences appear only at large polar angles with a low impact on the overall mass transfer enhancement due to the reduced interfacial area of the rear region.

The simulations have confirmed the selectivity drop due to recirculations in the wake region at low Damköhler numbers reported by Khinast (2001) in his study based on a 2D fixed-shape bubble model. However, the rise of the selectivity with increasing $\mathrm{Re}_b$ at moderate to fast reaction intensities found in his results has not emerged from the computations performed in this work. On the contrary, a decreasing profile has been observed. This behavior has been explained through an analysis of the local selectivity fields.

For both the considered reaction prototypes, a good agreement between the values of the enhancement factor provided by the simulations and the film theory has been found. In both the cases, the largest discrepancies are about 5%. Furthermore, the simulations have shown nearly total independence of the enhancement factor from the Reynolds and Schmidt numbers, in accordance with the film theory.

As previously mentioned, the outcomes of this work are particularly relevant for bubble column reactors with homogeneous flows. To obtain an exhaustive description of all the different phenomena inside these reactors, the present research has to be complemented by an investigation of the influence of bubble shape instabilities on the reactive mass transfer. These instabilities occur at bubble diameters larger than those ones considered here. Further steps concern the addressing of the bubble-bubble interactions. This requires a considerable effort in the improvement of the ability of the ALE Interface-Tracking method to handle topological changes. This development is necessary in order to proceed towards a complete understanding of bubble column reactors with different flow regimes.

# Bibliography


Aboulhasanzadeh, B., S. Thomas, M. Taeibi-Rahni, and G. Tryggvason. "Multiscale computations of mass transfer from buoyant bubbles." Chemical Engineering Science 75 (2012): 456-467.

Aboulhasanzadeh, B., S. Hosoda, A. Tomiyama, and G. Tryggvason. "A validation of an embedded analytical description approach for the computations of high Schmidt number mass transfer from bubbles in liquids." Chemical Engineering Science 101 (2013): 165-174.

Agarwal, D. K., S. W. J. Welch, G. Biswas, and F. Durst. "Planar simulation of bubble growth in film boiling in near-critical water using a variant of the VOF method." Journal of Heat Transfer 126.3 (2004): 329-338.

Ahn, H. T., and M. Shashkov. "Multi-material interface reconstruction on generalized polyhedral meshes." Journal of Computational Physics 226.2 (2007): 2096-2132.

Akhtar, M., and S. Kleis. "A volume of fluid phase change model on adaptive octree grids." Journal of ASTM International 8 (2011).

Al-Rawahi, N., and G. Tryggvason. "Numerical simulation of dendritic solidification with convection: two-dimensional geometry." Journal of Computational Physics 180.2 (2002): 471-496.

Alke, A., and D. Bothe. "3D numerical modeling of soluble surfactant at fluidic interfaces based on the volume-of-fluid method." Fluid Dynamics and Materials Processing 5.4 (2009): 345-372.

Alke, A., D. Bothe, M. Kröger, and H. J. Warnecke. "VOF-based simulation of conjugate mass transfer from freely moving fluid particles." Computational Methods in Multiphase Flow V (2009): 157-168.

Alke, A., D. Bothe, M. Kröger, B. Weigand, D. Weirich, and H. Weking. "Direct numerical simulation of high Schmidt number mass transfer from air bubbles rising in liquids using the Volume-of-Fluid-Method." ERCOFTAC Bulletin, Dispersed Multiphase Flow: From Micro-to Macro-Scale Numerical Modeling, Bulletin 82 (2010): 50-59.

Awile, O., F. Büyükkeçeci, S. Reboux, and I. F. Sbalzarini. "Fast neighbor lists for adaptive-resolution particle simulations." Computer Physics Communications 183.5 (2012): 1073-1081.

Bader, G., and P. Deuflhard. “A semi-implicit mid-point rule for stiff systems of ordinary differential equations.” Numerische Mathematik 41.3 (1983): 373-398.

Bird, R. B., W. E. Stewart, and E. N. Lightfoot. “Transport phenomena.” John Wiley & Sons, 2007.

Booty, M. R., and M. Siegel. “A hybrid numerical method for interfacial fluid flow with soluble surfactant.” Journal of Computational Physics 229.10 (2010): 3864-3883.

Bork, O., M. Schlüter, S. Scheid and N. Räbiger. “Analysis of the effect of local hydrodynamics on mass transfer from bubbles using laser induced fluorescence.” 4th ASME-JSME Joint Fluids Engineering Conference (2003).

Bothe, D., M. Koebe, and H. J. Warnecke. “VOF-simulation of the rise behavior of single air bubbles with oxygen transfer to the ambient liquid.” Fortschritt Berichte-VDI Reihe 3 Verfahrenstechnik (2004): 134-146.

Bothe, D., M. Kröger, A. Alke, and H. J. Warnecke. “VOF-based simulation of reactive mass transfer across deformable interfaces.” Progress in Computational Fluid Dynamics, an International Journal 9.6-7 (2009): 325-331.

Bothe, D., M. Kröger, and H. J. Warnecke. “A VOF-based conservative method for the simulation of reactive mass transfer from rising bubbles.” Fluid Dynamics & Materials Processing 7.3 (2011): 303-316.

Bothe, D., and S. Fleckenstein. “A volume-of-fluid-based method for mass transfer processes at fluid particles.” Chemical Engineering Science 101 (2013): 283-302.

Brown, D., L. Ling, E. Kansa, and J. Levesley. “On approximate cardinal preconditioning methods for solving PDEs with radial basis functions.” Engineering Analysis with Boundary Elements 29.4 (2005): 343-353.

Bulirsch, R., and J. Stoer. “Numerical treatment of ordinary differential equations by extrapolation methods.” Numerische Mathematik 8.1 (1966): 1-13.

Can, E., and A. Prosperetti. “A level set method for vapor bubble dynamics.” Journal of Computational Physics 231.4 (2012): 1533-1552.

Chen, K., and M. Lai. “A conservative scheme for solving coupled surface-bulk convection-diffusion equations with an application to interfacial flows with soluble surfactant.” Journal of Computational Physics 257 (2014): 1-18.

Clift, R., J. R. Grace, and M. E. Weber. “Bubbles, drops, and particles.” (1978).

Crank, J. “The mathematics of diffusion.” Oxford university press (1979).

Danckwerts, P. V. “Significance of liquid-film coefficients in gas absorption.” Industrial & Engineering Chemistry 43.6 (1951): 1460-1467.

# Bibliography


Danckwerts, P. V. "Gas-Liquid Reactions." McGraw-Hill (1970).

Danckwerts, P. V., and A. J. Gillham. "Design of gas absorbers. I. Methods for predicting rates of absorption with chemical reaction in packed columns and tests with 11/2in. Raschig rings." Transactions of the Institution of Chemical Engineers 44.2 (1966).

Danckwerts, P. V., A. M. Kennedy, and D. Roberts. "Kinetics of $CO_2$ absorption in alkaline solutions-II: Absorption in a packed column and tests of surface-renewal models." Chemical Engineering Science 18.2 (1963): 63-72.

Dani, A., P. Guiraud, and A. Cockx. "Local measurement of oxygen transfer around a single bubble by planar laser-induced fluorescence." Chemical Engineering Science 62.24 (2007): 7245-7252.

Darmana, D. "On the multiscale modelling of hydrodynamics, mass transfer and chemical reactions in bubble columns." PhD thesis, Universiteit Twente (2006).

Darmana, D., N. G. Deen, and J. A. M. Kuipers. "Detailed 3D Modeling of Mass Transfer Processes in Two-Phase Flows with Dynamic Interfaces." Chemical Engineering & Technology 29.9 (2006): 1027-1033.

Davidson, M. R., and M. Rudman. "Volume-of-fluid calculation of heat or mass transfer across deforming interfaces in two-fluid flow." Numerical Heat Transfer: Part B: Fundamentals 41.3-4 (2002): 291-308.

Deising, D., H. Marschall, and D. Bothe. "A unified single-field model framework for Volume-Of-Fluid simulations of interfacial species transfer applied to bubbly flows." Chemical Engineering Science 139 (2016): 173-195

Demirdžić, I., and M. Perić. "Space conservation law in finite volume calculations of fluid flow." International Journal for Numerical Methods in Fluids 8.9 (1988): 1037-1050.

Deshpande, K. B., and W. B. Zimmerman. "Simulation of interfacial mass transfer by droplet dynamics using the level set method." Chemical Engineering Science 61.19 (2006): 6486-6498.

Dijkhuizen, W., I. Roghair, M. V. S. Annaland, and J. A. M. Kuipers. "DNS of gas bubbles behaviour using an improved 3D front tracking model-model development." Chemical Engineering Science 65.4 (2010): 1427-1437.

Drew, D. A., and S. L. Passman. "Theory of multicomponent fluids." Applied Mathematical Sciences 135 (1999).

Duineveld, P. C. "The rise velocity and shape of bubbles in pure water at high Reynolds number." Journal of Fluid Mechanics 292 (1995): 325-332.

Esmaeeli, A., and G. Tryggvason. "Computations of film boiling. Part I: numerical method." International Journal of Heat and Mass Transfer 47.25 (2004): 5451-5461.

Fasshauer, G. E. “Solving partial differential equations by collocation with radial basis functions.” in Mehaute, A.L., C. Rabut, and L. L. Schumaker (eds.), Surface Fitting and Multiresolution Methods (1997): 131-138.

Fasshauer, G. E. “Meshfree methods.” Handbook of Theoretical and Computational Nanotechnology 27 (2005): 33-97.

Fdhila, B., and P. C. Duineveld. “The effect of surfactant on the rise of a spherical bubble at high Reynolds and Péclet numbers.” Physics of Fluids 8.2 (1996): 310-321.

Ferziger, J. H., and M. Perić. “Computational methods for fluid dynamics.” (1996).

Figueroa-Espinoza, B., and D. Legendre. “Mass or heat transfer from spheroidal gas bubbles rising through a stationary liquid.” Chemical Engineering Science 65.23 (2010): 6296-6309.

Fleckenstein, S., and D. Bothe. “A Volume-of-Fluid-based numerical method for multi-component mass transfer with local volume changes.” Journal of Computational Physics 301 (2015): 35-58.

Fornberg, B., and G. Wright. “Stable computation of multiquadric interpolants for all values of the shape parameter.” Computers & Mathematics with Applications 48.5-6 (2004): 853-867.

Francois, M. M., and N. N. Carlson. “The balanced-force volume tracking algorithm and global embedded interface formulation for droplet dynamics with mass transfer.” ASME Conference (2010).

Francois, J., N. Dietrich, P. Guiraud, and A. Cockx. “Direct measurement of mass transfer around a single bubble by micro-PLIFI.” Chemical Engineering Science 66.14 (2011): 3328-3338.

Fujioka, H. “A continuum model of interfacial surfactant transport for particle methods.” Journal of Computational Physics 234 (2013): 280-294.

Ganesan, S., and L. Tobiska. “Arbitrary Lagrangian-Eulerian finite-element method for computation of two-phase flows with soluble surfactants.” Journal of Computational Physics 231.9 (2012): 3685-3702.

Gia, Q. T. Le, I. H. Sloan, and H. Wendland. “Multiscale RBF collocation for solving PDEs on spheres.” Numerische Mathematik 121.1 (2012): 99-125.

Ghosh, K., A. Mukhopadhyay, S. Sen, and D. Sanyal. “A sphericosymmetric VOF approach for investigating immiscible two-phase systems with one liquid phase.” Numerical Heat Transfer, Part A: Applications 50.10 (2006): 949-974.

Ghosh, K., A. Mukhopadhyay, S. Sen, and D. Sanyal. “An integral approach for simulation of vapour film dynamics around a spherical surface.” International Journal of Thermal Sciences 48.7 (2009): 1327-1337.

Gibou, F., L. Chen, D. Nguyen, and S. Banerjee. “A level set based sharp interface method for the multiphase incompressible NavierStokes equations with phase change.” Journal of Computational Physics 222.2 (2007): 536-555.

# Bibliography


Gorodetskaya, A. "The rate of rise of bubbles in water and aqueous solutions at great Reynolds numbers." Journal of Physical Chemistry 23 (1949): 71-77.

Gründing, D., S. Fleckenstein, and D. Bothe. "A subgrid-scale model for reactive concentration boundary layers for 3D mass transfer simulations with deformable fluid interfaces." International Journal of Heat and Mass Transfer 101 (2016): 476-487.

Guo, K., S. Hu, and X. Sun. "Conditionally positive definite functions and Laplace-Stieltjes integrals." Journal of Approximation Theory 74.3 (1993): 249-265.

Hardt, S., and F. Wondra. "Evaporation model for interfacial flows based on a continuum-field representation of the source terms." Journal of Computational Physics 227.11 (2008): 5871-5895.

Haroun, Y., D. Legendre, and L. Raynal. "Volume of fluid method for interfacial reactive mass transfer: application to stable liquid film." Chemical Engineering Science 65.10 (2010): 2896-2909.

Hayashi, K., and A. Tomiyama. "Interface tracking simulation of mass transfer from a dissolving bubble." The Journal of Computational Multiphase Flows 3.4 (2011): 247-261.

Hayashi, K., and A. Tomiyama. "Effects of Surfactant on Lift Coefficients of Bubbles in Linear Shear Flows." International Journal of Multiphase Flow (2017).

Higbie, R. "The rate of absorption of a pure gas into a still liquid during short periods of exposure." American Institute of Chemical Engineers Journal 31 (1935): 365-389.

Hikita, H. "Gas absorption with (m, n)-th order irreversible chemical reaction." International Chemical Engineering 4 (1964): 332-340.

Hirt, C. W., and B. D. Nichols. "Volume of fluid (VOF) method for the dynamics of free boundaries." Journal of Computational Physics 39.1 (1981): 201-225.

Houim, R. W., and K. K. Kuo. "A ghost fluid method for compressible reacting flows with phase change." Journal of Computational Physics 235 (2013): 865-900.

Huang, DT-J., J. J. Carberry, and A. Varma. "Gas absorption with consecutive secondorder reactions." American Institute of Chemical Engineers Journal 26.5 (1980): 832-839.

Ishii, M. "Thermo-fluid dynamic theory of two-phase flow." Eyrolles, France (1975).

Issa, R. I. "Solution of the implicitly discretised fluid flow equations by operator-splitting." Journal of Computational Physics 62.1 (1986): 40-65.

James, A. J., and J. Lowengrub. "A surfactant-conserving volume-of-fluid method for interfacial flows with insoluble surfactant." Journal of Computational Physics 201.2 (2004): 685-722.

Juncu, G. "Unsteady-state mass transfer from a binary gas bubble with changing volume." International Journal of Heat and Mass Transfer 54.1-3 (2011): 669-677.

Juncu, G. "Unsteady-state mass transfer accompanied by a first-order chemical reaction from a binary gas bubble with changing volume." International Journal of Heat and Mass Transfer 55.15-16 (2012): 4269-4275.

Juric, D., and G. Tryggvason. "Computations of boiling flows." International Journal of Multiphase Flow 24.3 (1998): 387-410.

Kansa, E. J. "Multiquadrics-A scattered data approximation scheme with applications to computational fluid-dynamics-II solutions to parabolic, hyperbolic and elliptic partial differential equations." Computers & Mathematics with Applications 19.8-9 (1990): 147-161.

Khatri, S., and A. Tornberg. "An embedded boundary method for soluble surfactants with interface tracking for two-phase flows." Journal of Computational Physics 256 (2014): 768-790.

Khinast, J. G. "Impact of 2D bubble dynamics on the selectivity of fast gas-liquid reactions." American Institute of Chemical Engineers Journal 47.10 (2001): 2304-2319.

Khinast, J. G., A. A. Koynov, and T. M. Leib. "Reactive mass transfer at gas-liquid interfaces: impact of micro-scale fluid dynamics on yield and selectivity of liquid-phase cyclohexane oxidation." Chemical Engineering Science 58.17 (2003): 3961-3971.

Koynov, A., and J. G. Khinast. "Effects of hydrodynamics and Lagrangian transport on chemically reacting bubble flows." Chemical Engineering Science 59.18 (2004): 3907-3927.

Koynov, A., J. G. Khinast, and G. Tryggvason. "Mass transfer and chemical reactions in bubble swarms with dynamic interfaces." American Institute of Chemical Engineers Journal 51.10 (2005): 2786-2800.

Kröger, M., A. Alke, D. Bothe, and H. J. Warnecke. "A VOF-based approach for the simulation of reactive mass transfer from rising bubbles." Fortschritt Berichte-VDI Reihe 3 Verfahrenstechnik 883 (2007): 290.

Kunkelmann, C., and P. Stephan. "CFD simulation of boiling flows using the volume-of-fluid method within OpenFOAM." Numerical Heat Transfer, Part A: Applications 56.8 (2009): 631-646.

Kück, U. D., M. Schlüter, and N. Räbiger. "Analyse des grenzschichtnahen Stofftransports an frei aufsteigenden Gasblasen." Chemie Ingenieur Technik 81.10 (2009): 1599-1606.

Ling, L., R. Opfer, and R. Schaback. "Results on meshless collocation techniques." Engineering Analysis with Boundary Elements 30.4 (2006): 247-253.

Lochiel, A. C., and P. H. Calderbank. "Mass transfer in the continuous phase around axisymmetric bodies of revolution." Chemical Engineering Science 19.7 (1964): 471-484.

Ma, C., and D. Bothe. "Numerical modeling of thermocapillary two-phase flows with evaporation using a two-scalar approach for heat transfer." Journal of Computational Physics 233 (2013): 552-573.

# Bibliography


Maric, T., H. Marschall, and D. Bothe. "voFoam-a geometrical volume of fluid algorithm on arbitrary unstructured meshes with local dynamic adaptive mesh refinement using OpenFOAM." arXiv preprint arXiv:1305.3417 (2013).

Marschall, H., K. Hinterberger, C. Schueler, F. Habla, and O. Hinrichsen. "Numerical simulation of species transfer across fluid interfaces in free-surface flows using OpenFOAM." Chemical Engineering Science 78 (2012): 111-127.

Majumder, S. K. "Hydrodynamics and Transport Processes of Inverse Bubbly Flow." Elsevier (2016).

Micchelli, C. A. "Interpolation of scattered data: distance matrices and conditionally positive definite functions." Constructive Approximation 2 (1986): 11-22.

Muradoglu, M., and G. Tryggvason. "A front-tracking method for computation of interfacial flows with soluble surfactants." Journal of Computational Physics 227.4 (2008): 2238-2262.

Muradoglu, M., and G. Tryggvason. "Simulations of soluble surfactants in 3D multiphase flow." Journal of Computational Physics 274 (2014): 737-757.

Muzaferija, S., and M. Perić. "Computation of free surface flows using interface-tracking and interface-capturing methods." in Mahrenholtz O., M. Markiewicz (eds.), Nonlinear Water Wave Interaction, Chap. 2 (1999): 59-100.

Olsson, E., and G. Kreiss. "A conservative level set method for two phase flow." Journal of Computational Physics 210.1 (2005): 225-246.

Onda, K., E. Sada, T. Kobayashi, and M. Fujine. "Gas absorption accompanied by complex chemical reactions-IV: unsteady state." Chemical Engineering Science 27.2 (1972): 247-255.

Onea, A., M. Wörner, and D. G. Cacuci. "A qualitative computational study of mass transfer in upward bubble train flow through square and rectangular mini-channels." Chemical Engineering Science 64.7 (2009): 1416-1435.

Osher, S., and J. A. Sethian. "Fronts propagating with curvature-dependent speed: algorithms based on Hamilton-Jacobi formulations." Journal of Computational Physics 79.1 (1988): 12-49.

Palaparthi, R., D. T. Papageorgiou, and C. Maldarelli. "Theory and experiments on the stagnant cap regime in the motion of spherical surfactant-laden bubbles." Journal of Fluid Mechanics 559 (2006): 1-44.

Pesci, C., A. Weiner, H. Marschall, and D. Bothe. "Computational analysis of single rising bubbles influenced by soluble surfactant." Journal of Fluid Mechanics 856 (2018): 709-763.

Peskin, C. S. "Numerical analysis of blood flow in the heart." Journal of Computational Physics 25.3 (1977): 220-252.

Prosperetti, A., and G. Tryggvason. "Computational methods for multiphase flow." Cambridge University Press (2007).

Quan, S., J. Lou, and D. P. Schmidt. "Modeling merging and breakup in the moving mesh interface tracking method for multiphase flow simulations." Journal of Computational Physics 228.7 (2009): 2660-2675.

Radl, S., A. Koynov, G. Tryggvason, and J. G. Khinast. "DNS-based prediction of the selectivity of fast multiphase reactions: Hydrogenation of nitroarenes." Chemical Engineering Science 63.12 (2008): 3279-3291.

Raffensberger, J. A., B. J. Glasser, and J. G. Khinast. "Analysis of heterogeneously catalyzed reactions close to bubbles." American Institute of Chemical Engineers Journal 51.5 (2005): 1482-1496.

Renardy, Y. Y., M. Renardy, and V. Cristini. "A new volume-of-fluid formulation for surfactants and simulations of drop deformation under shear at a low viscosity ratio." European Journal of Mechanics-B/Fluids 21.1 (2002): 49-59.

Rhie, C. M., and W. L. Chow. "Numerical study of the turbulent flow past an airfoil with trailing edge separation." American Institute of Aeronautics and Astronautics Journal 21.11 (1983): 1525-1532.

Rider, W. J., and D. B. Kothe. "Reconstructing volume tracking." Journal of Computational Physics 141.2 (1998): 112-152.

Roghair, I., M. Van Sint Annaland, and J. A. M. Kuipers. "An improved Front-Tracking technique for the simulation of mass transfer in dense bubbly flows." Chemical Engineering Science 152 (2016): 351-369.

Rudman, M. "Volume-tracking methods for interfacial flow calculations." International Journal for Numerical Methods in Fluids 24.7 (1997): 671-691.

Rusche, H. "Computational fluid dynamics of dispersed two-phase flows at high phase fractions." PhD thesis, Imperial College London (2003).

Saboni, A., S. Alexandrova, M. Karsheva, and C. Gourdon. "Mass transfer from a contaminated fluid sphere." American Institute of Chemical Engineers Journal 57.7 (2011): 1684-1692.

Šarler, B., and R. Vertnik. "Meshfree explicit local radial basis function collocation method for diffusion problems." Computers & Mathematics with Applications 51.8 (2006): 1269-1282.

Satapathy, R., and W. Smith. "The motion of single immiscible drops through a liquid." Journal of Fluid Mechanics 10.4 (1961): 561-570.

Sato, Y., and B. Ničeno. "A sharp-interface phase change model for a mass-conservative interface tracking method." Journal of Computational Physics 249 (2013): 127-161.

## Bibliography


Schlottke, J., and B. Weigand. "Direct numerical simulation of evaporating droplets." Journal of Computational Physics 227.10 (2008): 5215-5237.

Schlüter, M., O. Bork, S. Scheid, S. Hövelmann, N. Räbiger. "New aspects of hydrodynamics and mass transfer in multiphase flows". International Conference on Multiphase Flows, Tulane University, New Orleans (2001).

Schoenberg, I. J. "Metric spaces and completely monotone functions." Annals of Mathematics (1938): 811-841.

Shah, Y. T., B. G. Kelkar, S. P. Godbole, and W. D. Deckwer. "Design parameters estimations for bubble column reactors." American Institute of Chemical Engineers Journal 28.3 (1982): 353-379.

Shin, S. W., and D. Juric. "Computation of microstructure in solidification with fluid convection." Journal of the Mechanical Behavior of Materials 11.4 (2000): 313-320.

Shin, S., and D. Juric. "Modeling three-dimensional multiphase flow using a level contour reconstruction method for front tracking without connectivity." Journal of Computational Physics 180.2 (2002): 427-470.

Shin, S., and D. Juric. "A hybrid interface method for three-dimensional multiphase flows based on front tracking and level set techniques." International Journal for Numerical Methods in Fluids 60.7 (2009): 753-778.

Stevens, D., H. Power, M. Lees, and H. Morvan. "The use of PDE centres in the local RBF Hermitian method for 3D convective-diffusion problems." Journal of Computational Physics 228.12 (2009): 4606-4624.

Stöhr, M., J. Schanze, and A. Khalili. "Visualization of gas-liquid mass transfer and wake structure of rising bubbles using pH-sensitive PLIF." Experiments in Fluids 47.1 (2009): 135-143.

Strotos, G., M. Gavaises, A. Theodorakakos, and G. Bergeles. "Numerical investigation of the evaporation of two-component droplets." Fuel 90.4 (2011): 1492-1507.

Stuke, B. "Das Verhalten der Oberfläche von sich in Flüssigkeiten bewegenden Gasblasen." Naturwissenschaften 39.14 (1952): 325-326.

Sun, X. "Scattered Hermite interpolation using radial basis functions." Linear Algebra and its Applications 207 (1994): 135-146.

Sun, X. "Conditional positive definiteness and complete monotonicity." Series in Approximations and Decompositions 6 (1995): 537-540.

Sussman, M., P. Smereka, and S. Osher. "A level set approach for computing solutions to incompressible two-phase flow." Journal of Computational Physics 114.1 (1994): 146-159.

Takemura, F., and Y. Matsumoto. "Dissolution rate of spherical carbon dioxide bubbles in strong alkaline solutions." Chemical Engineering Science 55.18 (2000): 3907-3917.

Takemura, F., and A. Yabe. "Gas dissolution process of spherical rising gas bubbles." Chemical Engineering Science 53.15 (1998): 2691-2699.

Takemura, F., and A. Yabe. "Rising speed and dissolution rate of a carbon dioxide bubble in slightly contaminated water." Journal of Fluid Mechanics 378 (1999): 319-334.

Tanguy, S., T. Ménard, and A. Berlemont. "A level set method for vaporizing two-phase flows." Journal of Computational Physics 221.2 (2007): 837-853.

Tomar, G., G. Biswas, A. Sharma, and A. Agrawal. "Numerical simulation of bubble growth in film boiling using a coupled level-set and volume-of-fluid method." Physics of Fluids 17.11 (2005): 112103.

Torres, D. J., and J. U. Brackbill. "The point-set method: front-tracking without connectivity." Journal of Computational Physics 165.2 (2000): 620-644.

Tryggvason, G., B. Bunner, A. Esmaeeli, D. Juric, N. Al-Rahawi, W. Tauber, J. Han, S. Nas, and Y.-J. Jan. "A front-tracking method for the computations of multiphase flow." Journal of Computational Physics 169.2 (2001): 708-759.

Tryggvason, G., R. Scardovelli, and S. Zaleski. "Direct numerical simulations of gas-liquid multiphase flows." Cambridge University Press (2011).

Tuković, Ž., and H. Jasak. "A moving mesh finite volume interface tracking method for surface tension dominated interfacial fluid flow." Computers & Fluids 55 (2012): 70-84.

Ubbink, O., and R. I. Issa. "A method for capturing sharp fluid interfaces on arbitrary meshes." Journal of Computational Physics 153.1 (1999): 26-50.

Unverdi, S. O., and G. Tryggvason. "A front-tracking method for viscous, incompressible, multi-fluid flows." Journal of Computational Physics 100.1 (1992): 25-37.

Urseanu, M. I., and R. Krishna. "Scaling up bubble column reactors." PhD thesis, Universiteit van Amsterdam (2000).

Wang, Q., M. Siegel, and M. R. Booty. "Numerical simulation of drop and bubble dynamics with soluble surfactant." Physics of Fluids 26.5 (2014): 052102.

Weber, P., H. Marschall, and D. Bothe. "Highly accurate two-phase species transfer based on ALE Interface Tracking." International Journal of Heat and Mass Transfer 104 (2017): 759-773.

Weiner, A., and D. Bothe. "Advanced subgrid-scale modeling for convection-dominated species transport at fluid interfaces with application to mass transfer from rising bubbles." Journal of Computational Physics 347 (2017): 261-289.

## Bibliography


Welch, S. W., and T. Rachidi. "Numerical computation of film boiling including conjugate heat transfer." Numerical Heat Transfer: Part B: Fundamentals 42.1 (2002): 35-53.

Welch, S. W., and J. Wilson. "A volume of fluid based method for fluid flows with phase change." Journal of Computational Physics 160.2 (2000): 662-682.

Wendland, H. "Piecewise polynomial, positive definite and compactly supported radial functions of minimal degree." Advances in Computational Mathematics 4.1 (1995): 389-396.

Whitman, W. G. "The two-film theory of gas absorption." Chemical and Metallurgical Engineering 29 (1923): 146-148.

Winnikow, S. "Letter to the Editors." Chemical Engineering Science 22.3 (1967): 477.

Wörner, M. "Numerical modeling of multiphase flows in microfluidics and micro process engineering: a review of methods and applications." Microfluidics and Nanofluidics 12.6 (2012): 841-886.

Wright, G. B., and B. Fornberg. "Scattered node compact finite difference-type formulas generated from radial basis functions." Journal of Computational Physics 212.1 (2006): 99-123.

Wu Z. "Solving PDEs with radial basis functions and the error estimation." in Chen Z. et al. (eds.), Advances in Computational Mathematics (1998).

Yuan, M. H., Y. H. Yang, T. S. Li, and Z. H. Hu. "Numerical simulation of film boiling on a sphere with a volume of fluid interface tracking method." International Journal of Heat and Mass Transfer 51.7-8 (2008): 1646-1657.

Zhang, Y., J. B. McLaughlin, and J. A. Finch. "Bubble velocity profile and model of surfactant mass transfer to bubble surface." Chemical Engineering Science 56.23 (2001): 6605-6616.